

M.Sc. in Mechanical Engineering Thesis

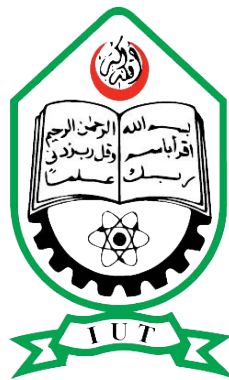
A Numerical Investigation of Local Scour Around Different Shape of Bridge Piers and Its Reduction

Submitted by

Rumana Hasan
181011006

Supervised by

Prof. Dr. Md. Hamidur Rahman



**Department of Mechanical and Production Engineering
Islamic University of Technology**

Dhaka, Bangladesh

June, 2022

CANDIDATES' DECLARATION

This is to certify that the work presented in this thesis, titled, “A Numerical Investigation of Local Scour Around Different Shape of Bridge Piers and Its Reduction”, is the outcome of the investigation and research carried out by me under the supervision of Prof. Dr. Md. Hamidur Rahman.

It is also declared that neither this thesis nor any part thereof has been submitted anywhere else for the award of any degree, diploma or other qualifications.

Rumana Hasan
181011006

This thesis titled, “**A Numerical Investigation of Local Scour Around Different Shape of Bridge Piers and Its Reduction**”, submitted by Rumana Hasan, Student ID: 181011006, has been accepted as satisfactory in partial fulfillment of the requirements for the degree M.Sc. in Mechanical Engineering on 20th June, 2022.

BOARD OF EXAMINERS

Dr. Md. Hamidur Rahman Professor Mechanical and Production Engineering, IUT, Bangladesh	Chairman (Supervisor)
---	--------------------------

Dr. Md. Anayet Ullah Patwari Head and Professor Mechanical and Production Engineering, IUT, Bangladesh	Member (Ex-Officio)
--	------------------------

Dr. Md. Rezwanul Karim Associate Professor Mechanical and Production Engineering, IUT, Bangladesh	Member
---	--------

Dr. Mohammad Zoynal Abedin Professor Mechanical Engineering, DUET, Bangladesh	Member (External)
---	----------------------

ACKNOWLEDGEMENT

To begin with, I would like to express my gratitude to the Almighty Allah for his benevolence and favor towards me, especially during my academic career, and for enabling me to achieve this moment in life.

It would not have been possible to complete the research work without the continuous support of my thesis supervisor Prof. Dr. Md. Hamidur Rahman. Throughout the journey, I found him as an inspiring mentor who managed a place for me in the well-equipped simulation lab of the MPE department and with other technical details of Local Scour. I want to thank Dr. Arafat Ahmed Bhuiyan and Dr. Md. Rezwanul Karim, Associate Professor of MPE department, for their worthwhile guidance towards the successful completion of the degree. I also like to acknowledge the favor of MPE faculty members, especially Mr. Chowdhury Sadid Alam and Mr. Tahsin Sejat Saniat, for the time-to-time support regarding the M.Sc. coursework and other administrative processes.

Apart from this, I appreciate my family for their generous support throughout my hard time on this project.

Dhaka
June, 2022

Rumana Hasan

Contents

<i>CANDIDATES' DECLARATION</i>	i
<i>CERTIFICATION</i>	ii
<i>ACKNOWLEDGEMENT</i>	iii
List of Figures	vi
List of Tables	x
<i>ABSTRACT</i>	xi
1 Introduction	1
1.1 Bridge Scour	1
1.2 Areas Affected By Local Scour	1
1.3 Basic Theory Related To Scouring	2
1.4 Different Types Of Bridge Scour	3
1.5 Scouring Mechanism	5
1.6 Factors Affecting Bridge Scour	6
1.7 Research Objectives	8
1.8 Methodology	8
1.9 Research Outcomes	9
2 Literature Review	10
3 Design and Simulation	15
3.1 Governing Equations	15
3.1.1 Bed Shear Stress	15
3.1.2 Critical Shields Parameter	16
3.1.3 Entrainment and Deposition	17
3.1.4 Bed Load Transport	18
3.1.5 Suspended Load Transport	20
3.2 Turbulence Modeling With FLOW-3D	20
3.3 Geometry Of Bridge Pier Structure	22

3.3.1	Sketch And Dimensions	23
3.4	Numerical Modeling Of The River Bed	25
3.4.1	Dimension Of The River Bed	25
3.4.2	Sediment Scour Model	26
3.4.3	Boundary Conditions	26
3.4.4	Mesh Generations And Mesh Planes	27
3.5	Grid Independence Test	31
3.6	Validation	32
4	Results and Discussions	34
4.1	Scour Depth And Sand Deposition Analysis	34
4.1.1	Cylindrical Shaped Pier	34
4.1.2	Square Shaped Pier	36
4.1.3	Diamond Shaped Pier	38
4.1.4	Hexagonal-Sharp Nose Shaped Pier	40
4.1.5	Hexagonal-Vertical Nose Shaped Pier	42
4.1.6	Airfoil Shaped Pier	44
4.1.7	Upstream Facing Airfoil Shaped Pier	46
4.1.8	Downstream Facing Airfoil Shaped Pier	48
4.1.9	Oblong Shaped Pier	50
4.1.10	Rectangle Shaped Pier	52
4.1.11	Comparison Of The Scour Depths And Sediment Deposition	53
4.1.12	Scour Depth In 3D View	57
4.2	Velocity and Pressure Distribution	59
4.3	Time Dependent Analysis Of Scour Depth And Sediment Deposition	64
4.3.1	Scour Depth Over Time	64
4.3.2	Sediment Deposition Over Time	65
4.4	Reduction Of Local Scour	66
4.4.1	Tapered Cylindrical Bridge Piers	66
4.4.2	Tapered Hexagonal Bridge Piers	67
4.4.3	Anti-Scour Collar Plates	70
4.5	Effective Pier Geometry For Bridge Construction	73
5	Conclusions and Recommendations	74
5.1	Conclusions	74
5.2	Recommendations	75
	References	77

List of Figures

1.1	Shields graph [1]	3
1.2	Classification of scour	4
1.3	Scour depth versus time graph [3]	5
1.4	A schematic representation of the local scour around cylindrical bridge pier [4]	6
1.5	The horseshoe vortex and the wake vortex [5]	6
1.6	Influence of flow depth and width of the pier [7]	7
1.7	Steps in numerical analysis	8
2.1	Bridge collapse due to scouring effect [9]	10
2.2	The allocation of bridge failure yields between 1989 and 2000 in the US [11]	11
2.3	Schoharie Creek Bridge Collapse [16]	12
3.1	2D sketch of pier shapes in SOLIDWORKS	23
3.2	River bed with outlines	25
3.3	Boundary conditions	26
3.4	Location of mesh planes for Cylindrical pier	27
3.5	Meshing in XY plane for Cylindrical pier	28
3.6	Meshing in YZ plane for Cylindrical pier	28
3.7	Meshing in ZX plane for Cylindrical pier	28
3.8	Total mesh cells in 3D domain for Cylindrical pier	29
3.9	Location of mesh planes for airfoil pier	29
3.10	Meshing in XY plane for Airfoil pier	30
3.11	Meshing in YZ plane for Airfoil pier	30
3.12	Meshing in ZX plane for Airfoil pier	30
3.13	Total mesh cells in 3D domain for Airfoil pier	31
3.14	Grid independent test for cylindrical pier	31
3.15	Mesh cells size at the surroundings of the pier in the YZ plane	32
3.16	Numerical and experimental comparison among the scour depth contour plot of Cylindrical shaped pier	33
3.17	Numerical and experimental comparison among the scour depth contour plot of Diamond shaped pier	33
4.1	Packed sediment elevation net change for Cylindrical pier in YZ plane	34

4.2	3D Scour depth for the cylindrical pier with a fraction of fluid	35
4.3	Packed sediment elevation net change for Cylindrical pier in ZX plane	35
4.4	Scour depth contour plot of the river bed for Cylindrical pier after scouring . . .	35
4.5	Packed sediment elevation net change for Square pier in YZ plane	36
4.6	3D Scour depth for the square pier with a fraction of fluid	36
4.7	Packed sediment elevation net change for Square pier in ZX plane	37
4.8	Scour depth contour plot of the river bed for Square pier after scouring	37
4.9	Packed sediment elevation net change for Diamond pier in YZ plane	38
4.10	3D Scour depth for the diamond pier with a fraction of fluid	38
4.11	Packed sediment elevation net change for Diamond pier in ZX plane	39
4.12	Scour depth contour plot of the river bed for Diamond pier after scouring	39
4.13	Packed sediment elevation net change for Hexagonal- Sharp Nose pier in YZ plane	40
4.14	3D Scour depth for the hexagonal-sharp nose pier with a fraction of fluid	40
4.15	Packed sediment elevation net change for Hexagonal- Sharp Nose pier in ZX plane	41
4.16	Scour depth contour plot of the river bed for Hexagonal- Sharp Nose pier after scouring	41
4.17	Packed sediment elevation net change for Hexagonal- Vertical Nose pier in YZ plane	42
4.18	3D Scour depth for the hexagonal-vertical nose pier with a fraction of fluid	42
4.19	Packed sediment elevation net change for Hexagonal- Vertical Nose pier in ZX plane	43
4.20	Scour depth contour plot of the river bed for Hexagonal- Vertical Nose pier after scouring	43
4.21	Packed sediment elevation net change for Airfoil pier in YZ plane	44
4.22	3D Scour depth for the airfoil pier with a fraction of fluid	44
4.23	Packed sediment elevation net change for Airfoil pier in ZX plane	45
4.24	Scour depth contour plot of the river bed for Airfoil pier after scouring	45
4.25	Packed sediment elevation net change for Upstream Facing Airfoil pier in YZ plane	46
4.26	3D Scour depth for the upstream facing airfoil pier with a fraction of fluid	46
4.27	Packed sediment elevation net change for Upstream Facing Airfoil pier in ZX plane	47
4.28	Scour depth contour plot of the river bed for Upstream Facing Airfoil pier after scouring	47
4.29	Packed sediment elevation net change for Downstream Facing Airfoil pier in YZ plane	48
4.30	3D Scour depth for the downstream facing airfoil pier with a fraction of fluid	48

4.31	Packed sediment elevation net change for Downstream Facing Airfoil pier in ZX plane	49
4.32	Scour depth contour plot of the river bed for Downstream Facing Airfoil pier after scouring	49
4.33	Packed sediment elevation net change for Oblong pier in YZ plane	50
4.34	3D Scour depth for the oblong pier with a fraction of fluid	50
4.35	Packed sediment elevation net change for Oblong pier in ZX plane	51
4.36	Scour depth contour plot of the river bed for Oblong pier after scouring	51
4.37	Packed sediment elevation net change for Rectangle pier in YZ plane	52
4.38	3D Scour depth for the rectangle pier with a fraction of fluid	52
4.39	Packed sediment elevation net change for Rectangle pier in ZX plane	53
4.40	Scour depth contour plot of the river bed for Rectangle pier after scouring	53
4.41	Comparison among the scour depth and sediment deposition of cylindrical, square, diamond, and hexagonal piers	54
4.42	Comparison among the scour depth and sediment deposition of airfoil, oblong, and rectangle piers	55
4.43	River bed in 3D after scouring for cylindrical, square, diamond, hexagonal pier	57
4.44	River bed in 3D after scouring for airfoil, oblong, rectangle pier	58
4.45	Velocity and pressure distribution for cylindrical pier in ZX plane	59
4.46	Velocity and pressure distribution for square pier in ZX plane	60
4.47	Velocity and pressure distribution for diamond pier in ZX plane	60
4.48	Velocity and pressure distribution for hexagonal-sharp nose pier in ZX plane	61
4.49	Velocity and pressure distribution for hexagonal-vertical nose pier in ZX plane	61
4.50	Velocity and pressure distribution for airfoil pier in ZX plane	62
4.51	Velocity and pressure distribution for upstream facing airfoil pier in ZX plane	62
4.52	Velocity and pressure distribution for downstream facing airfoil pier in ZX plane	63
4.53	Velocity and pressure distribution for oblong pier in ZX plane	63
4.54	Velocity and pressure distribution for rectangle pier in ZX plane	64
4.55	Scour depth vs Time	65
4.56	Sediment deposition vs Time	65
4.57	3D sketch of non-tapered vs tapered cylindrical pier	66
4.58	Packed sediment elevation net change for non-tapered vs tapered cylindrical pier	67
4.59	Velocity distribution and pressure contour of the tapered cylindrical pier	67
4.60	3D sketch of non-tapered vs tapered hexagonal-sharp nose pier	68
4.61	Packed sediment elevation net change for non-tapered vs tapered hexagonal-sharp nose pier	68
4.62	Velocity distribution and pressure contour of the tapered hexagonal-sharp nose pier	69
4.63	The Padma Multipurpose Bridge, Bangladesh	69

4.64	Collar plate	70
4.65	Effect of collar plates on scour depths	71
4.66	2D contour plot of scour depth in the presence of collar plates	71
4.67	2D contour plot of scour depth in the presence of collar plates	72
4.68	Comparing the scour depth for cylindrical, tapered cylindrical, and cylindrical piers with collar plates	73
5.1	3D model of splitter and plate	75
5.2	Multiple splitters attached to the cylindrical pier	76
5.3	Front and back plate attached to the cylindrical pier	76

List of Tables

3.1	Bed load coefficient for different transport type	19
3.2	Top view of the bridge piers	22
3.3	Dimensions of the piers along X,Y, Z axis for non-tapered shape	24
3.4	Dimensions of the piers along X,Y, Z axis for tapered shape	24
3.5	Dimensions of the river bed along X,Y, Z axis	25
3.6	Placement of pier in the river bed	25
3.7	Sediment scour model in SI unit	26
3.8	Boundary Conditions	27
3.9	Volume flow rate and fluid elevation	27
3.10	Total mesh cells in the domain	29
3.11	Number of cells in X, Y, Z directions	32
3.12	Numerical and experimental comparison of scour depth	33
4.1	Scour depth and sediment deposition	54
4.2	Scour depth and sediment deposition	55
4.3	Scour depths around the pier in cm unit	56
4.4	Percentage change in scour depth for tapered cylindrical pier	67
4.5	Percentage change in scour depth for tapered hexagonal-sharp nose pier	69
4.6	Scour depth with multiple collar plates attaching to the cylindrical pier in cm	70
4.7	Scour depth for non-tapered cylindrical, tapered cylindrical, and cylindrical pier with collar plates	73

ABSTRACT

Around the world, local scour is one of the leading causes of bridge collapses and other hydraulic structure failures. The study demonstrates the scour depth and fluid dynamics of different shaped bridge piers, including cylindrical, square, diamond, hexagonal-sharp nose, hexagonal-vertical nose, airfoil, upstream facing airfoil, downstream facing airfoil, oblong, and rectangle piers through simulations. This study aims to discover the most efficient pier with the lowest scour depth. Tapered shape bridge piers and collar plates around the cylindrical pier are also discussed here to reduce the effect of local scouring. The FLOW-3D software has been used to solve the most challenging free surface flow problems using the Renormalized Group (RNG) $k-\epsilon$ turbulence model. Positioning a collar plate below the bed level will decrease scour depth, and using a combination of one collar plate under the bed level and one collar plate above the bed level will reduce the scour depth even more. According to the study, the tapered cylindrical pier has the lowest scour depth among the other bridge piers. The scour depth of the tapered cylindrical pier is 19.23% lower than the tapered hexagonal sharp nose pier. In comparison to a non-tapered cylindrical pier and a cylindrical pier with one collar plate under the bed level and one above the bed level, the scour depth of a tapered cylindrical pier is 33.96% and 9.48% less, respectively. As the piers are streamlined and sharply edged, the scour depth is higher for airfoil and diamond piers. The scour depth of diamond pier is 98% greater than the tapered cylindrical pier. The analysis also indicates that there is more scouring in the vicinity of the piers upstream than downstream.

Chapter 1

Introduction

1.1 Bridge Scour

Bridge Scour is the process of removing sediments, sand particles, and gravel from the surrounding area of the bridge piers structure and leaving a scour hole. Around the world, it is one of the vital factors in bridge failure. Whenever the flow conditions are turbulent, the scouring problem is complicated to assess because various factors need to be considered, such as flow depth, velocity, pier geometry, and types of river bed sand. This is why erosion caused by flowing water around the bridge piers is one of the most fundamental hazardous situations in river engineering. Piers are often susceptible to local scour due to the rapid water flow and turbulence. A local scour develops due to the increased velocity and associated vortices around the piers. These scours increase gradually in-depth as the water speeds up to around the piers. Bridge foundations can fail partially or even collapse completely if local scouring occurs around the foundations. During a steady current flow, a vertical pier placed in a riverbed will identify the variations in the flow pattern along with sediment transportation around the pier. As a result, bridge piers are designed to reduce collapse due to local scour. The mechanical design of bridge piers must be based on accurate estimation.

1.2 Areas Affected By Local Scour

Local scour is more likely to develop around piers and abutments because the water flows faster. Contractions scour occurs at bridge openings when water flows through a narrow space compared to the upstream channel. Degradation scour takes place both downstream and upstream over a large area. The stream bed can be lowered over time as a result.

1.3 Basic Theory Related To Scouring

The sediment doesn't move simply because of the action or flow of water. However, it requires a minimum or threshold force regardless of whether it is deposition or transportation. Sediment motion is initiated by bed shear stress in Equation (1.1).

The sediment does not move at lower bed shear stress, but when the numerical value gradually increases after a certain point, the individual particles start to move. The circumstances of the fluid flow that result in motion in the sediment are known as critical motions. Shear stress caused by movement in the bed is critical shear stress τ_c . When there is no movement then $\tau_o < \tau_c$ And movement occurs only when the bed shear stress reaches the critical point that is $\tau_o = \tau_c$.

$$\tau_o = \gamma R S_o \quad (1.1)$$

$$R_{*c} = \frac{U_{*c} d}{\nu} \quad (1.2)$$

$$\tau_{*c} = \frac{\tau_c}{(\gamma_s - \gamma)d} \quad (1.3)$$

$$\gamma_s = \rho_s g \quad (1.4)$$

$$\gamma = \rho g \quad (1.5)$$

$$U_{*c} = \sqrt{\frac{\tau_c}{\rho}} \quad (1.6)$$

Where,

d = Grain diameter

γ_s = Unit weight of the sediment particle

τ_c = Critical shear stress

ν = kinematic viscosity

R_{*c} = Critical Reynolds number

U_{*c} = Characteristic particle velocity

τ_{*c} = Non dimensional shear stress

S_o = The slope

Shields finds a functional relationship between the two parameters R_{*c} and τ_{*c} based on several experimental analyses [1] [2]. Shields Diagram in Figure 1.1 is the curve that represents the relationship between these two.

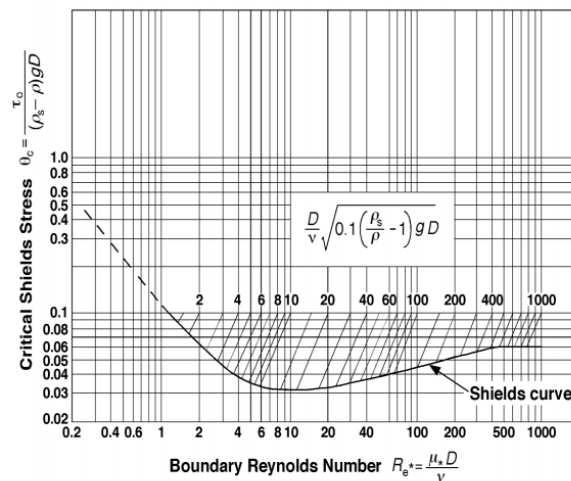


Figure 1.1: Shields graph [1]

The Shields curve clearly shows that up to $R_{*c} = 2$ the flow is pretty smooth in nature, and the particle diameter has no effect on the critical shields stress. There is a transition stage for $2 < R_{*c} < 400$, and both the velocity and particle diameter have an impact on critical shields stress, but after that range, it becomes nearly constant. Since sediment size is not uniform in nature, it is convenient to take the median size d_{50} .

1.4 Different Types Of Bridge Scour

In an open channel flow with a mobile sand bed, sediment is usually transported, resulting in erosion and deposition. If the channel geometry or the flow of the water changes, there will be additional erosion of sediments.

Different types of local scour are associated with fluvial hydraulics. When a structural pier or abutment is placed in the flow, the obstruction will alter the flow locally, causing erosion and deposition to occur nearby. A narrowed channel may encounter contraction scour. There is a considerable chance of scouring occurring downstream when water flows over or under a hydraulic structure. Figure 1.2 illustrates the classification of local scour.

Degradation scour: Streambed elevation can change over time as a result of natural calamities. There is a possibility that these changes can have an impact on the river near the bridge. For aggradation and degradation, a reference surface must be established at a discrete time in the river's history. If historical streamflow data are not available, it is difficult to measure changes occurring over a long period at the site of the bridge structure. Paleogeomorphologists can often estimate past and future geomorphic changes for rivers using sediment stratigraphy and vegetation.

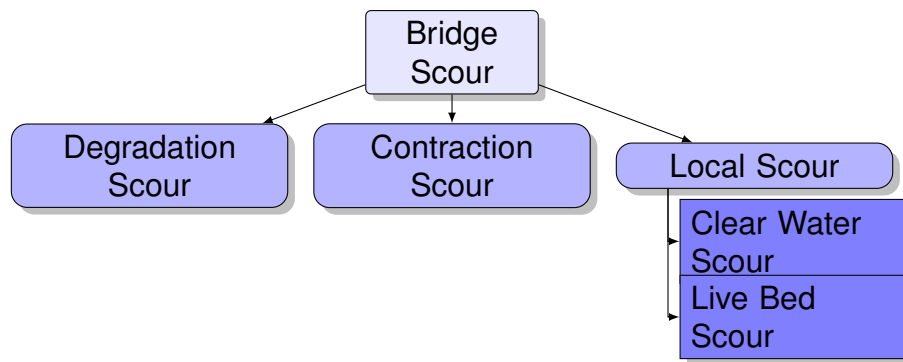


Figure 1.2: Classification of scour

Contraction scour: Natural or artificial contraction of the normal flow leads to contraction scour. It is the height difference between beds within contracted and uncontracted sections. Scour associated with contracting does not necessarily occur evenly across the entire cross-section; however, it is typically calculated as the average difference between contracted and uncontracted sections. Both lateral and vertical contractions can occur. In a pressure-flow condition, a bridge would experience vertical contraction.

Local scour: When current strikes an obstruction and moves past it, vortices form, and flow accelerates, causing local scouring. Essentially, the depth of the scour hole is the difference between where the bed would be if the obstruction weren't present and where the bed is with the obstacle. The same amount of sediment is transported from the piers to a different location. Debris accumulation on the structural pier can expand the blockage area and depth of the scour holes at both sides of the piers. When debris deflects the flow direction, local scouring is increased through the change in angle of attack. There is also a possibility that garbage can redirect the entire channel or river bed near the bridge, increasing flooding and scouring in another area.

Scour in clear water: Under clear water conditions, scour occurs when the flow of water creates greater shear stress than the critical shear stress imposed by the bed material, such as sand, gravel, or rock. Due to the lack of sediment, clear water scouring does not usually refill during the recession of the flood.

Scour in live bed: Shear stress exceeds the threshold value under scouring in live bed conditions when the sand moves upstream. Consequently, sediment continuously flows into a scour hole as part of the approach flow.

In equilibrium, the maximum scour in clear water is 10% larger than in live bed conditions in Figure 1.3 [3]. Conditions favorable to clear water scouring include:

- Coarse grains in the river bed that cannot be moved from one place to another
- In vegetated or artificially strengthened channels, local scour only occurs at high velocity
- At low flows, the slopes of the bed are flat

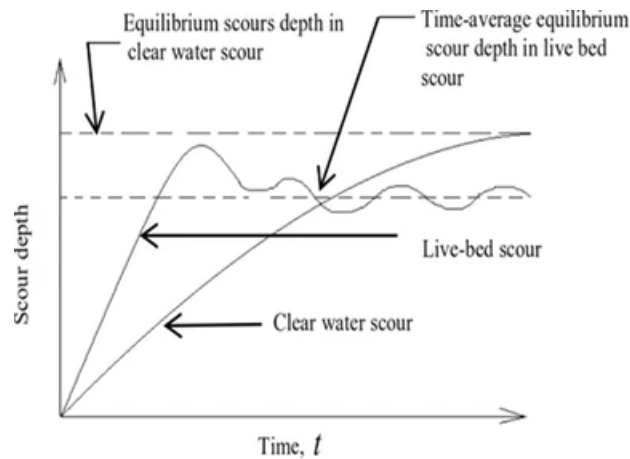


Figure 1.3: Scour depth versus time graph [3]

1.5 Scouring Mechanism

The velocity of flowing water will change when an obstruction is present. There may be differential motion in the sand particles of the river bed close to the obstacle. This is due to changes in the flow directions adjacent to a substrate. Flow velocity, the geometry of the structures, piers configurations, and substrate characteristics affect the magnitude of these changes. There is generally a deepening of the stream bed near the obstruction. The materials removed from the substrate are deposited behind or close to the obstacle, which reduces local velocity. Scour depths can be quite deep under circumstances of high water velocity, moving sand particles, and inadequately streamlined designs.

Local scour is caused by three main mechanisms:

- Accelerating flow rates and creating pressure differences in the surroundings of the construction
- Creating secondary flows through vortices
- An increase in local turbulence

There are two types of vortex flow:

- Wake and flow separation vortex, on the downstream side of the structure
- Horizontal axis vortex flow at the river bed resulting from stagnation pressure gradients along the facade of the structural pier and separation of flow in the vicinity of the scour hole.

At the intersection between a pier and its direction of flow, there is a point of stagnation where velocity ceases to be constant. This is where water flows toward the pier. There is a pressure gradient from the lowest water level to the highest water level. This is because the velocity distribution of the approaching flow varies along the bed surface from zero to maximum. A change in pressure creates a vortex at the bottom of the pillar that sweeps sediment from the

region. The vortex resembles the shape of a horseshoe. The horseshoe vortex in Figure 1.4 gets its name for that reason [4].

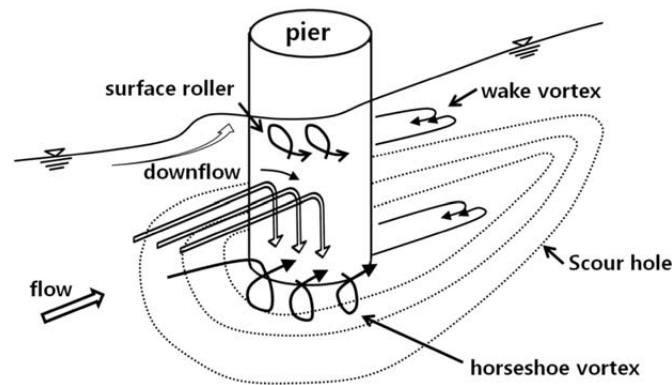


Figure 1.4: A schematic representation of the local scour around cylindrical bridge pier [4]

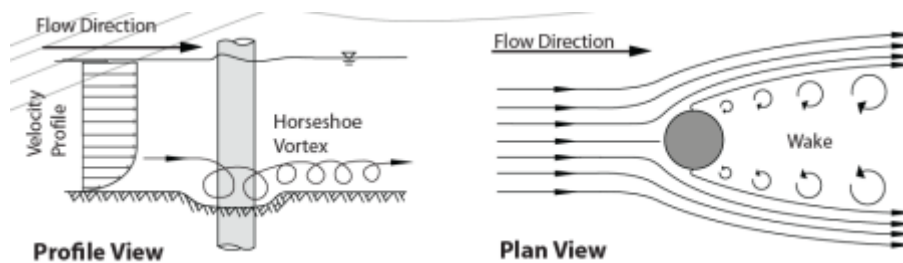


Figure 1.5: The horseshoe vortex and the wake vortex [5]

The formation of the horseshoe vortex is the primary cause of scouring. A wake vortex in Figure 1.5 also occurs at the separating region behind the pier [5]. Sediment is transported from the horseshoe vortex region and taken outside of the wake vortex region, resulting in scouring around the piers in Figure 1.4. Flow separation causes horseshoe vortices to form on the upstream portion of bridge piers. Vortices created by the upstream bridge pier affect scouring around the downstream pier. By scouring the sediment from the upstream bridge pier, these vortices deposit some sediment into the scour pit of the downstream portion of bridge piers.

1.6 Factors Affecting Bridge Scour

Several factors influence scour, including the geometry of the river bed or hydraulic flume, the fluid dynamics, the soil requirements, and the configurations of the structural piers of the bridges [5]. Using computational fluid dynamics (CFD) to simulate flow around structural piers is essential [6]. It can determine the parameters that affect sediment reduction around piers and bed scouring.

- **Effect of flow intensity:** These flow parameters include the upstream flow velocity and the angle of contact between flow and structure. Debris and sediment transport are also included. As scouring occurs between the uppermost surface and sediment bed, the approach flow depth affects the pressure gradient between them.
- **Flow shallowness:** Flow shallowness in Figure 1.6 is the ratio of flow depth to the width of the pier [7]. The mathematical representation of flow shallowness is Y/D where Y is flow depth and D is pier width. The scour depth increases proportionally with pier width for narrower piers, regardless of flow depth. In contrast, for shallower flows compared to the pier width, the scour depth rises proportionally with flow depth, regardless of pier width.

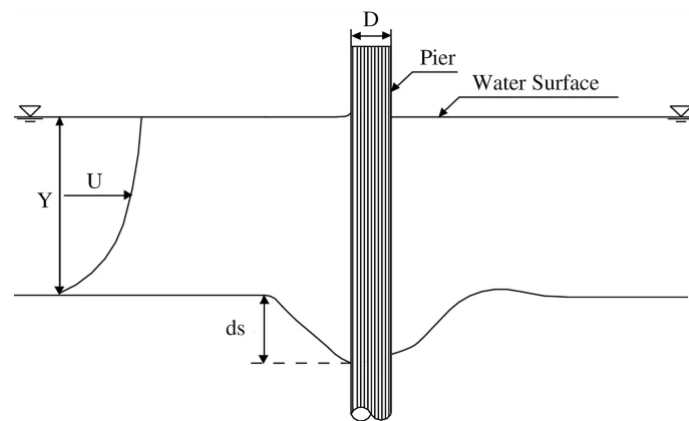


Figure 1.6: Influence of flow depth and width of the pier [7]

- **Fluid property:** Any fluid is characterized by its density ρ and viscosity ν . The density and viscosity both depend on the temperature. Typically, laboratory studies or numerical analyses take these conditions for granted at a definite ambient temperature. That is not the case in real life because the temperature of the atmosphere is constantly changing.
- **Effect of pier shape:** Scouring is strongly influenced by the shape and structure of the pier. A structure's ability to restrict the flow on its path is determined by its constriction degree. It reduced the passage area of water, which affected scouring.
- **Sediment properties:** In this case, there are two conditions: clear water scour and live bed scour. And neither of them can be predicted. Unlike scour sediments in the clear bed, scour sediments in the live bed are transported with water. Besides these, particle size, sediment distribution in non-cohesive sediments, and sediment size distribution are significant factors.
- **Floating debris:** Floating waste tends to accumulate in rivers during flooding, including trees and discarded plastic. At bridge piers, debris can accumulate into large masses of material called debris rafts. The obstruction caused by a foundation with accumulated debris is greater than without debris. In general, additional flow obstructions result in greater local scour depths than in the absence of debris accumulation.

- **Effect of time:** The process of scouring is asymptotic. During clear water scour, the scour depth approaches equilibrium gradually. In live-bed situations, the scour depth reaches equilibrium faster, oscillating as the bed materials pass the bridge pier.

To achieve equilibrium conditions, it is necessary to run laboratory experiments in clear water for several days. This will help to determine the scour depth at the equilibrium stage. If the data has been collected after less time, say after 10 to 12 hours, then the scour depth can be less than 50% of the equilibrium scour depth [8].

1.7 Research Objectives

The project's research goals are as follows:

- To investigate the fluid dynamics, scouring geometry, scour depth, bed topography, and the deposition of sediments around the bridge piers of various shapes including square, cylindrical, diamond, hexagonal sharp nose, hexagonal vertical nose, airfoil, oblong, rectangle, upstream, and downstream facing airfoil shaped piers.
- To develop a numerical model for simulating the scour depth using a commercial software.
- To reduce the scouring effect, tapered shape bridge piers will be compared with the non-tapered shape bridge piers.
- Single and multiple anti-scour collar plates wrapped around the cylindrical piers will be quantitatively examined in order to reduce the scouring impact.
- To find the efficient shape of bridge piers that produce the minimum scouring depth.

1.8 Methodology

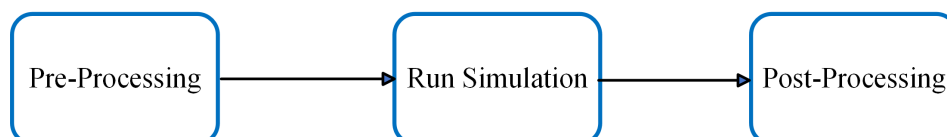


Figure 1.7: Steps in numerical analysis

- Three steps make up numerical modeling: pre-processing, simulation execution, and post-processing.

- Pre-processing comprises the creation of geometry, boundary conditions, material physical attributes, named selections, and mesh generation.
- Post-processing, however, contains the results section.

1.9 Research Outcomes

The local scouring process surrounding variously shaped bridge piers will be thoroughly analyzed to investigate which pier geometry has the lowest scour depth. The reduction of local scour will be carefully examined.

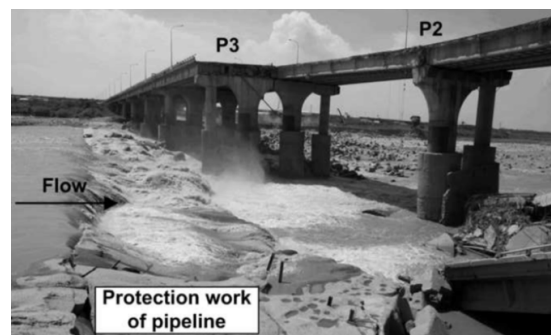
Chapter 2

Literature Review

There have been numerous bridge failures since the beginning of bridge-building thousands of years ago. Typically, foundation failures are caused by scouring in Figure 2.1, which is the loss of soil around the foundation [9]. Bridge pile foundation failures result in huge losses, including lives, economic impact, and environmental damage due to scouring. The number of studies on numerical simulations of local scours around different shapes of bridge pier is still relatively low. Even though scouring cannot be eliminated, some measures can be implemented to reduce erosion and scouring effect, which leads to the collapse of hydraulic structures. Local scour surrounding the piers is most commonly caused by horseshoe vortices. As a result of flow acceleration and a downward pressure gradient in front of the pier structure, a much higher bed shear stress causes the scouring. Many efforts are being made worldwide to reduce the failure rate of bridges. Several cases, including the scouring phenomenon, need to be addressed to guarantee the safeguard and longevity of the bridge piers, which directly impact the hydraulic structures.



Local Scour



Houfeng Bridge collapsed in Taiwan

Figure 2.1: Bridge collapse due to scouring effect [9]

There are a number of factors that affect local scour around bridge piers. To maintain a good level of control over these variables, a gradual process of development and analysis is required.

A precise prediction of the depth of scour holes around bridge piers is crucial for their safe and economical design. Several studies have explored the fluid dynamics around bridge piers and the predictability of scour depth in a uniform steady flow. In the United States, more than 500 failures of bridges were studied from 1989 to 2000 [10]. Overall, bridges failed between 1 year (under construction) and 157 years, with a life span of 52.5 years on average. The most common causes of bridge failures are structure, arrangement, construction, supervision, materials, and insufficient consideration of extreme events. From Figure 2.2, floods and scour accounted for 49% of bridge failures in the United States [11].

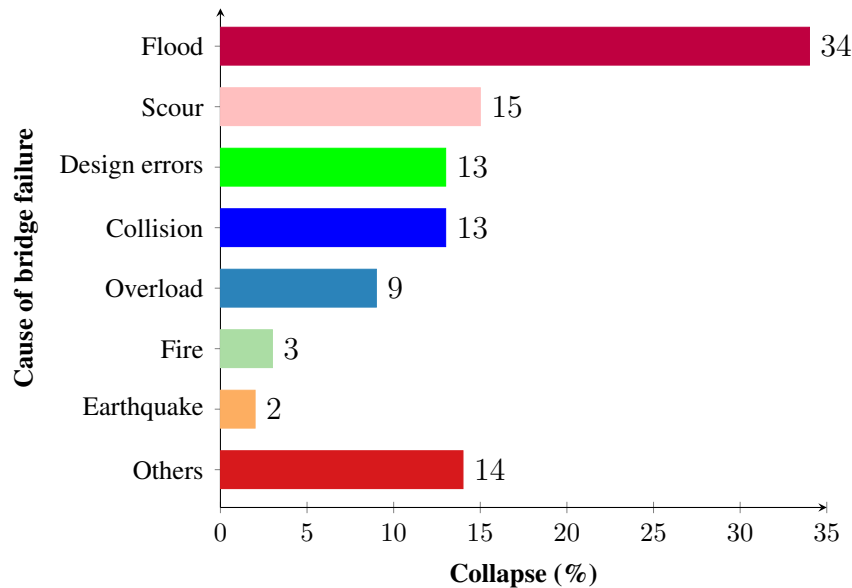


Figure 2.2: The allocation of bridge failure yields between 1989 and 2000 in the US [11]

Scouring is commonly referred to as a natural phenomenon in hydraulic structures. It is caused by the structural pier altering the fluid motion and leading to turbulence around the bridge piers [12] [13] [14]. Approximately 488,750 river bridges in the US are prone to failures caused by the scouring effect, resulting in a \$30 million annual loss [15]. On April 5, 1987, the Schoharie Creek Bridge, New York State in Figure 2.3 collapsed due to excessive scouring under bridge pile foundations, causing five vehicles to fall into the river and killing ten people [16]. Record rainfall caused the bridge to scour at its foundations, which caused it to collapse. May 21, 1988, marked the opening of the replacement bridge. On September 14, 2008, six people died due to the partial failure of the Houfeng Bridge in Figure 2.1, the most severely scour-critical bridges in Taiwan [17]. Strong winds and heavy rainfall were responsible for the collapse of the bridge. Bishopsford Road Bridge collapsed in Mitcham, London, due to a local scour on June 14, 2019 [18]. As a result of jack posts installed four days earlier, the northern arch of the bridge partially collapsed due to scour. It was completely demolished in July 2020 so that it could be rebuilt. Monitoring the scour holes around the piers of the bridge is essential when designing, operating, and maintaining hydraulic structures [19] [20]. Recently, efforts have been made to reduce scour by using piers of different shapes, geometries, and orientations [21].



Figure 2.3: Schoharie Creek Bridge Collapse [16]

An earlier study compared cylindrical piers, round-nosed rectangular piers, and triangular-nosed rectangular piers. The simulation uses many piers of the exact dimensions parallel to each other at the same time. The piers are of the same width. Scour holes deepen as horizontal distance decreases between the piers until the space-to-width ratio is 4.6 [22]. Below this value, the impact is minimal. Compared to the other two shapes, the circular pier has the greatest scouring depth. Many researchers simulated bridge scour in clear water conditions at a variety of flow velocities, volume flow rates, levels of fluid elevation, and different pier structures like cylindrical, rectangular, square, octagonal, elliptical, and lenticular. The main goal of using different pier shapes is to find the exact shape with the lowest scour depth. Several experiments have been conducted to simulate scouring caused by combined waves and currents at the complex shape of structural bridge piers [23]. While ice is covering the flow, the scouring mechanism around cylindrical bridge piers has been investigated. This has been done by varying the piers' dimensions and the grain size of the sand bed in a hydraulic flume experimental setup. The scour hole under an ice-covered flow appeared deeper and wider than one with an open channel flow. A similar flow rate suggests a much larger volume of scour holes [24].

Hexagonal, oblong, and rectangular shapes are the best for providing minimum scour [25]. Placing the foundation below bed level reduces scouring depth around bridge piers. Furthermore, a hexagonal pier is the best shape for minimizing scour due to its minimal exposed area. For piers with a small diameter, such as less than 30mm, the depth of the scour hole depends on the particle Froude Number [26]. Additionally, for larger piers, it correlates with the ratio of the diameter of the structural pier to the flow depth. Results from the experiments indicated that scour holes increased in depth with an increase in pier diameter and decreased with a decrease in pier spacing [27]. In terms of scouring reduction, piers with a length-to-width ratio of 3 performed better. Piers located at 90° create the deepest scour holes. When the pier is positioned at 90 degrees towards the innermost and outermost side of the bank, the angle of

attack increases, and so does the depth and surface area of the scour hole [28]. A round-nosed pier that faces downstream reduces local scouring [29]. Compared to the cylindrical pier, scour depth was reduced by 54%, and by 40% compared to the round-nosed pier facing upstream. In comparison to the cylindrical pier, the round-nosed pier facing downstream reduces local scour by 83%. Many experiments have been conducted to calculate scour around non-circular cylinders. In several projects, simulations of fluid dynamics and the evolution of bridge scour have been performed involving a square pier aligned 90° and 45° to the flow direction. Diamond piers are square piers with a 45° angle to the direction of flow [30]. The scour depth of cylindrical, square, diamond, airfoil and hexagonal shaped piers have been investigated, and among these piers, the cylindrical pier results in the lowest scour depth [31]. Researchers are using Artificial Neural Networks to precisely predict the scour depth around the piers and abutments [32] [33] [34]. Support Vector Machine (SVM), a Machine Learning algorithm, has been used to predict local scour [35].

In an open channel flow, vortex interactions are abundant in a turbulent horseshoe vortex (THV) system around a cylindrical shape. Turbulent horseshoe vortex systems initiate the local scouring process in front of the cylindrical structure. The evolution of THV is studied using time-resolved particle image velocimetry (PIV). Particle image velocimetry (PIV) is an optical technique used in research to visualize flow patterns. The PIV is useful for anticipating and handling the primary stages of the local scour in the front part of the cylindrical structure [36]. In a study conducted by Unger and Hager examining the flow structure around bridge piers in various Reynolds numbers and PIVs, they determined that the THV is the main reason for scouring [37].

Due to the repair costs as well as the interruption of operations, bridge failures lead to significant economic losses [38]. Scientists and researchers have been working to minimize the possibility of scouring and the powerful effect of the horseshoe vortex nearby bridge pillars, which is one of the leading causes of scouring. A further twenty million dollars were estimated to have been invested in scour research in the United States during the past two decades [39]. According to the Federal Highway Administration, about 60,000 out of the 600,000 bridges in the United States were in poor condition in 2009 [40]. By 2020, that number dropped to 45,000, despite a slight rise in the number of bridges in the country. Most scour-related bridge failures have occurred where the structure had been deemed "scour-resistant". Natural disasters are likely to worsen scouring situations. The risk of scour can be reduced by investing in better monitoring and countermeasures.

Hence, the primary goal of this study is to investigate the fluid dynamics, velocity magnitude, contour plots, scouring geometry, time-dependent analysis of scour depth, and sand deposition around the bridge piers of various shapes including cylindrical, square, diamond, hexagonal, airfoil, oblong, rectangle, and tapered shape to find out which one is more efficient to implement as a pillar in bridges construction across the globe. Several advantages of numerical methods

include their simplicity, low cost, and relatively low time consumption, as well as their high accuracy, making them a particularly valuable tool for the prediction of likely failures. Simulation software employs computational fluid dynamics (CFD) for solving Navier-Stokes and continuity equations in flow simulations [41]. Flow-3D is a CFD software capable of modeling sediment scour and free surface flow. With the use of numerical technologies, Flow-3D simplifies the solution of computational fluid dynamics equations through transient, 3D, and 2D multiphysics flow difficulties [42]. The Navier-Stokes equation for free surface flow is numerically solved by Flow-3D's volume of fluid (VOF) method. FAVOR (fractional area-volume obstacle representation) method is used to mesh complex geometries [43]. For this reason, Flow-3D is selected to create a 3D model and simulate the effect of turbulence on sediment transportation and scouring around the varying shapes of the structural piers.

Chapter 3

Design and Simulation

3.1 Governing Equations

Different shaped bridge piers have been simulated using FLOW 3D. At every time step that the user is incorporating, the total volume of the packed sediment and its area fraction is calculated. Bed shear stress, critical shield parameter, sediment entrainment and deposition, bedload transport, and suspended load transport are calculated at each mesh cell of the river bed to predict the local scouring process. The software also analyzes the contour plot, packed sediment elevation net change along with different directions, velocity magnitude of the fluid flow, and 3D view of the model.

3.1.1 Bed Shear Stress

The shear stress defines the movement of bed loads and sediment transport. Bed shear stress is an effective hydraulic parameter for estimating sediment transport. For 3D turbulence flow, it is measured by wall function from Equation (3.1).

$$u = u_\tau \left[\frac{1}{\mathcal{K}} \ln \ln \left(\frac{Y}{\frac{y}{u_\tau} + k_s} \right) \right] \quad (3.1)$$

$$u_\tau = \sqrt{\frac{\tau}{\rho}} \quad (3.2)$$

$$\mathcal{K} = 0.4 \quad (3.3)$$

Where,

U = Velocity

U_τ = Shear velocity

τ = Bed shear stress

ρ = Bulk density of the fluid-sediment mixture

Y = Distance from the wall

ν = Kinematic viscosity

\mathcal{K} = Von Karman Constant

$$k_s = C_s d_{50} \quad (3.4)$$

$$C_s = 2.5 \quad (3.5)$$

Where,

d_{50} = Median grain diameter

C_s = User defined coefficient related to the shape and smoothness of the grains

3.1.2 Critical Shields Parameter

In fluid flow, the Shields number, also known as the Shields parameter or Shields criterion, is a nondimensional number used to determine the onset of sediment motion. In other words, it is the nondimensionalization of shear stress.

$$\theta_n = \frac{\tau}{gd_n(\rho_n - \rho_f)} \quad (3.6)$$

Where,

θ_n = The Shields parameter

g = Gravitational constant

ρ_n = Density of the sediment

ρ_f = Density of the fluid

d_n = Grain diameter

n = Number of nth sediment species

$$\theta_{cr,n} = \frac{\tau_{cr,n}}{gd_n(\rho_n - \rho_f)} \quad (3.7)$$

$$\theta_{cr,n} = \frac{0.3}{1 + 1.2d_{*,n}} + 0.055(1 - e^{-0.02d_{*,n}}) \quad (3.8)$$

$$d_{*,n} = d_n \left[\frac{g(S_n - 1)}{\nu f^2} \right] \quad (3.9)$$

$$S_n = \frac{\rho_n}{\rho_f} \quad (3.10)$$

Where,

$d_{*,n}$ = Dimensionless grain diameter

ν_f = Kinematic viscosity of the fluid

$\theta_{cr,n}$ = Critical Shields parameter

$\tau_{cr,n}$ = Critical shear stress

It is essential to define the shield parameters at the critical bed shear stress when sediments move in the bed. Considering both entrainment as well as bedload transport, the Equation (3.6) can be written as Equation (3.7).

The value of $\theta_{cr,n}$ is computed based on the assumption that the grains are evenly distributed within the bed. Users can either input their own values (default value 0.05) or use the Soulsby Whitehouse Equation (3.8) to calculate $\theta_{cr,n}$ [44]. Soulsby and Whitehouse propose this alternative form, also obtained by fitting the Shields curve.

3.1.3 Entrainment and Deposition

Entrainment refers to particles being carried over from the fluidized bed. The sediment in a flow may move from one point to another as bedload in sliding and rolling grains or suspended load

transferred by the main flow. It is also possible that some sediment materials will flow downstream in a wash load from upstream reaches. In contrast with suspended loads, wash loads contain sediment that does not interact with bed loads. Water moves with the mean velocity of the main stream as the wash load is carried within the water column. As for deposition, it occurs when sediments from the outside area accumulate in the packed bed due to friction, gravity, and buoyancy effects.

Entrainment and deposition of sediment are considered to be opposing micro-processes that occur simultaneously. The net exchange rate for suspended and packed sediment is calculated by adding these two effects together. During entrainment, the velocities by which sediments move away from the packed bed are called lifting velocities. And this velocity can be calculated by Winterwerp et al. (1992), which is explained in Equation (3.11). The settling velocity in Equation (3.12) of Soulsby (1997) is used in the sand deposition.

$$\mathcal{U}_{\text{lift},n} = n_b \alpha_n d_{*,n}^{0.3} (\theta_n - \theta_{cr,n})^{1.5} \sqrt{g d_n (S_n - 1)} \quad (3.11)$$

$$\mathcal{U}_{\text{settle},n} = \frac{g}{g} [(10.36^2 + 10.49 d_{*,n}^3)^{1/2} - 10.36]^{v_f/d_n} \quad (3.12)$$

$$\alpha_n = 0.018 \quad (3.13)$$

Where,

α_n = Entrainment coefficient of species n

n_b = Outward normal vector of the packed sediment bed surface

$\mathcal{U}_{\text{settle},n}$ = Settling velocity

$\mathcal{U}_{\text{lift},n}$ = Lifting velocity

3.1.4 Bed Load Transport

The bed load rolls, glides, and bounces over the sand bed. According to theory, bedload constitutes 5% to 10% of the total sediments in a flow, making it insignificant when compared to the amount of sediment as a whole. In rivers, those having gravels bed, the bed material load (bedload plus suspended load derived from bed material) is primarily dominated by bed load. A bed material load is the only one that actively interacts with the sediment load. Because the bed load is such a vital component, it significantly affects the river bed or channel's morphology.

In general, bedload transport rate is a function of excess dimensionless shear stress. This Equation (3.14) illustrates the dimensionless transport parameter for bedloads. The Meyer-Peter and Muller (1948) Equation (3.15) is used to calculate the value of Φ_n [45]. The original equation of Meyer-Peter and Muller does not include $\mathcal{C}_{b,n}$. The addition of this variable allows for the

effects of several species to be taken into account. Van Rijn (1984) suggests that the thickness of the bedload layer h_n can be predicted based on Equation (3.18).

$$\Phi_n = \frac{q_{b,n}}{\sqrt{[g(S_n - 1)d_n^3]}} \quad (3.14)$$

$$\Phi_n = B_n(\theta_n - \theta_{cr,n})^{1.5} C_{b,n} \quad (3.15)$$

$$C_{b,n} = \frac{\text{Total volume of } n \text{ species}}{\text{Total volume of all species}} \quad (3.16)$$

$$\sum_{n=1}^N C_{b,n} = 1 \quad (3.17)$$

$$h_n = 0.3d_n d_{*,n}^{0.7} \left(\frac{\theta_n}{\theta_{cr,n}} - 1 \right)^{0.5} \quad (3.18)$$

$$\mathcal{U}_{b,n} = \frac{q_{b,n}}{h_n C_{b,n} f_b} \quad (3.19)$$

Where,

$q_{b,n}$ = Volumetric bed load transport rate of size class n per unit channel width b

Φ_n = Transport stage

B_n = Bed load coefficient

$C_{b,n}$ = volume fraction of species n

N = Total number of species

h_n = Bed load layer thickness

$\mathcal{U}_{b,n}$ = Bed load velocity

f_b = The total packing fraction of sediment

Table 3.1: Bed load coefficient for different transport type

Transport Type	Bed Load Coefficient (B_n)
Low transport	5-5.7
Intermediate transport	8
High transport	13

The literature analysis of Flow 3D shows that the most common value for bed load coefficient is 8.0 for intermediate transport. Here are the details of the bed load coefficient value in Table 3.1.

3.1.5 Suspended Load Transport

Most of the suspended load transports at a greater fraction of the average flow velocity in the stream, and this load travels through the downward and central areas of the stream. Solving the transport equation for individual species will give the concentration of suspended sediment. Unlike fluids and other species, individual sediment species in suspension move at their own speed. This is because grains with varying mass densities and sizes experience dissimilar drag forces. FLOW-3D can solve the main suspended load transportation equation by using Equation (3.20) to Equation (3.23).

$$\frac{\partial C_{s,n}}{\partial t} + \nabla \cdot (C_{s,n} \mathcal{U}_{s,n}) = \nabla \cdot \nabla (DC_{s,n}) \quad (3.20)$$

$$C_{s,n} = \frac{C_{s,n}}{\rho_n} \quad (3.21)$$

$$\bar{\rho} = \sum_{m=1}^N C_{s,m} \rho_{s,m} + (1 - C_{s,tot}) \rho_f \quad (3.22)$$

$$C_{s,tot} = \sum_{m=1}^N C_{s,m} \quad (3.23)$$

Where,

$C_{s,n}$ = Mass concentration of suspended sediment

D = Diffusivity

$\mathcal{U}_{s,n}$ = Sediment velocity of species n

$\bar{\rho}$ = Mass density of fluid-sediment mixture

$C_{s,tot}$ = Total volume concentration of suspended sediment

3.2 Turbulence Modeling With FLOW-3D

FLOW-3D offers a wide variety of turbulence models, including 3D flows, 2D flows, and hybrid 3D/2D flows. FLOW-3D includes eight different turbulence models.

- Prandtl mixing length model
- One-equation Model
- Standard k- ϵ model

- Renormalized Group (RNG) k- ϵ model
- k- ϵ two-equation model
- LES model
- 2D depth-averaged shallow water turbulence model
- Second 2D depth-averaged shallow water turbulence model

Yakhot and Orszag (1986), Yakhot and Smith (1992) developed the Renormalized Group (RNG) k- ϵ model. The RNG turbulent model is recommended in most industrial problems since it is a more effective alternative to the k- ϵ two-equation model. According to Yakhot et al., smaller scales of movement have significant impacts. He suggested the RNG model. It renormalizes Navier-Stokes equations by using Renormalisation Group (RNG) methods. The eddy viscosity of turbulence in the k- ϵ model is derived from a single turbulence length scale, resulting in turbulent diffusion occurring at a single length scale. Turbulent diffusion, however, can take place at any scale. One can derive a turbulence model using the RNG approach, and this RNG turbulence model will be identical to the k- ϵ model. The RNG model uses an improved version of the Epsilon equation, which changes the production term depending on the various scale of motion. With its extended capabilities, it covers transitionally turbulent flows, wall heat transfer, mass transfer, and curving flows better than the standard k- ϵ model. Herein, transport equations [46] are shown in Equation (3.24) to Equation (3.28).

$$\frac{\partial}{\partial t}(\rho k) + \frac{\partial}{\partial x_i}(\rho k u_i) = \frac{\partial}{\partial x_j} \left[\left(\mu + \frac{\mu_t}{\sigma_k} \right) \frac{\partial k}{\partial x_j} \right] + P_k - \rho \epsilon \quad (3.24)$$

$$\frac{\partial}{\partial t}(\rho \epsilon) + \frac{\partial}{\partial x_i}(\rho \epsilon u_i) = \frac{\partial}{\partial x_j} \left[\left(\mu + \frac{\mu_t}{\sigma_\epsilon} \right) \frac{\partial \epsilon}{\partial x_j} \right] + C_{1\epsilon} \frac{\epsilon}{k} P_k - C_{2\epsilon}^* \rho \frac{\epsilon^2}{k} \quad (3.25)$$

$$C_{2\epsilon}^* = C_{2\epsilon} + \frac{C_\mu \eta^3 (1 - \eta/\eta_o)}{1 + \beta \eta^3} \quad (3.26)$$

$$\eta = S k / \epsilon \quad (3.27)$$

$$S = (2 S_{ij} S_{ij})^{1/2} \quad (3.28)$$

In the RNG turbulent model, every constant (except β) is derived explicitly. These values are shown below (standard k- ϵ equation). The RNG k- ϵ models expand the capabilities of the k- ϵ model by providing better results for low-intensity turbulence and intense shear stress regions [47] [48].

$$C_{\mu} = 0.0845(0.09)$$

$$\sigma_k = 0.7194(1.0)$$

$$\sigma_{\epsilon} = 0.7194(1.30)$$

$$C_{\epsilon 1} = 1.42(1.44)$$

$$C_{\epsilon 2} = 1.42(1.92)$$




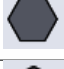








$$\eta_o = 4.38$$

$$\beta = 0.012(\text{Derived from experiment})$$

3.3 Geometry Of Bridge Pier Structure

This study uses twelve different types of bridge piers. These are cylindrical, square, diamond, hexagonal-sharp nose, hexagonal- vertical nose, airfoil, oblong, rectangle, upstream facing airfoil, downstream facing airfoil, tapered cylindrical, and tapered hexagonal- sharp nose in Table 3.2. Modeling the geometry of the piers has been done using SOLIDWORKS in Figure 3.1. The STL files of the 3D model are imported into FLOW-3D for individual simulation to complete the meshing and geometry part of the model setup.

Table 3.2: Top view of the bridge piers

Top View	Pier Geometry
	Cylindrical
	Square
	Diamond
	Hexagonal- Sharp Nose
	Hexagonal- Vertical Nose
	Airfoil
	Upstream Facing Airfoil
	Downstream Facing Airfoil
	Oblong
	Rectangle
	Taper Cylindrical
	Taper Hexagonal- Sharp Nose

3.3.1 Sketch And Dimensions

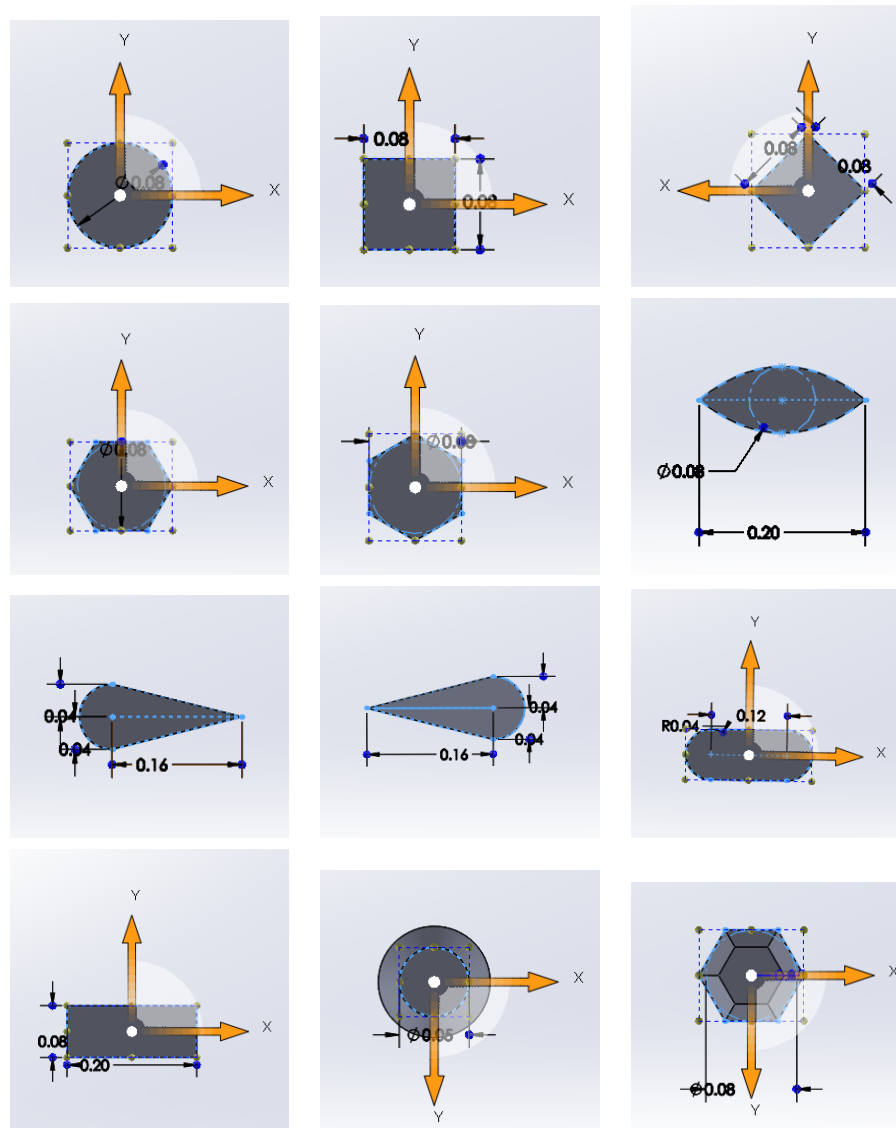


Figure 3.1: 2D sketch of pier shapes in SOLIDWORKS

In the case of cylindrical piers in Table 3.3, 8cm is taken as the diameter. For square piers, the edge length equals 8cm . A square shape pier rotated at a 45° angle will become a diamond shape pier. This pier has the same edge length as a square pier. Two types of regular hexagonal-shaped piers have been simulated in this study. The first has a sharp nose, and the second has a vertical nose facing the flow direction. This hexagonal pier's inscribed circle measures 8cm in diameter, and its edge is 5cm long. Cylindrical, square, diamond, and hexagonal piers have X- and Y-axis lengths ranging from 8cm to 11cm .

The airfoil pier has a streamlined shape. Airfoil pier also has two options. An upstream facing airfoil with a sharp end and a downstream facing airfoil with a sharp leading edge. From Table 3.3, the inscribed circles of these airfoils are 8cm in diameter. An oblong pier has two round noses at the trailing edge and leading edge. The airfoil, oblong, rectangle, upstream,

and downstream facing airfoil piers have a length of 2cm along the X-axis and 8cm along the Y-axis. All of the piers are 35cm high in Z-direction.

Table 3.3: Dimensions of the piers along X,Y, Z axis for non-tapered shape

Pier Geometry	Length $x(m)$	Width $y(m)$	Height $z(m)$	Diameter (m)	Edge (m)	Length
Cylindrical	0.08	0.08	0.35	0.08	–	
Square	0.08	0.08	0.35	–	0.08	
Diamond	0.11	0.11	0.35	–	0.08	
Hexagonal-sharp nose	0.09	0.08	0.35	0.08	0.05	
Hexagonal-vertical nose	0.08	0.09	0.35	0.08	0.05	
Airfoil	0.20	0.08	0.35	0.08	–	
Oblong	0.20	0.08	0.35	–	–	
Upstream facing airfoil	0.20	0.08	0.35	0.08	–	
Downstream facing airfoil	0.20	0.08	0.35	0.08	–	
Rectangle	0.20	0.08	0.35	–	–	

For the tapered cylindrical pier, the diameter of the base is $D_1=8\text{cm}$, and the top surface is $D_2=5\text{cm}$ which is the same as a tapered hexagonal- sharp nose pier. The height of the piers is 35cm in the Z direction. The tapered angle for both of the piers is 2.45° , which is calculated using Equation (3.29). The dimensions of the tapered shape are given in Table 3.4.

$$\tan \alpha = \frac{D_1 - D_2}{2z} \quad (3.29)$$

where

D_1 = Larger diameter of the tapered shape

D_2 = Smaller diameter of the tapered shape

z = Height of the tapered shape

Table 3.4: Dimensions of the piers along X,Y, Z axis for tapered shape

Pier Geometry	Length $x(m)$	Width $y(m)$	Height $z(m)$	Diameter (m)	Taper Angle
Taper cylindrical	0.08-0.05	0.08-0.05	0.35	0.08-0.05	2.45°
Taper hexagonal-sharp nose	0.09-0.06	0.08-0.05	0.35	0.08-0.05	2.45°

3.4 Numerical Modeling Of The River Bed

This section includes the geometry of the river bed, boundary conditions, mesh planes, mesh generation, and grid test.

3.4.1 Dimension Of The River Bed

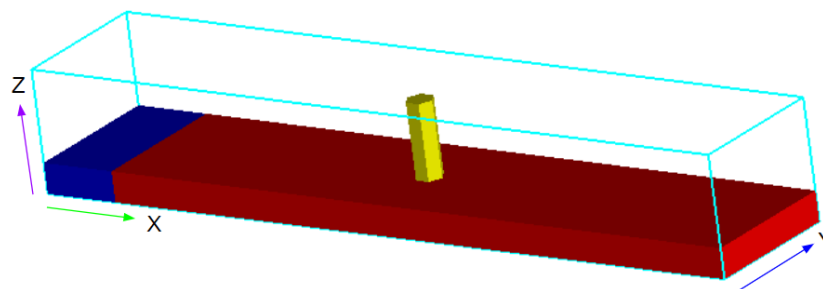


Figure 3.2: River bed with outlines

The river bed in Figure 3.2 includes two parts, the solid block, and the sand bed. In the inlet section, a solid block of $25\text{cm}/50\text{cm}/10\text{cm}$ has been placed to reduce turbulence. The sand bed has dimensions of $225\text{cm}/50\text{cm}/10\text{cm}$. So the overall dimension of the river bed is- the length of the bed is 250cm , the width of the bed is 50cm , and sand height is 10cm . The hydraulic flume is 250cm long, 50cm wide, and 35cm high. Dimensions are given in Table 3.5. The piers are located in the middle of the river bed, $(x, y) = (1, 0.25)$ from Table 3.6. A total of 12 different single piers have been used for simulation.

Table 3.5: Dimensions of the river bed along X,Y, Z axis

Part	Length $x(m)$	Width $y(m)$	Height $z(m)$
Solid block	0.25	0.5	0.10
Sand bed	2.25	0.5	0.10
River bed	2.50	0.5	0.10
Hydraulic Flume	2.50	0.5	0.35

Table 3.6: Placement of pier in the river bed

Centre of The River Bed (m)	From Inlet (m)	From Outlet (m)
$(x, y) = (1, 0.25)$	1.25	1.25

3.4.2 Sediment Scour Model

An evenly grading layer of non-cohesive sand covers the flume for 10cm with a mean particle diameter of $d_{50}=0.85mm$ and density is $1602kg/m^3$ from Table 3.7. The sediment bed and the sidewalls of the flumes are smooth, and there is no roughness.

Table 3.7: Sediment scour model in SI unit

Name	Diameter	Density	Critical Shields Number	Entrainment Coefficient	Bed Load Coefficient	Angle of Repose
Sand	0.00085	1602	0.05	0.018	8	32°

3.4.3 Boundary Conditions

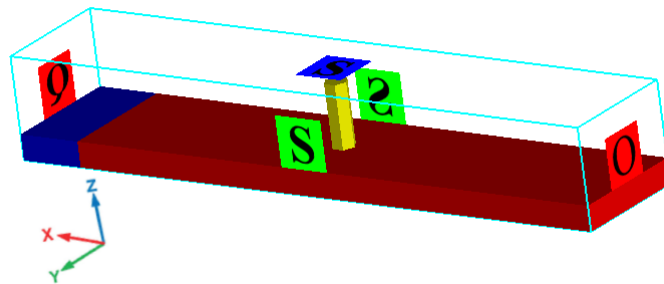


Figure 3.3: Boundary conditions

X Min is the inlet boundary conditions in Figure 3.3 which is the volume flow rate of water $0.01m^3/s$. X flow direction vector is 1, Y and Z flow direction vectors are 0. From Table 3.9, fluid is water at 20° and fluid elevation is 2cm. The outlet BC is defined as outflow. Symmetry boundary conditions are used for sides of the flume, which are Y Min, Y Max, and Z Max. The base of the flume is Z Min, where the Wall boundary condition is used. Boundary conditions are given in Table 3.8. Volume flow rate has been calculated using Equation (3.30). Cross-sectional area of the flume is 0.125m and flow velocity is 0.12m/s.

$$Q = AV \quad (3.30)$$

Where,

Q = Volume flow rate

A = Cross-sectional area of the flume

V = Flow velocity

Table 3.8: Boundary Conditions

Boundaries	Conditions
X Min	Volume flow rate (vfr)
X Max	Outflow (O)
Y Min	Symmetry (S)
Y Max	Symmetry (S)
Z Min	Wall (W)
Z Max	Symmetry (S)

Table 3.9: Volume flow rate and fluid elevation

Name	Values
Vfr	$0.01m^3/s$
Fluid	Water at 20°
Fluid Elevation	$0.2m$
Sand Height	$0.1m$

3.4.4 Mesh Generations And Mesh Planes

In mesh generation, continuous geometric shapes are split into discrete geometric cells. A simplicial complex is often formed by these cells. The geometric input domain is usually divided into discrete cells, and mesh cells provide a discrete localization of the larger domain. Computational fluid dynamics (CFD) and finite element analysis (FEA) use meshes to simulate problems. The meshes in this study are made up of simple cells, such as quadrilaterals or hexahedrons. For meshing, a total cell instead of a cell size is used.

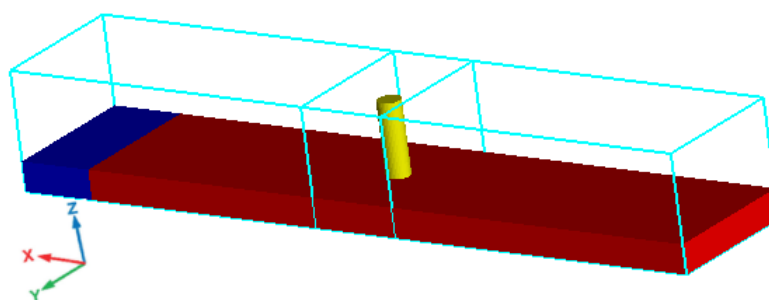


Figure 3.4: Location of mesh planes for Cylindrical pier

From Figure 3.4, along X-axis there are four mesh planes- mesh plane 1 at $x=-0.25m$, mesh plane 2 at $x=0.85m$, mesh plane 3 at $x=1.15m$, and mesh plane 4 at $x=2.25m$. There are two mesh planes in the Y direction- mesh plane 1 at $y=0m$ and mesh plane 2 at $y=0.5m$. Furthermore, in the Z direction, there are two mesh planes- mesh plane 1 at $z=0m$ and mesh plane 2 at $z=0.4m$. These locations of mesh planes in Figure 3.4 are the same for cylindrical, square, diamond, and hexagonal shape piers.

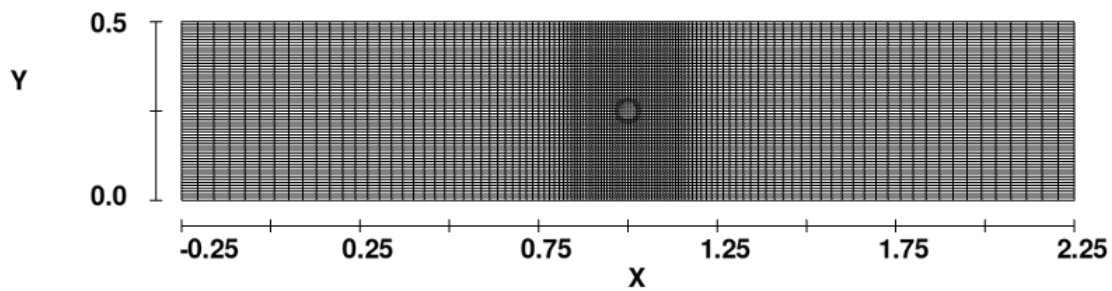


Figure 3.5: Meshing in XY plane for Cylindrical pier

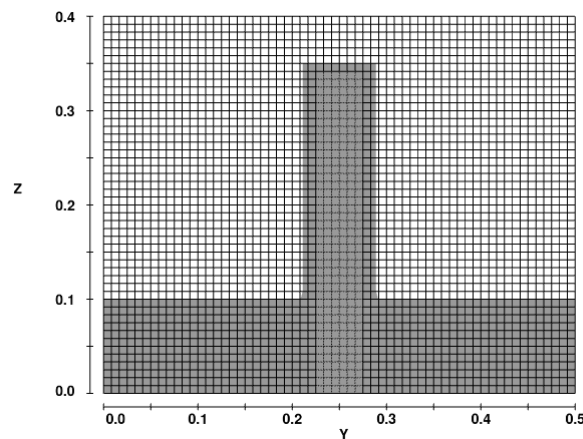


Figure 3.6: Meshing in YZ plane for Cylindrical pier

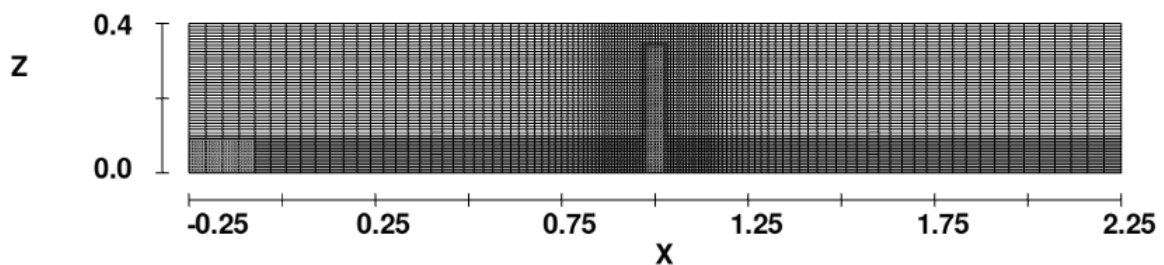


Figure 3.7: Meshing in ZX plane for Cylindrical pier

The total number of cells in the X direction between mesh planes 1 and 2 is 40, mesh plane 2 and 3 is 36, and between mesh planes 3 and 4 is 40. So, the total cell in the X direction is 116 in Figure 3.5. In the Y and Z directions, the total number of cells is 60 in Figure 3.6 and 48 in Figure 3.7 respectively. The total number of cells along the X, Y, Z axis have been increased within the scour-poor region, mainly around the pier, to enhance the accuracy of the simulation. From Table 3.10, the total mesh cell in the domain is 334080 in Figure 3.8.

From Figure 3.9, along X-axis there are four mesh planes- mesh plane 1 at $x=-0.25m$, mesh plane 2 at $x=0.8m$, mesh plane 3 at $x=1.2m$, and mesh plane 4 at $x=2.25m$. There are four mesh planes in the Y direction- mesh plane 1 at $y=0m$, mesh plane 2 at $y=0.1m$, mesh plane 3

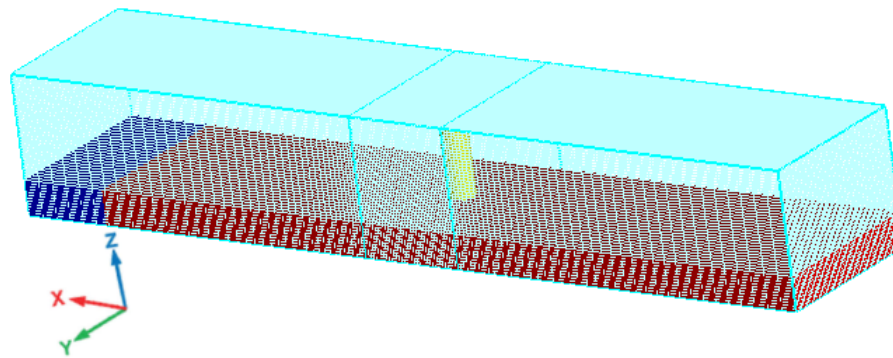


Figure 3.8: Total mesh cells in 3D domain for Cylindrical pier

Table 3.10: Total mesh cells in the domain

Pier Shape	Total Cell in X, Y, Z Axis	Total Mesh Cells
Cylindrical, square, diamond, hexagonal	$116 \times 60 \times 48$	334080
Airfoil, oblong, rectangle	$140 \times 50 \times 48$	336000

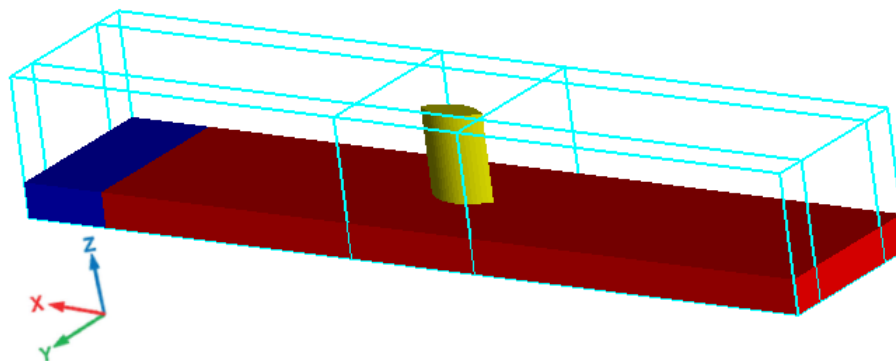


Figure 3.9: Location of mesh planes for airfoil pier

at $y=0.4m$, and mesh plane 2 at $y=0.5m$. Furthermore, in the Z-direction, there are two mesh planes- mesh plane 1 at $z=0m$ and mesh plane 2 at $z=0.4m$. These locations of mesh planes in Figure 3.9 are the same for the airfoil, oblong, and rectangle piers.

The total number of cells in the X direction between mesh plane 1 and 2 is 46, mesh plane 2 and 3 is 48, and between mesh planes 3 and 4 is 46 and in the Y direction between mesh planes 1 and 2 is 7, mesh plane 2 and 3 is 36, and between mesh plane 3 and 4 is 7. So, total cells in the X direction is 140 in Figure 3.10 and in the Y direction is 50 in Figure 3.11. In the Z direction, the total number of cells is 48 in Figure 3.12. From Table 3.10, total mesh cell in the domain is 336000 in Figure 3.13.

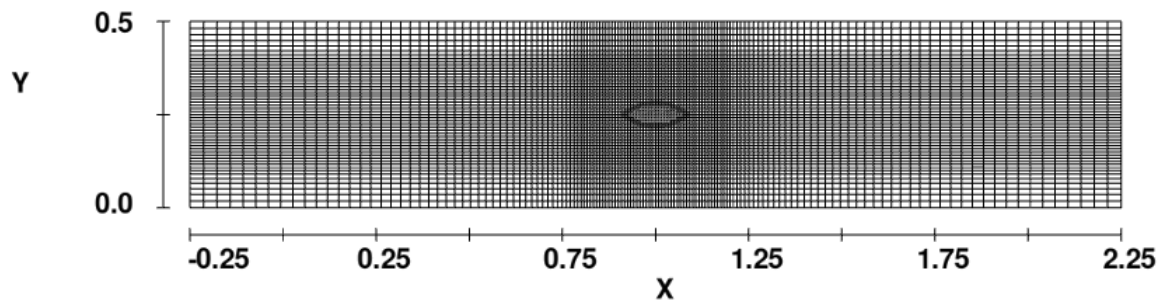


Figure 3.10: Meshing in XY plane for Airfoil pier

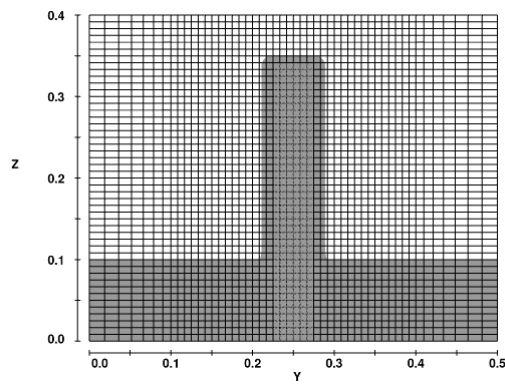


Figure 3.11: Meshing in YZ plane for Airfoil pier

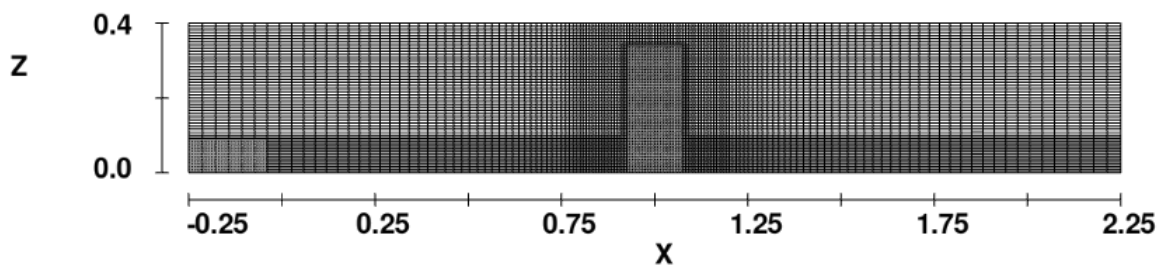


Figure 3.12: Meshing in ZX plane for Airfoil pier

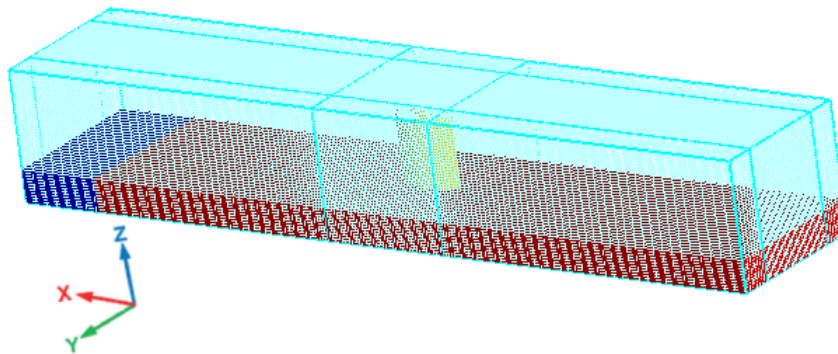


Figure 3.13: Total mesh cells in 3D domain for Airfoil pier

For each of the geometries of the piers, these numerical simulations have been performed in clear water conditions. Measurement of sediment bed elevation is taken prior to the numerical analysis. The simulations have been run until equilibrium conditions are reached for each case. The finish time is 1000s, and the initial time step is 0.01s.

3.5 Grid Independence Test

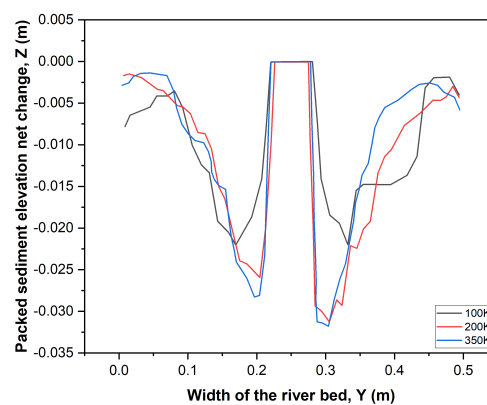


Figure 3.14: Grid independent test for cylindrical pier

The grid independence test uses various grid conditions to find the best grid condition with the least number of grids without generating a difference in numerical results. Unless a solution is grid-independent, it should not be accepted. The process involves repeating a computer run with finer and finer grids until all points in space show the same results.

In the case of cylindrical piers, the grid independence test has been achieved. The rectangular and square structured meshes extend over the river bed and the structural piers. To discretize the governing equations, several cells have been defined. The grid resolution has changed from

Table 3.11: Number of cells in X, Y, Z directions

Grid	Total Cell in X, Y, Z Axis	Total Mesh Cells	Approximate Mesh Cells
A	$94 \times 40 \times 32$	120320	100000
B	$102 \times 50 \times 40$	204000	200000
C	$116 \times 60 \times 48$	334080	350000

coarser to finer cells.

From Figure 3.14, there are three grid tests on a cylindrical pier, A (coarsest), B (less coarse and less fine), and C (finest). The Table 3.11 explains the details of the various computational grids, including their numbers.

The results in Figure 3.14 demonstrate that A (the coarsest) with a total of 100k mesh cells is unable to predict the scour depth effectively. This is because B (with 200k) and C (with 350k) yield close scour depth results, sufficient to conduct grid independence. The most refined grid C has been selected as the preferred one to run the remaining simulations for other structural piers. These cases have been simulated until they reached the equilibrium condition using time-accurate simulations.

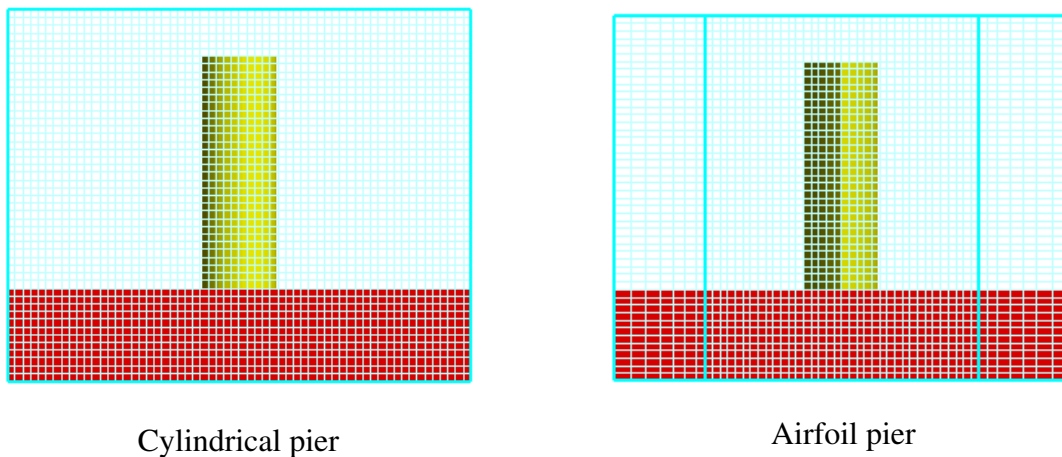


Figure 3.15: Mesh cells size at the surroundings of the pier in the YZ plane

3.6 Validation

The numerical analysis of the experimental result for the cylindrical and diamond-shaped piers has been compared from an article published in *Advances in Water Resources* [49]. The length of the hydraulic flume is $10m$, and it has a rectangular cross-section of $1.21m$ by $45cm$. It contains sand of $20cm$ deep, and the mean particle diameter is $d_{50} = 0.85mm$. The diameter of the cylindrical pier is $16.51cm$ and the width of the diamond-shaped pier is $23.35cm$.

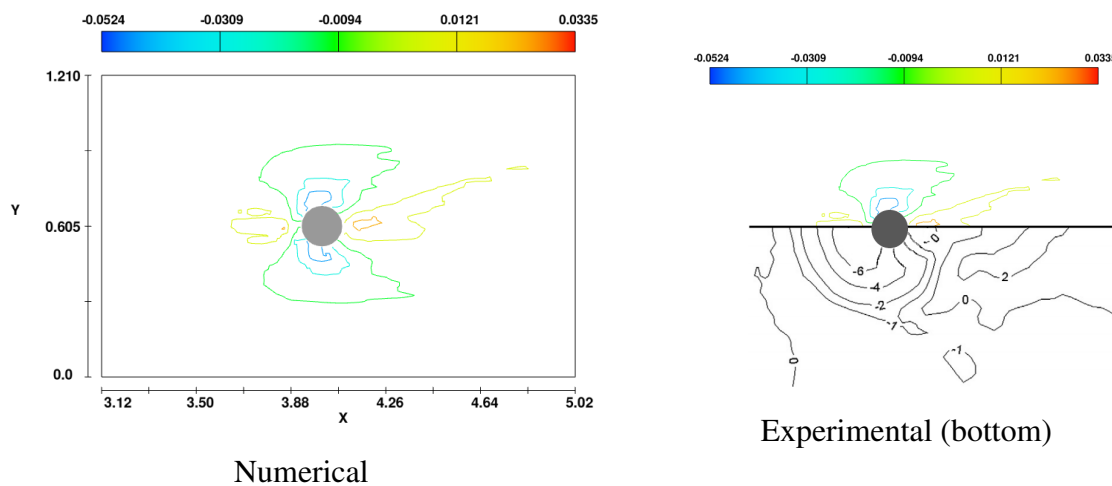


Figure 3.16: Numerical and experimental comparison among the scour depth contour plot of Cylindrical shaped pier

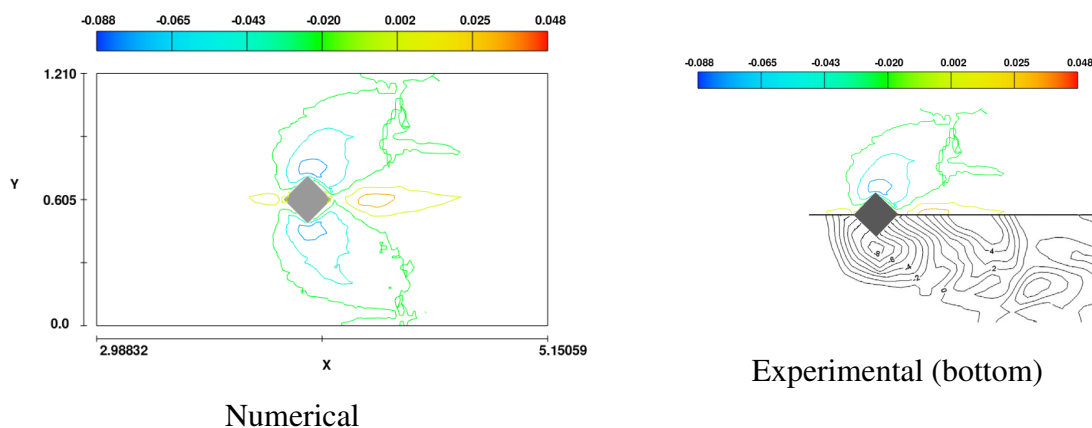


Figure 3.17: Numerical and experimental comparison among the scour depth contour plot of Diamond shaped pier

According to the contour plot, the capability of the FLOW-3D software is dependent on the geometrical characteristics of the structural piers. For cylindrical and diamond-shaped piers in Figure 3.16 and Figure 3.17, FLOW-3D offers a better prediction of scour depth. The comparison between numerical and experimental result has been shown in Table 3.12.

Table 3.12: Numerical and experimental comparison of scour depth

Pier Geometry	Numerical (cm)	Experimental (cm)	Percentage Change
Cylindrical	5.24	6	-12.67%
Diamond	8.80	8	+10%

Chapter 4

Results and Discussions

4.1 Scour Depth And Sand Deposition Analysis

This section illustrates the scour depth and entrainment of sediments for the various shapes of structural piers in 1D, 2D, and 3D views, along with the bed topography of the river bed.

4.1.1 Cylindrical Shaped Pier

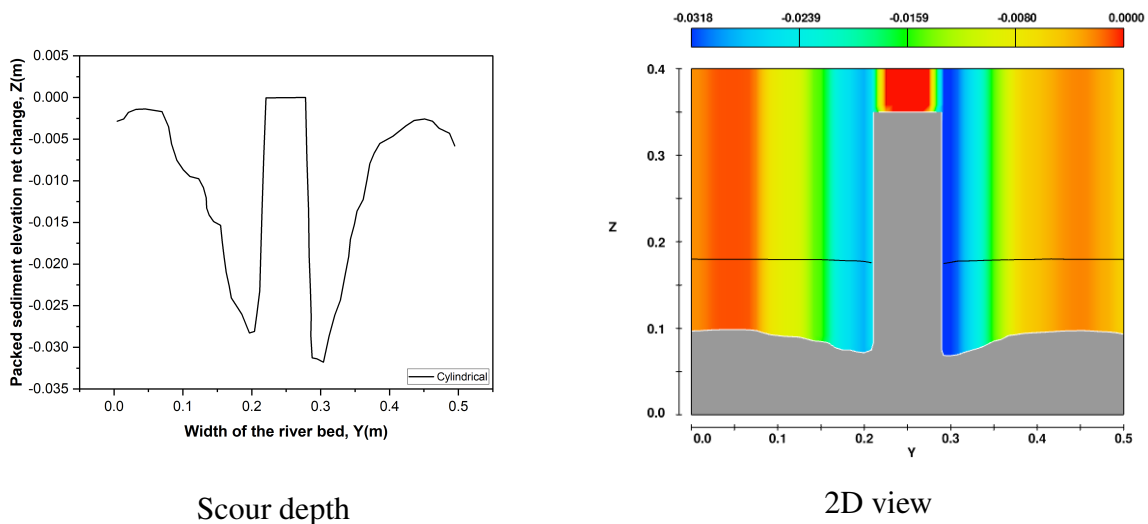


Figure 4.1: Packed sediment elevation net change for Cylindrical pier in YZ plane

From Figure 4.1, the maximum scour depth for the cylindrical pier is 3.18cm . Figure 4.2 shows the 3D view of the scour depth for the cylindrical pier. The negative numerical values indicate local scour depth, whereas the positive numerical value indicates sand depositions.

Figure 4.3 shows entrainment and deposition of sand along the length of the river bed. Be-

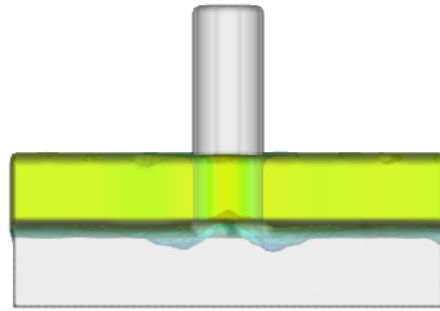


Figure 4.2: 3D Scour depth for the cylindrical pier with a fraction of fluid

cause of the high velocity of water at the inlet, a hole of 1.65cm has been created just after the solid block. On the X-axis, relatively few sediments 1.37cm has been removed from the pier's upstream adjacent area along with the flow. Sediment depositions of 1.62cm occur at the pier's downstream section, and these sediment particles are coming along with the wake flow. Figure 4.4 illustrates the numerical bed topography for a cylindrical pier. The maximum scour depth occurs at the adjacent sides of the cylindrical pier along the Y-axis. Moving further from the center of the pier along the Y-axis will decrease the scour hole depth.

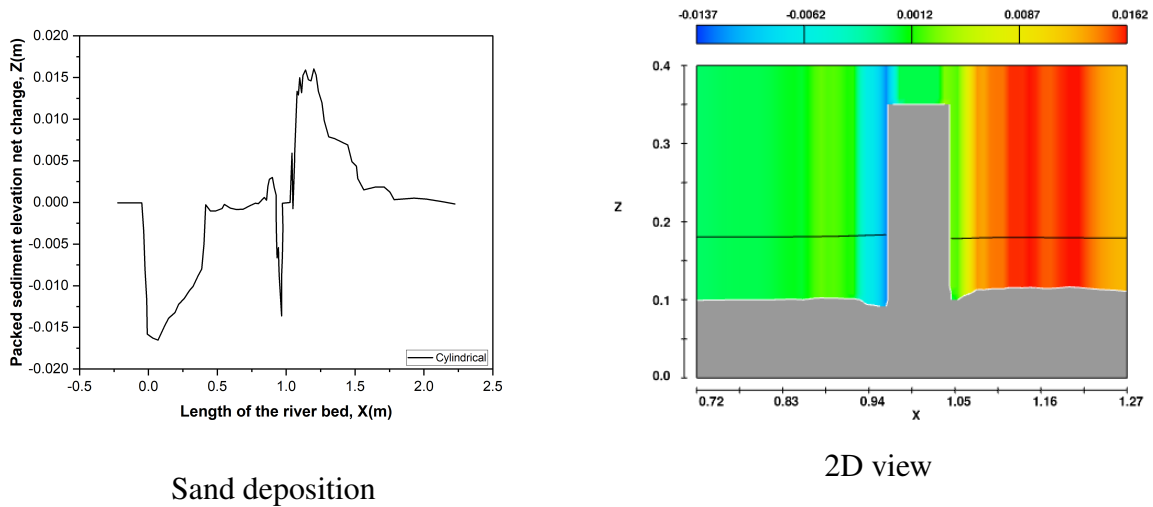


Figure 4.3: Packed sediment elevation net change for Cylindrical pier in ZX plane

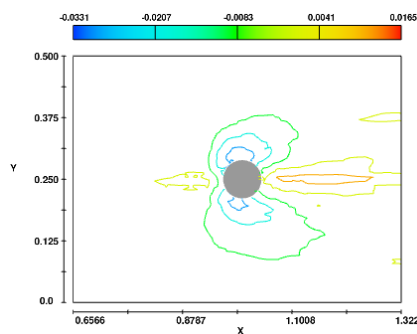


Figure 4.4: Scour depth contour plot of the river bed for Cylindrical pier after scouring

4.1.2 Square Shaped Pier

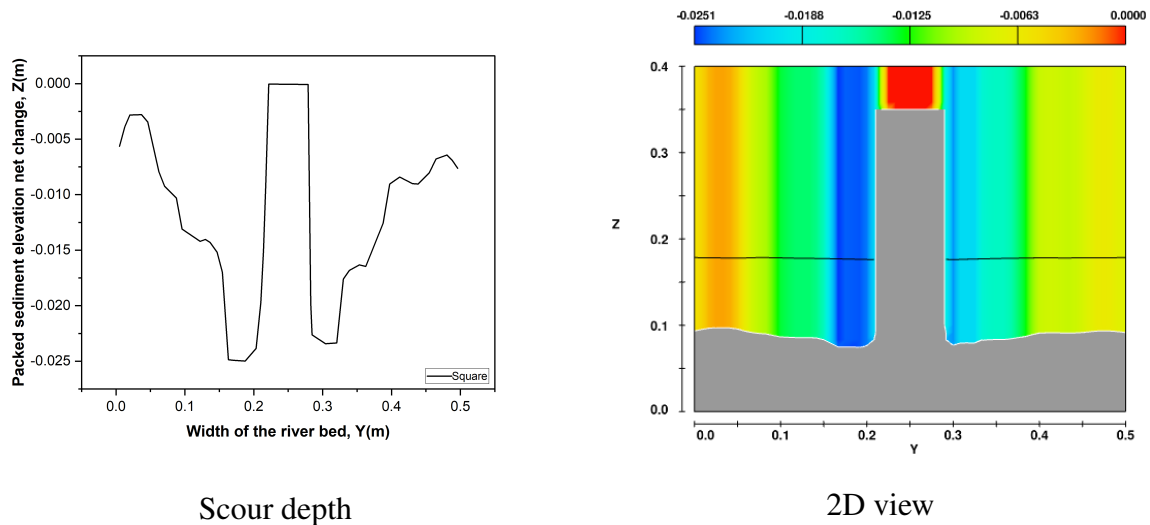


Figure 4.5: Packed sediment elevation net change for Square pier in YZ plane

From Figure 4.5, the maximum scour depth for the square pier is 2.51cm . Figure 4.6 shows the 3D view of the scour depth for the square pier in the presence of isosurface- a fraction of fluid.

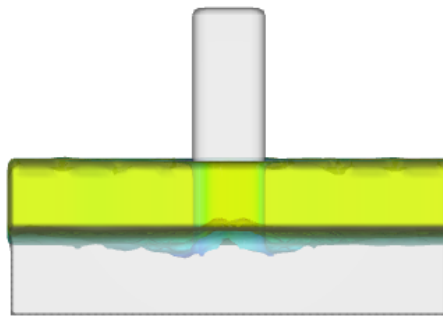
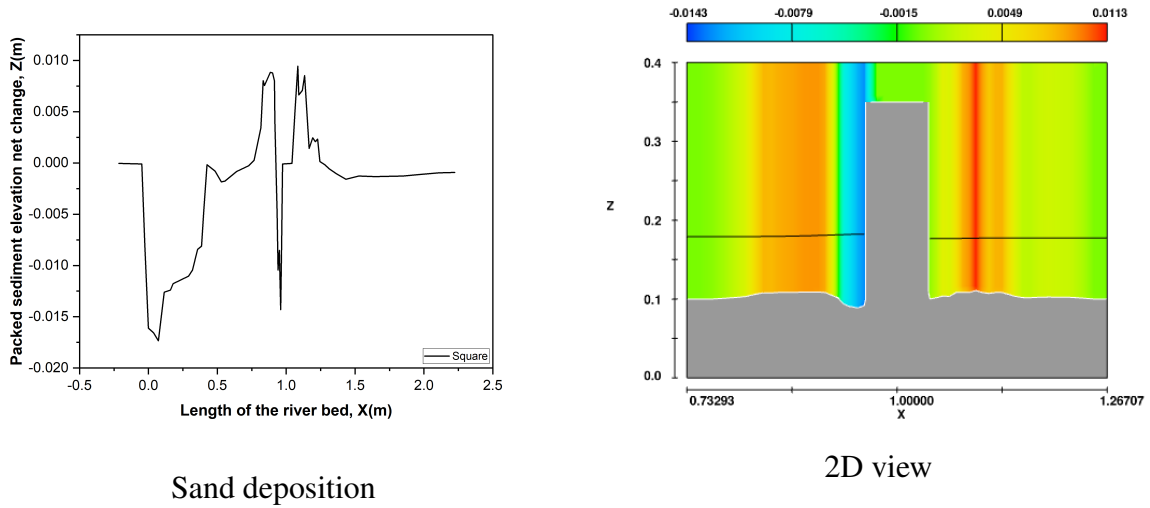


Figure 4.6: 3D Scour depth for the square pier with a fraction of fluid

Figure 4.7 shows entrainment and deposition of sand along the length of the river bed. Because of the high velocity of water at the inlet, a hole of 1.74cm has been created just after the solid block. A small amount of 0.77cm sediment deposits at the upstream part of the pier. On the X-axis, relatively few sediments 1.43cm and 0.15cm have been removed from the pier's upstream and downstream adjacent areas along with the flow. Sediment depositions of 1.13cm occur at the pier's downstream section, and these sediment particles are coming along with the wake flow. Figure 4.8 illustrates the numerical bed topography for a square pier. The maximum scour depth occurs at the upstream front nose of the square pier, which spreads outward from the sides of the square pier along the Y-axis. Moving further from the center of the pier along the Y-axis will decrease the scour hole depth. A depth of 1.43cm hole has been created at the upstream pier section along the X-axis.



Sand deposition
2D view

Figure 4.7: Packed sediment elevation net change for Square pier in ZX plane

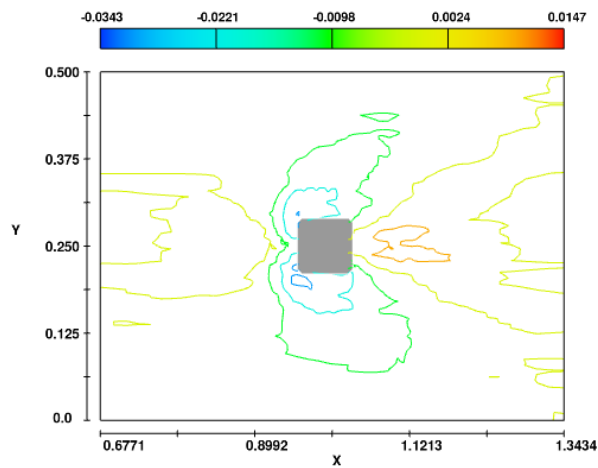


Figure 4.8: Scour depth contour plot of the river bed for Square pier after scouring

4.1.3 Diamond Shaped Pier

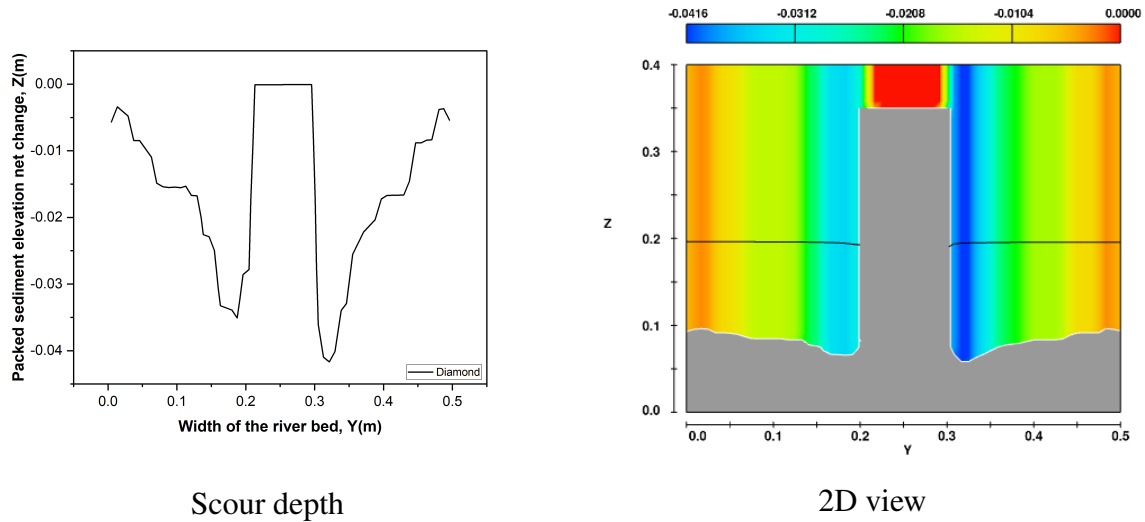


Figure 4.9: Packed sediment elevation net change for Diamond pier in YZ plane

From Figure 4.9, the maximum scour depth for the diamond pier is 4.16cm . Figure 4.10 shows the 3D view of the scour depth after scouring for the diamond pier in the presence of isosurface-a fraction of fluid.

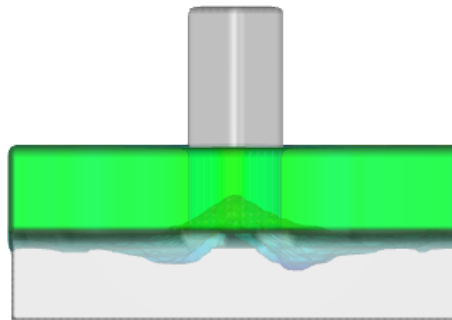


Figure 4.10: 3D Scour depth for the diamond pier with a fraction of fluid

Figure 4.11 shows entrainment and deposition of sand along the length of the river bed. Because of the high velocity of water at the inlet, a hole of 1.67cm has been created just after the solid block. On the X-axis, relatively few sediments 1.57cm have been removed from the pier's upstream adjacent areas along with the flow. Relatively large sediment depositions of 4.54cm occur at the pier's downstream section, and these sediment particles are coming along with the wake flow. Figure 4.12 illustrates the numerical bed topography for a Diamond pier. The maximum scour depth occurs at both of the side noses of the diamond pier, which spreads outward from the sides of the pier along the Y-axis. Moving further from the center of the pier along the Y-axis will decrease the scour hole depth. A depth of 1.57cm hole has been created at the upstream pier section along the X-axis.

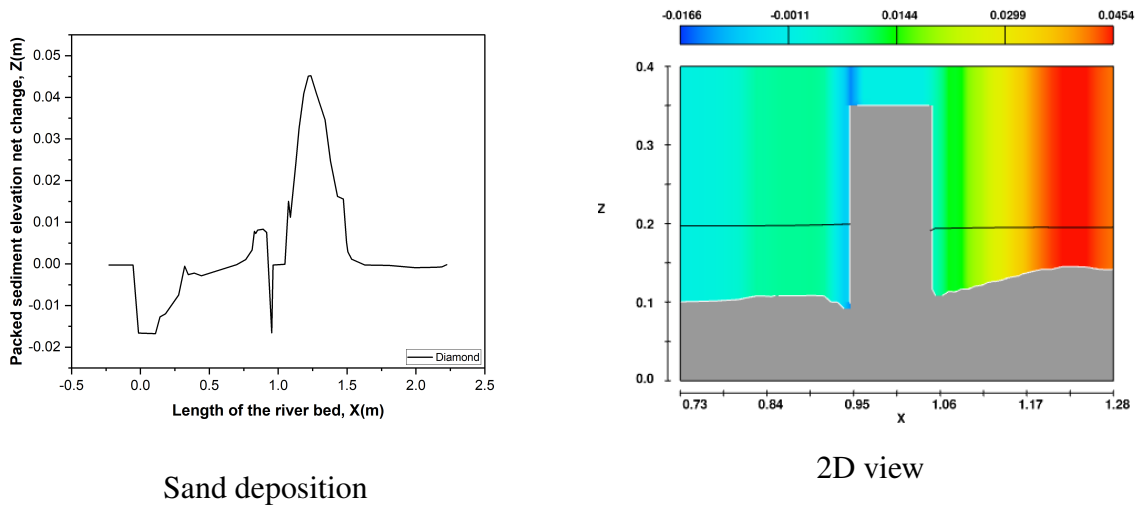


Figure 4.11: Packed sediment elevation net change for Diamond pier in ZX plane

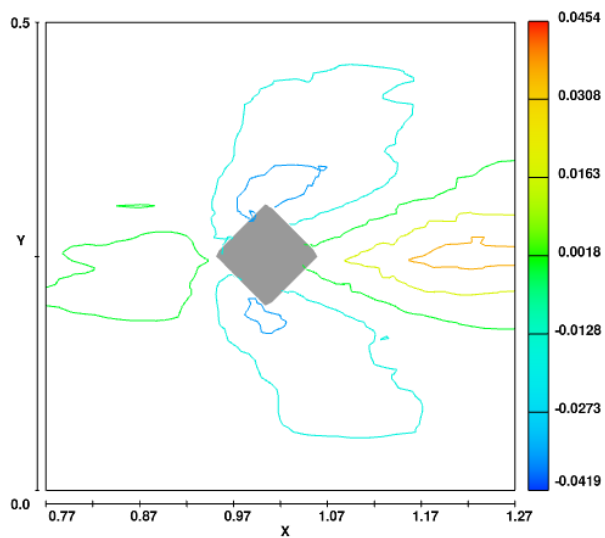


Figure 4.12: Scour depth contour plot of the river bed for Diamond pier after scouring

4.1.4 Hexagonal-Sharp Nose Shaped Pier

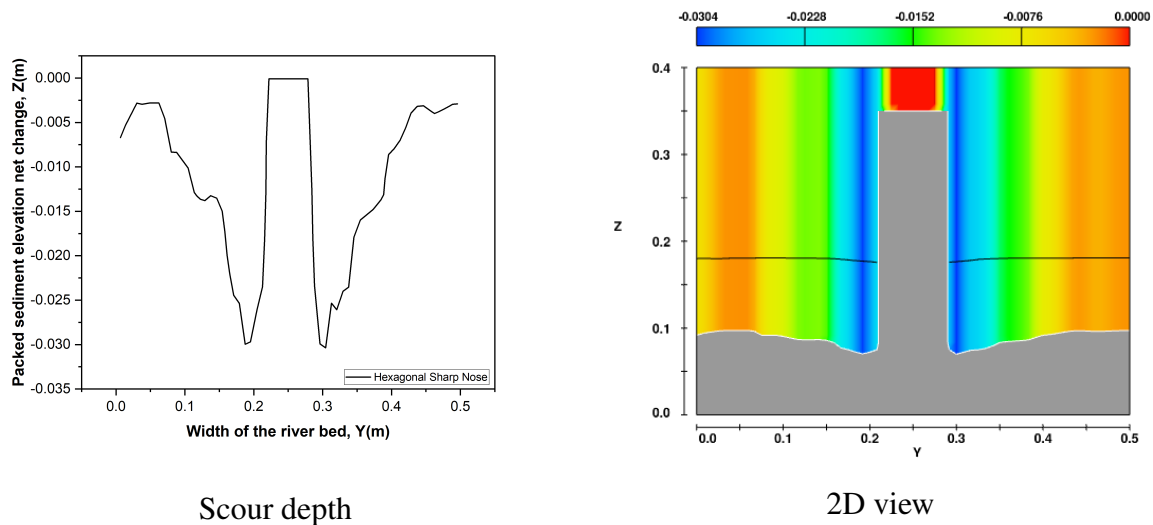


Figure 4.13: Packed sediment elevation net change for Hexagonal-Sharp Nose pier in YZ plane

From Figure 4.13, the maximum scour depth for the Hexagonal-Sharp Nose pier is 3.04cm . Figure 4.14 shows the 3D view of the scour depth after scouring for the Hexagonal-Sharp Nose pier in the presence of the isosurface- a fraction of fluid.

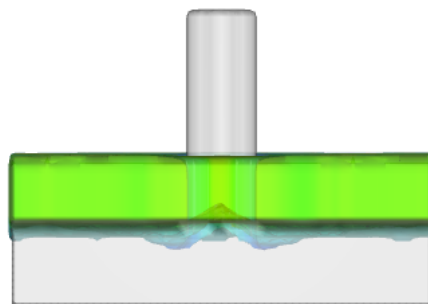


Figure 4.14: 3D Scour depth for the hexagonal-sharp nose pier with a fraction of fluid

Figure 4.15 shows entrainment and deposition of sand along the length of the river bed. Because of the high velocity of water at the inlet, a hole of 2.26cm has been created just after the solid block. On the X-axis, relatively few sediments 0.84cm have been removed from the pier's upstream adjacent areas along with the flow. Sediment depositions of 2.44cm zigzag occur at the pier's downstream section, and these sediment particles are coming along with the wake flow. Figure 4.16 illustrates the numerical bed topography for a hexagonal-sharp nose pier. The maximum scour depth occurs at both of the front side noses of the hexagonal-sharp nose pier, which spreads outward from the sides of the pier along the Y-axis. Moving further from the center of the pier along the Y-axis will decrease the scour hole depth. A depth of 0.84cm hole has been created at the upstream pier section along the X-axis.

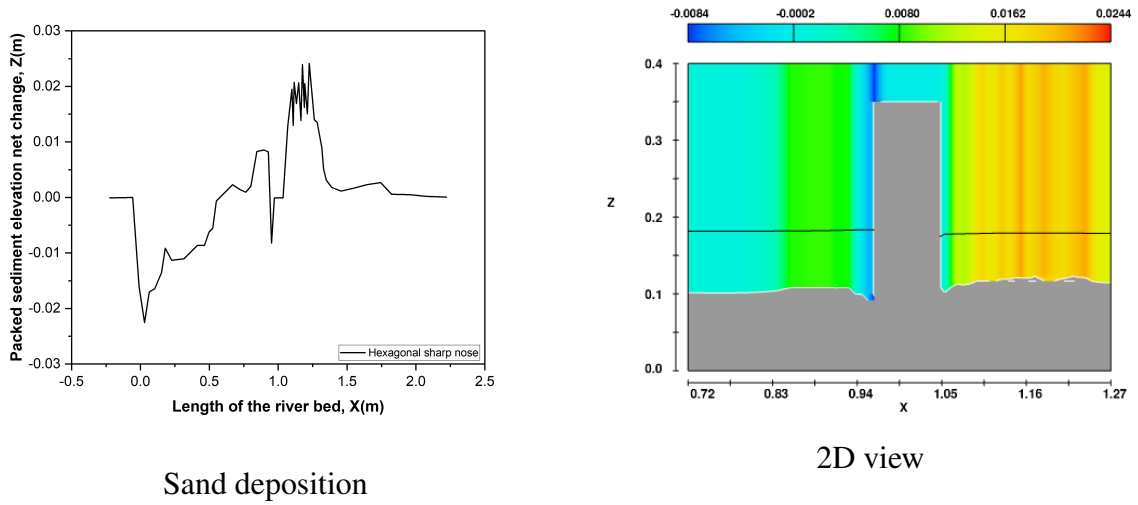


Figure 4.15: Packed sediment elevation net change for Hexagonal- Sharp Nose pier in ZX plane

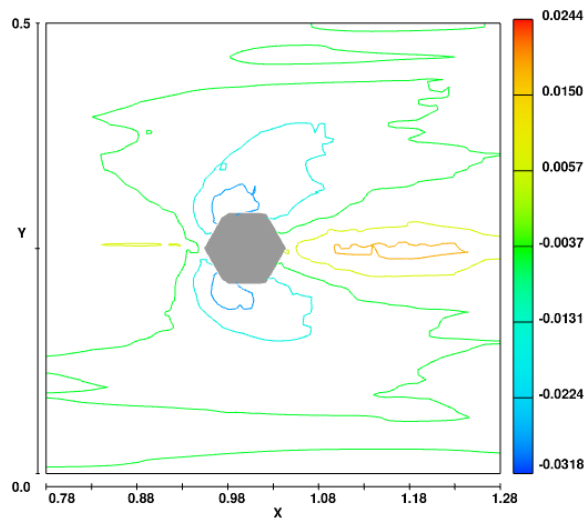


Figure 4.16: Scour depth contour plot of the river bed for Hexagonal- Sharp Nose pier after scouring

4.1.5 Hexagonal-Vertical Nose Shaped Pier

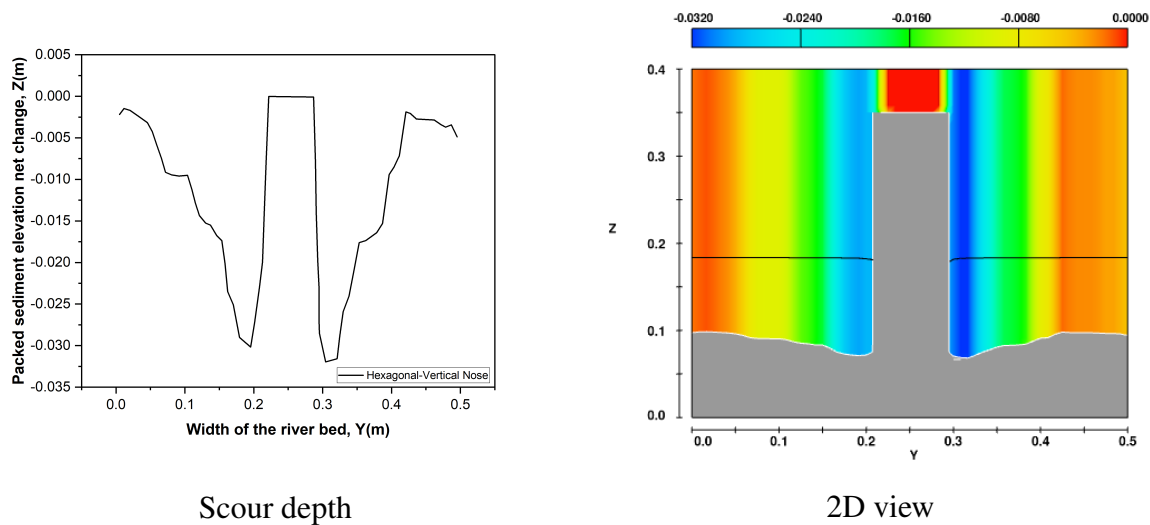


Figure 4.17: Packed sediment elevation net change for Hexagonal- Vertical Nose pier in YZ plane

From Figure 4.17, the maximum scour depth for the Hexagonal- Vertical Nose pier is 3.2cm . Figure 4.18 shows the 3D view of the scour depth after scouring for the Hexagonal- Vertical Nose pier with the isosurface- a fraction of fluid.

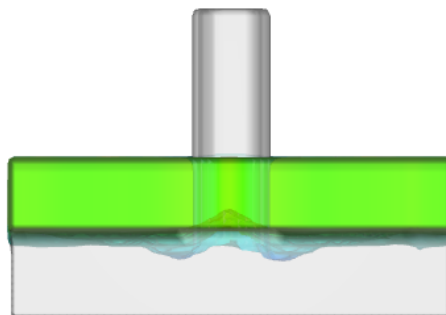


Figure 4.18: 3D Scour depth for the hexagonal-vertical nose pier with a fraction of fluid

Figure 4.19 shows entrainment and deposition of sand along the length of the river bed. Because of the high velocity of water at the inlet, a hole of 1.84cm has been created just after the solid block. On the X-axis, relatively few sediments 1.27cm have been removed from the pier's upstream adjacent areas along with the flow. Sediment depositions of 2.45cm occur at the pier's downstream section, and these sediment particles are coming along with the wake flow. Figure 4.20 illustrates the numerical bed topography for a hexagonal-vertical nose pier. The maximum scour depth occurs at both of the side noses of the hexagonal-vertical nose pier, which spreads outward from the sides of the pier along the Y-axis. Moving further from the center of the pier along the Y-axis will decrease the scour hole depth. A depth of 1.27cm hole has been created at the upstream pier section along the X-axis.

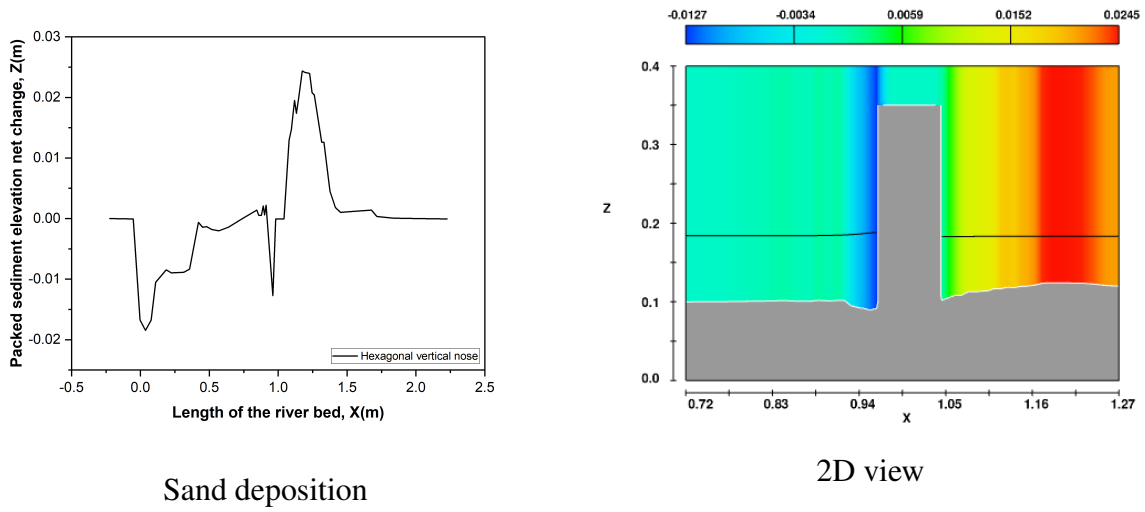


Figure 4.19: Packed sediment elevation net change for Hexagonal- Vertical Nose pier in ZX plane

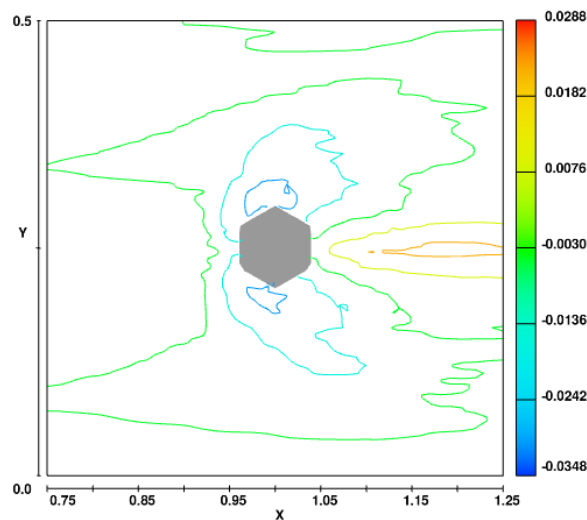


Figure 4.20: Scour depth contour plot of the river bed for Hexagonal- Vertical Nose pier after scouring

4.1.6 Airfoil Shaped Pier

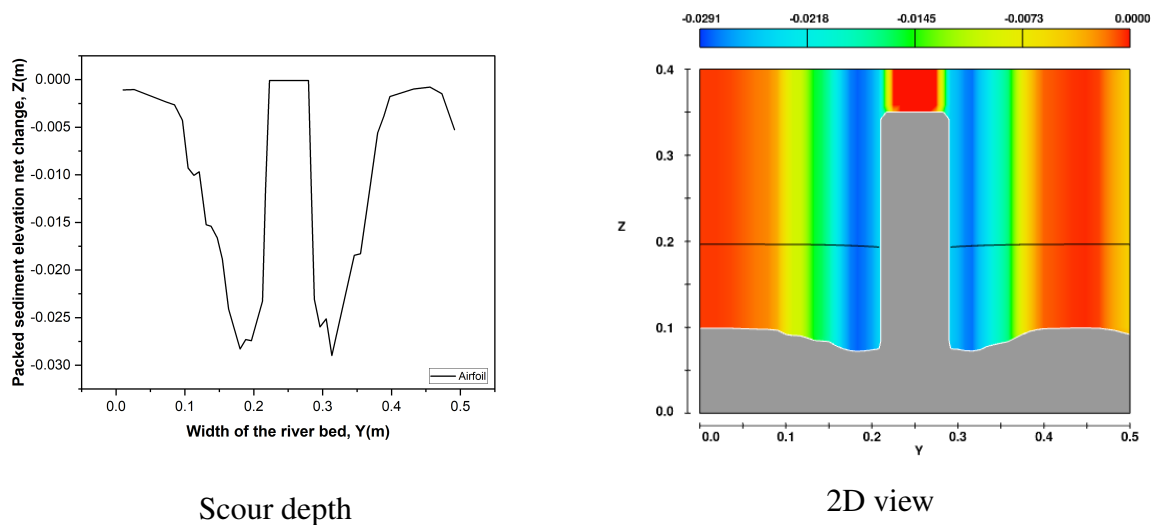


Figure 4.21: Packed sediment elevation net change for Airfoil pier in YZ plane

From Figure 4.21, the maximum scour depth for the airfoil pier is 2.91 cm . Figure 4.22 shows the 3D view of the scour depth after scouring for the airfoil pier contains an isosurface- a fraction of fluid.

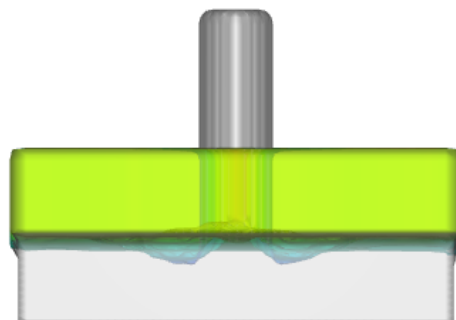
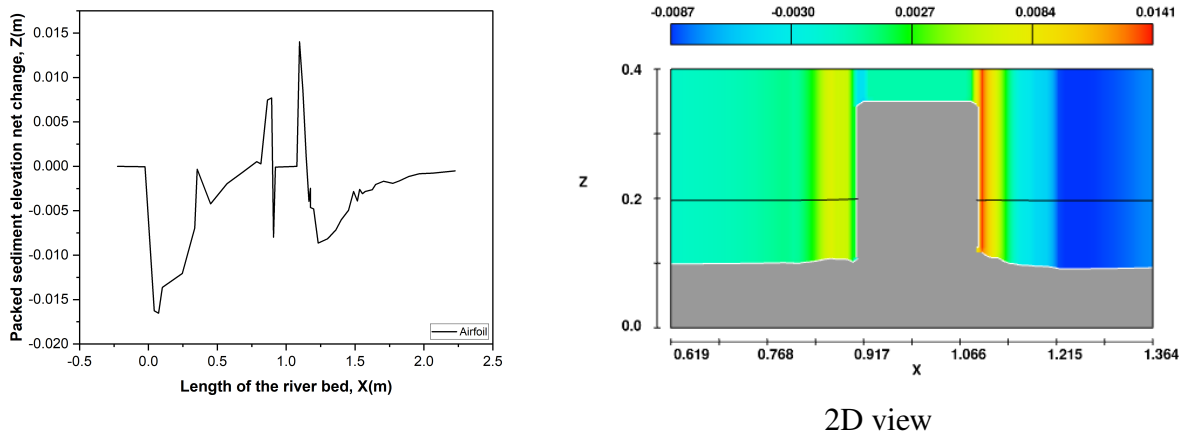


Figure 4.22: 3D Scour depth for the airfoil pier with a fraction of fluid

Figure 4.23 shows entrainment and deposition of sand along the length of the river bed. Because of the high velocity of water at the inlet, a hole of 1.66 cm has been created just after the solid block. On the X-axis, relatively few sediments have been removed from the pier's upstream and downstream adjacent areas along with the flow. A small amount of 0.64 cm sediment deposits at the upstream end of the pier. Sediment depositions of 1.41 cm occur at the pier's downstream section, and these sediment particles are coming along with the wake flow. A depth of 0.87 cm hole has been created at the downstream pier section along the X-axis. Figure 4.24 illustrates the numerical bed topography for a hexagonal-vertical nose pier. The maximum scour depth occurs at both sides of the airfoil pier, which spreads outward from the sides of the pier along the Y-axis. Moving further from the center of the pier along the Y-axis will decrease the scour hole depth.



Sand deposition

Figure 4.23: Packed sediment elevation net change for Airfoil pier in ZX plane

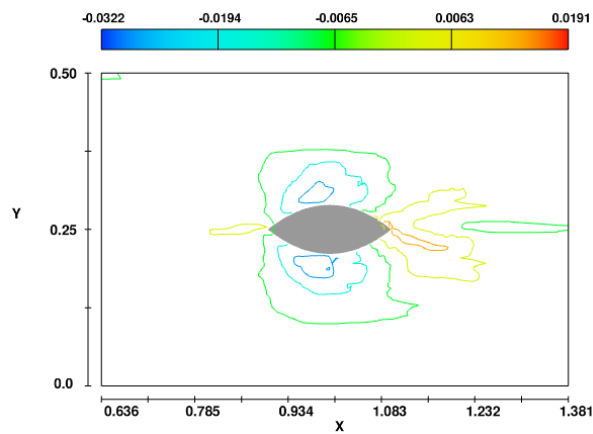


Figure 4.24: Scour depth contour plot of the river bed for Airfoil pier after scouring

4.1.7 Upstream Facing Airfoil Shaped Pier

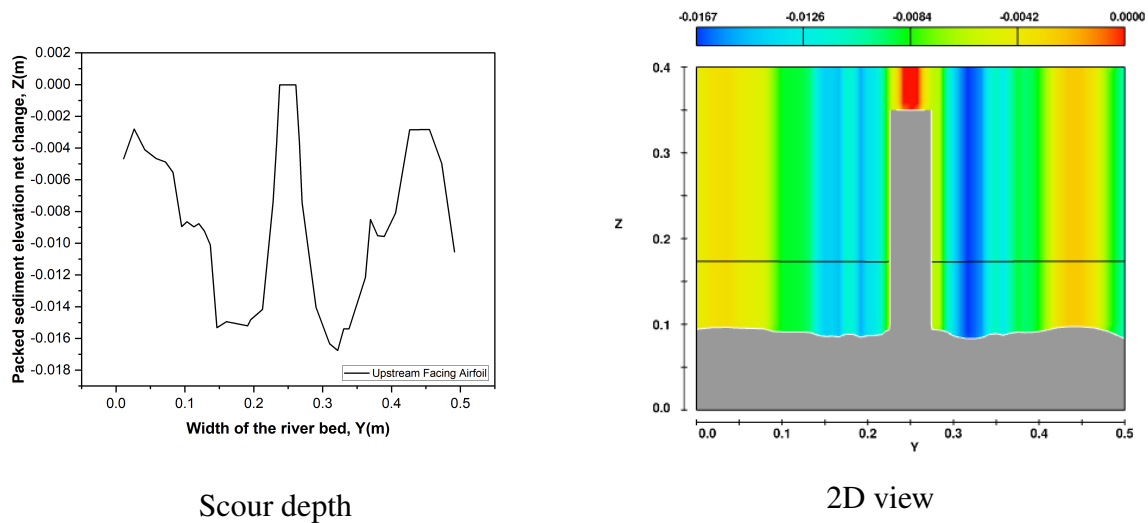


Figure 4.25: Packed sediment elevation net change for Upstream Facing Airfoil pier in YZ plane

From Figure 4.25, the maximum scour depth for the upstream facing pier is 1.67 cm . Figure 4.26 shows the 3D view of the scour depth after scouring for the upstream facing airfoil pier with an isosurface- a fraction of fluid.

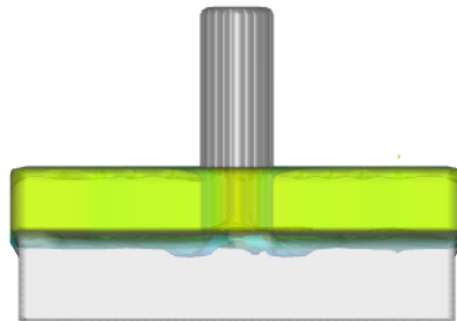


Figure 4.26: 3D Scour depth for the upstream facing airfoil pier with a fraction of fluid

Figure 4.27 shows entrainment and deposition of sand along the length of the river bed. Because of the high velocity of water at the inlet, a hole of 1.68 cm has been created just after the solid block. A small amount of 0.95 cm sediment deposits at the upstream end of the pier. On the X-axis, relatively few sediments 1.61 cm have been removed from the pier's upstream adjacent areas along with the flow. Sediment depositions of 0.95 cm occur at the pier's downstream adjacent section, and these sediment particles are coming along with the wake flow. Figure 4.28 illustrates the numerical bed topography for a hexagonal-vertical nose pier. The maximum scour depth occurs at the front merge point of the half circle and straight line of the upstream facing airfoil pier, which spreads outward from the sides of the pier along the Y-axis. Moving further from the center of the pier along the Y-axis will decrease the scour hole depth. A depth of

1.61cm and 0.31cm hole has been created at the upstream and downstream pier sections along the X-axis, respectively.

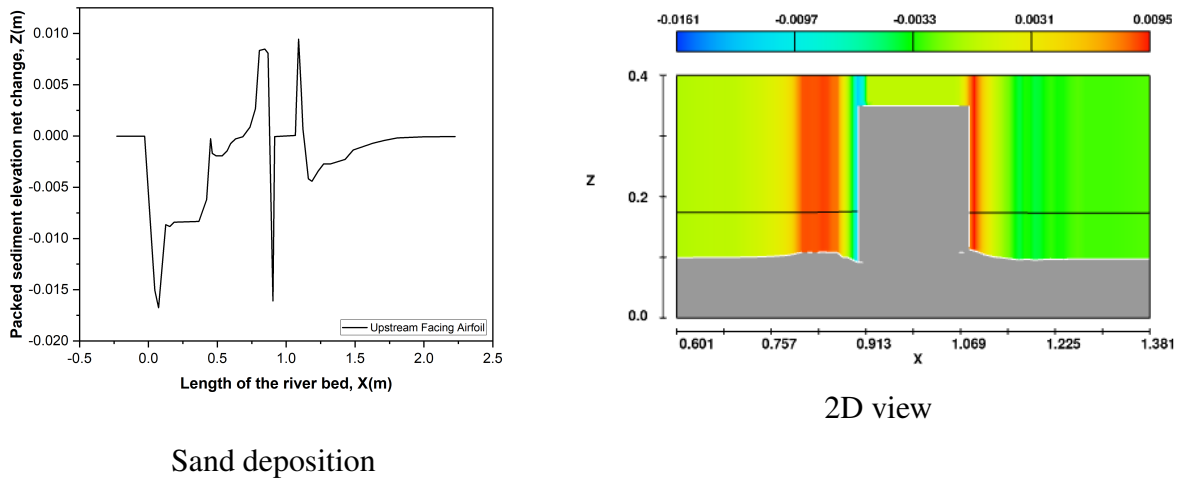


Figure 4.27: Packed sediment elevation net change for Upstream Facing Airfoil pier in ZX plane

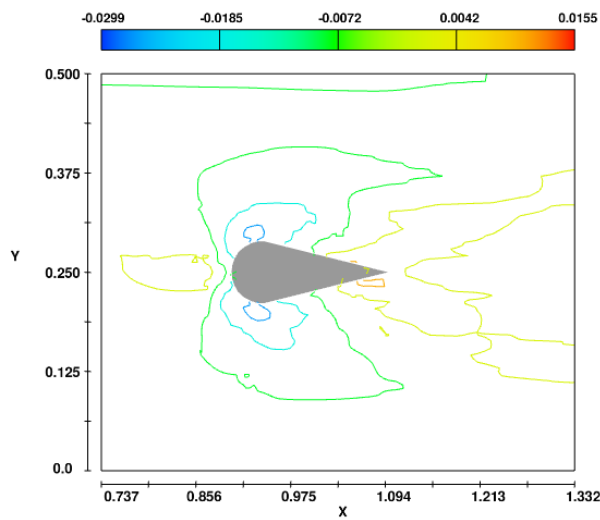


Figure 4.28: Scour depth contour plot of the river bed for Upstream Facing Airfoil pier after scouring

4.1.8 Downstream Facing Airfoil Shaped Pier

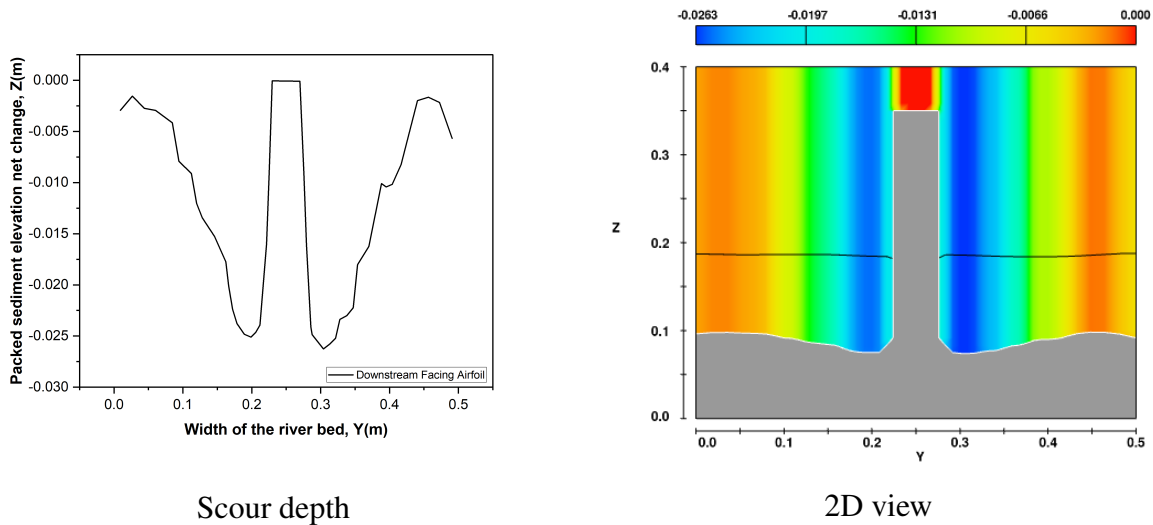


Figure 4.29: Packed sediment elevation net change for Downstream Facing Airfoil pier in YZ plane

From Figure 4.29, the maximum scour depth for the downstream facing pier is 2.63cm . Figure 4.30 shows the 3D view of the scour depth after scouring for the downstream facing airfoil pier in the presence of the isosurface- a fraction of fluid.

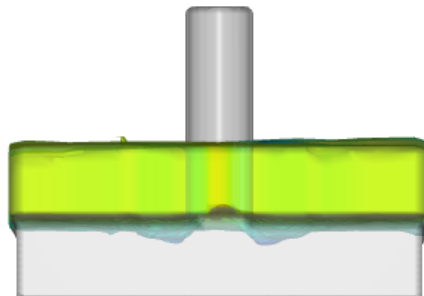


Figure 4.30: 3D Scour depth for the downstream facing airfoil pier with a fraction of fluid

Figure 4.31 shows entrainment and deposition of sand along the length of the river bed. Because of the high velocity of water at the inlet, a hole of 1.62cm has been created just after the solid block. A small amount of 0.56cm sediment deposits at the upstream end of the pier. On the X-axis, relatively few sediments have been removed from the pier's upstream and downstream adjacent areas along with the flow. Sediment depositions of 1.85cm occur at the pier's downstream section, and these sediment particles are coming along with the wake flow. Figure 4.32 illustrates the numerical bed topography for a hexagonal-vertical nose pier. The maximum scour depth occurs at the end merge point of the half circle and straight line of the downstream facing airfoil pier, which spreads outward from the sides of the pier along the Y-axis. Moving further from the center of the pier along the Y-axis will decrease the scour hole depth. A depth of 0.74cm hole has been created at the downstream pier section along the X-axis.

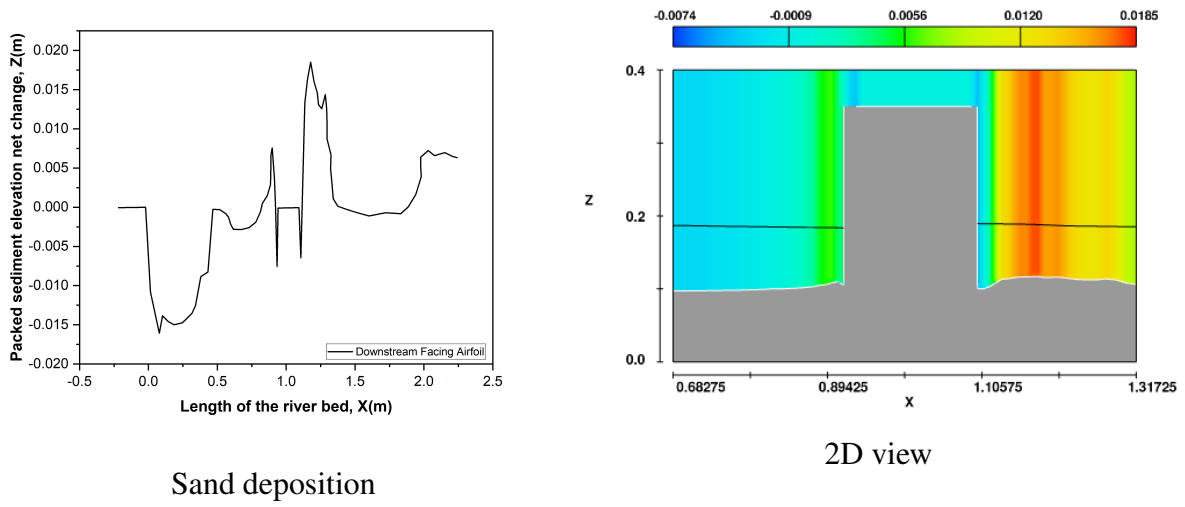


Figure 4.31: Packed sediment elevation net change for Downstream Facing Airfoil pier in ZX plane

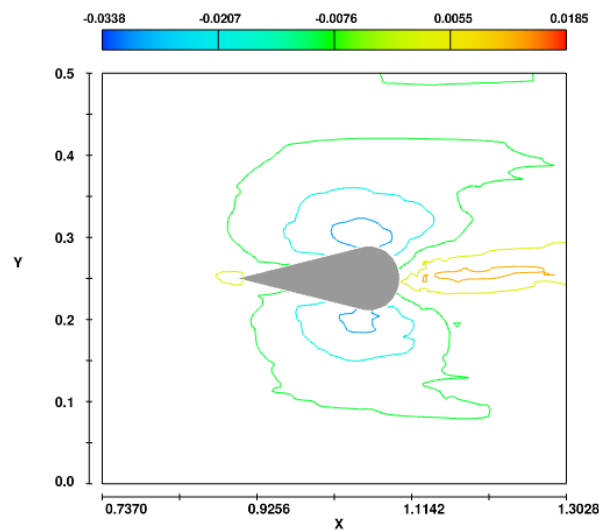


Figure 4.32: Scour depth contour plot of the river bed for Downstream Facing Airfoil pier after scouring

4.1.9 Oblong Shaped Pier

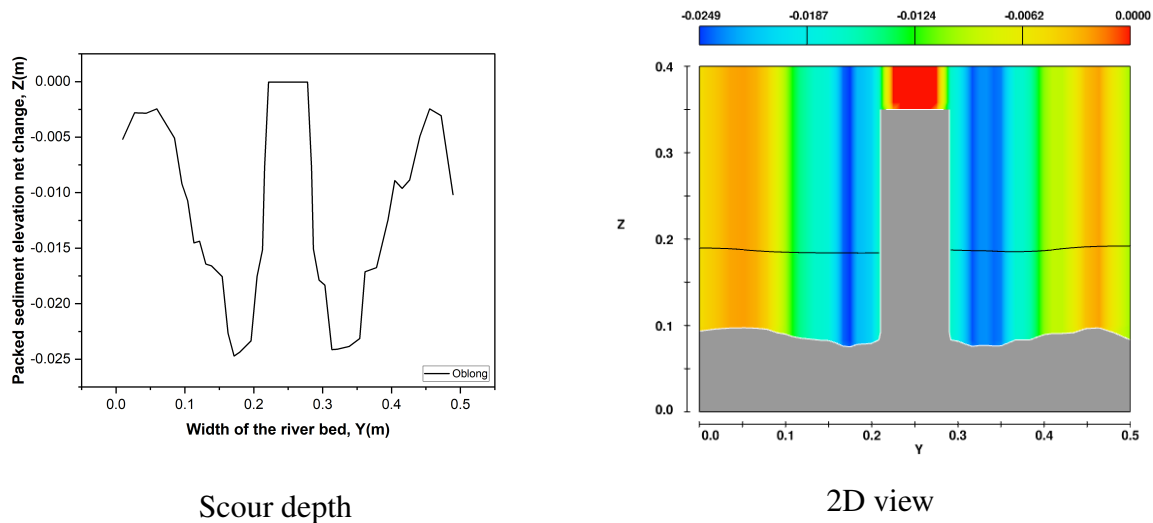


Figure 4.33: Packed sediment elevation net change for Oblong pier in YZ plane

From Figure 4.33, the maximum scour depth for the oblong pier is 2.49cm . Figure 4.34 shows the 3D view of the scour depth after scouring for the oblong pier where the isosurface- a fraction of fluid is present.

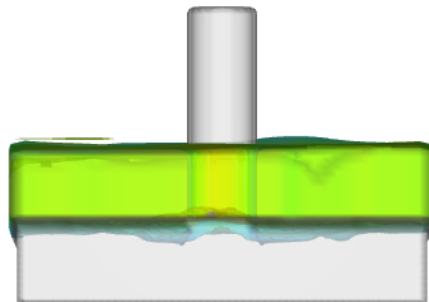


Figure 4.34: 3D Scour depth for the oblong pier with a fraction of fluid

Figure 4.35 shows entrainment and deposition of sand along the length of the river bed. Because of the high velocity of water at the inlet, a hole of 1.54cm has been created just after the solid block. On the X-axis, relatively few sediments have been removed from the pier's upstream and downstream adjacent areas. A small amount of 0.81cm sediment deposits at the upstream end of the pier and 0.93cm sediment transfers from the upstream end of the pier along with the flow. Sediment depositions of 1.59cm occur at the pier's downstream section, and these sediment particles are coming along with the wake flow. Figure 4.36 illustrates the numerical bed topography for a hexagonal-vertical nose pier. The maximum scour depth occurs at the front merge point of the half circle and straight line of the oblong pier, which spreads outward from the sides of the pier along the Y-axis. Moving further from the center of the pier along

the Y-axis will decrease the scour hole depth. A depth of 0.93cm hole has been created at the upstream pier section along the X-axis.

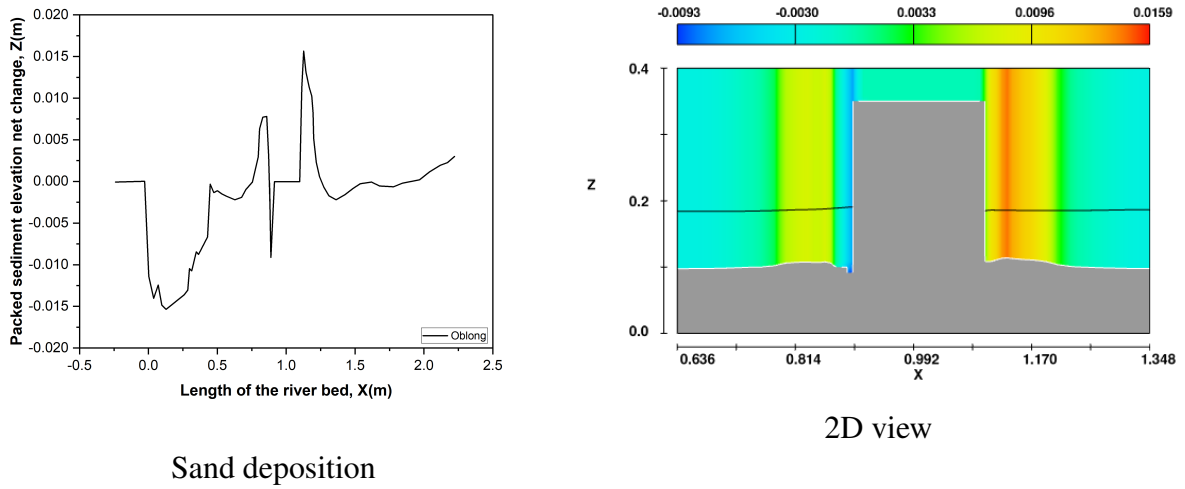


Figure 4.35: Packed sediment elevation net change for Oblong pier in ZX plane

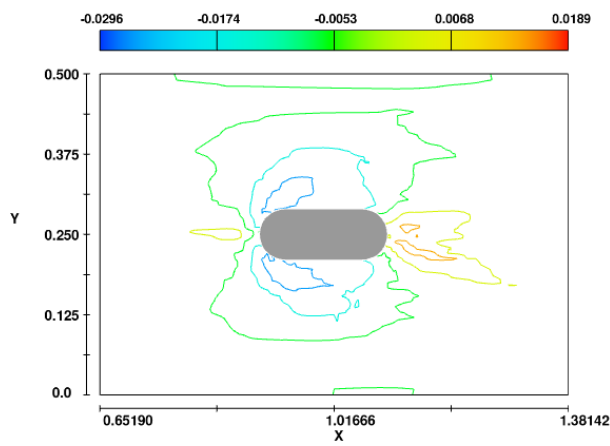


Figure 4.36: Scour depth contour plot of the river bed for Oblong pier after scouring

4.1.10 Rectangle Shaped Pier

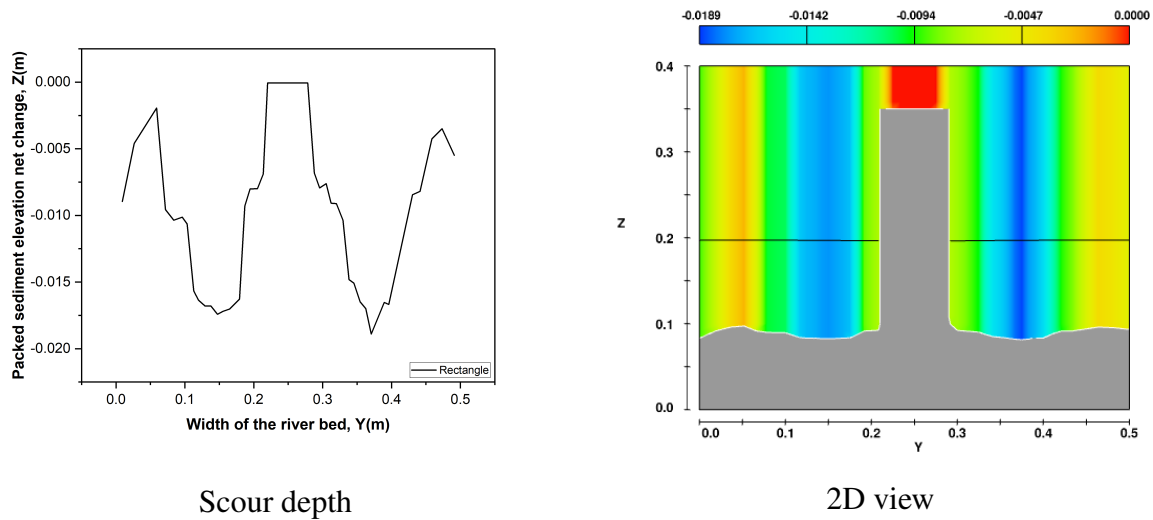


Figure 4.37: Packed sediment elevation net change for Rectangle pier in YZ plane

From Figure 4.37, the maximum scour depth for the rectangle pier is 1.89cm . Sediments have not been removed fully from the pier's adjacent areas along Y-axis. The scour depth has been created a bit far away from the sides of the pier along the Y-axis. Figure 4.38 shows the 3D view of the scour depth after scouring for the rectangle pier with the presence of the isosurface-a fraction of fluid.

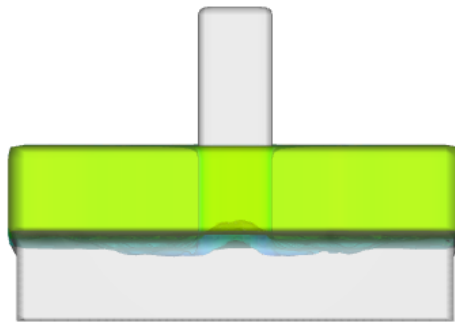


Figure 4.38: 3D Scour depth for the rectangle pier with a fraction of fluid

Figure 4.39 shows entrainment and deposition of sand along the length of the river bed. Because of the high velocity of water at the inlet, a hole of 1.67cm has been created just after the solid block. On the X-axis, relatively few sediments have been removed from the pier's upstream and downstream adjacent areas. A small amount of 1cm sediment deposits at the upstream end of the pier and 1.67cm sediment transfers from the upstream end of the pier along with the flow. Sediment depositions of 1.71cm occur at the pier's downstream section, and these sediment particles are coming along with the wake flow. Figure 4.40 illustrates the numerical bed topography for a hexagonal-vertical nose pier. The maximum scour depth occurs at both

of the front side noses of the rectangle pier, which spreads outward from the sides of the pier along the Y-axis. Moving further from the center of the pier along the Y-axis will decrease the scour hole depth. A depth of 1.67cm hole has been created at the upstream pier section along the X-axis.

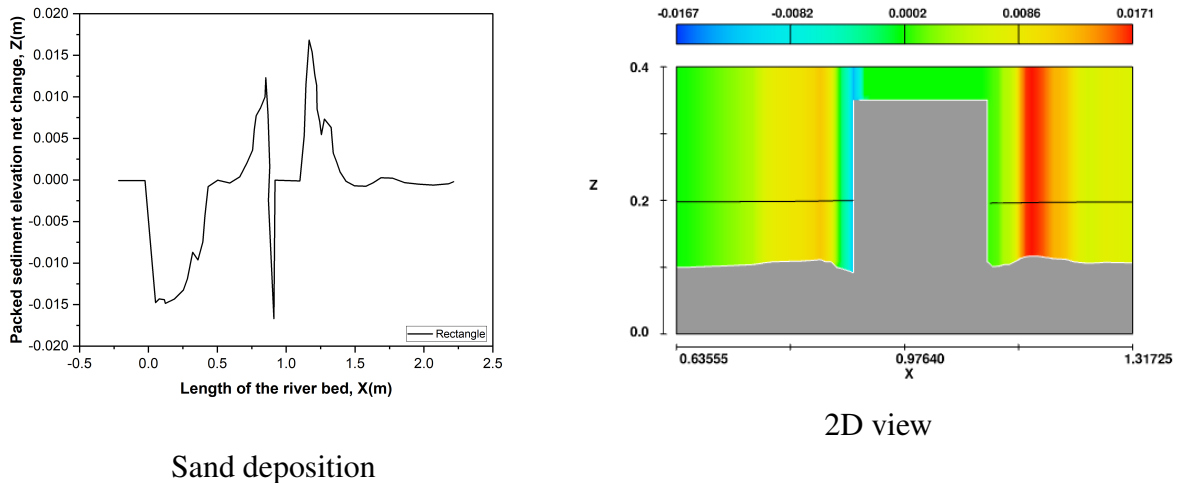


Figure 4.39: Packed sediment elevation net change for Rectangle pier in ZX plane

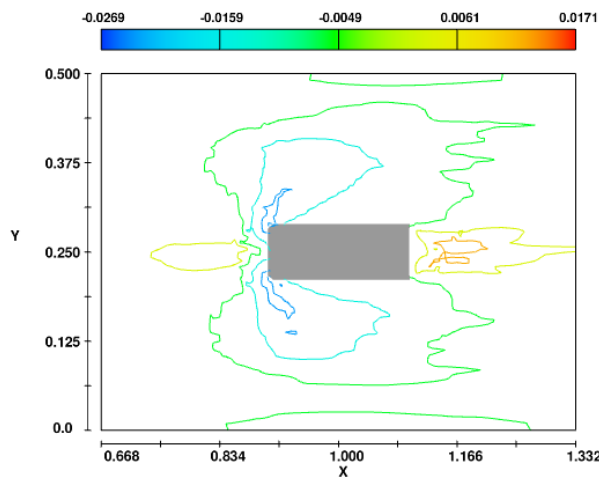


Figure 4.40: Scour depth contour plot of the river bed for Rectangle pier after scouring

4.1.11 Comparison Of The Scour Depths And Sediment Deposition

From Table 4.1, the diamond pier has the highest scour depth and sand deposition. Therefore, using diamond piers for bridge construction will probably lead to the bridge’s collapse. The square pier has the least value of scour depth and sand deposition and is therefore more efficient. The scour depths and sediment deposition of piers with cylindrical, square, diamond, and hexagonal shapes have been compared in Figure 4.41.

Table 4.1: Scour depth and sediment deposition

Pier Geometry	Max. Scour Depth (cm)	Max. Sand Deposition (cm)
Cylindrical	3.18	1.62
Square	2.51	1.13
Diamond	4.16	4.54
Hexagonal-sharp nose	3.04	2.44
Hexagonal-vertical nose	3.20	2.45

The scour depth of the square pier is 21%, 40%, 17.5%, 21.5% less compared to the cylindrical, diamond, hexagonal-sharp nose, hexagonal-vertical nose piers, respectively. The scour depth of the diamond pier is almost double of the square pier's scour depth. The depths of scour hole of the cylindrical and hexagonal-vertical nose pier are nearly the same. From Table 4.1, the second efficient pier with the least scour depth is hexagonal-sharp nose pier.

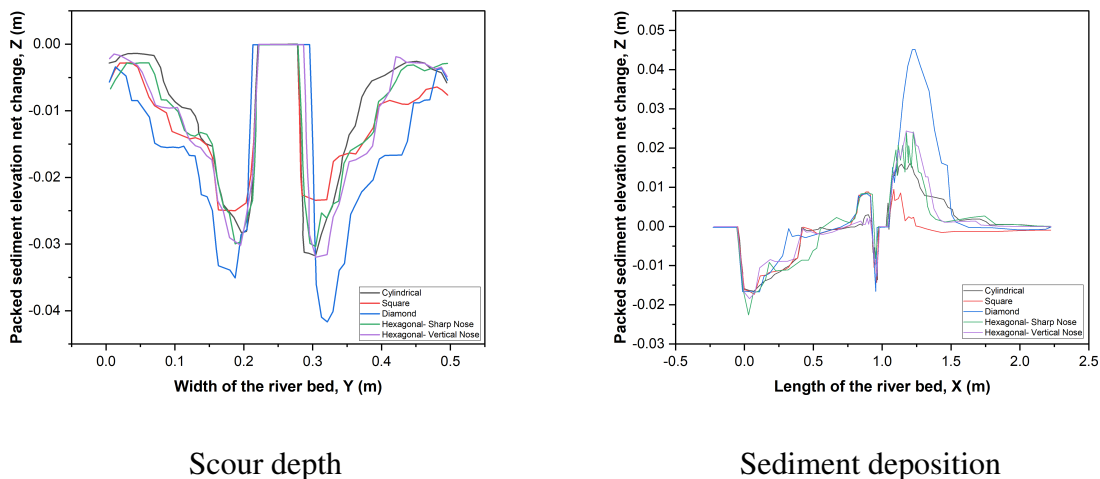


Figure 4.41: Comparison among the scour depth and sediment deposition of cylindrical, square, diamond, and hexagonal piers

From Table 4.1, the sediment deposition of the square pier is 30%, 75%, 53.6%, and 53.8% less compared to the cylindrical, diamond, hexagonal-sharp nose, hexagonal-vertical nose piers, respectively. The sediment depositions for the two hexagonal piers have almost the same value. Due to the diamond pier's sharp edge geometry, there is considerable sand deposition at its downstream section. There are no scour holes at the downstream end of the cylindrical, square, diamond, and hexagonal piers.

From Table 4.2, the airfoil pier has the highest scour depth because of its streamlined shape. Therefore, using airfoil piers during bridge construction will likely cause the bridge to collapse. The upstream facing airfoil and rectangle piers have the least scour depth value and are therefore more reliable. The scour depths and sediment deposition of piers with airfoil, oblong, and rectangle shapes have been compared in Figure 4.42.

Table 4.2: Scour depth and sediment deposition

Pier Geometry	Max. Scour Depth (cm)	Max. Sand Deposition (cm)
Airfoil	2.91	1.41
Upstream facing airfoil	1.67	0.95
Downstream facing airfoil	2.63	1.85
Oblong	2.49	1.59
Rectangle	1.89	1.71

The scour depth of the upstream facing airfoil pier is 42.6%, 36.5%, 32.9%, 11.6% less compared to the airfoil, downstream facing airfoil, oblong, and rectangle piers, respectively. The scour depth of the rectangle pier is 35%, 28.1%, 24% less compared to the airfoil, downstream facing airfoil, and oblong piers, respectively. The scour hole depth of the rectangle pier is 13% higher than the upstream facing airfoil pier's scour depth. The scour depth of the airfoil pier is 74.2% and 53.9% higher than the upstream facing airfoil and rectangle piers, respectively. The depths of scour hole of the downstream facing airfoil and oblong pier are almost the same. From Table 4.2, the rectangle pier is the second most efficient pier with the least scour depth.

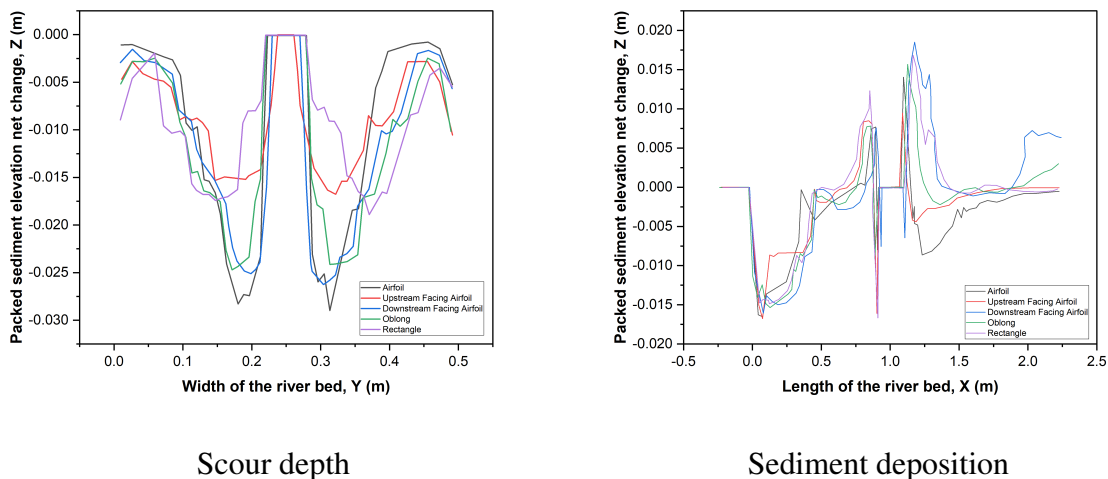


Figure 4.42: Comparison among the scour depth and sediment deposition of airfoil, oblong, and rectangle piers

From Table 4.2, the sediment deposition of the upstream facing airfoil pier is 32.6%, 48.6%, 40.25%, and 44.44% less compared to the airfoil, downstream facing airfoil, oblong, and rectangle piers, respectively. The sediment depositions of the downstream facing airfoil and the rectangle piers have almost the same value. Due to the streamlined geometry of the airfoil pier, it has a scour hole of 0.87cm depth at its downstream section instead of significant sediment deposition. There is also a small scour hole of 0.31cm depth at the downstream end of the upstream facing airfoil pier. The amount of sediment deposition at the downstream portion of the airfoil, oblong, rectangular piers is less than the diamond and hexagonal piers.

Table 4.3: Scour depths around the pier in cm unit

Pier Geometry	Left SD	Right SD	Front SD	Rear SD
Cylindrical	2.785	3.18	1.37	0.12
Square	2.51	2.195	1.43	0.15
Diamond	3.50	4.16	1.57	0.11
Hexagonal-sharp nose	3.04	3.04	0.84	0.02
Hexagonal-vertical nose	3	3.20	1.27	0.20
Airfoil	2.91	2.91	0.70	0.87
Upstream facing airfoil	1.60	1.67	1.61	0.33
Downstream facing airfoil	2.50	2.63	0.74	0.60
Oblong	2.49	2.49	0.93	0
Rectangle	1.75	1.89	1.67	0.02

Scour depths in the left, right, front, and rear section of the piers are given in table 4.3.

4.1.12 Scour Depth In 3D View

After completing the simulation for all the ten different shaped piers, the 3D scouring geometry around the piers has been achieved and shown in Figure 4.43 and Figure 4.44. From Figure 4.43, the diamond-shaped pier has a large amount of sediment deposition at the back end of the pier, whereas the square-shaped pier has the least value of sediment deposition. The amount of sediment deposition is less for the piers in Figure 4.44 for their elongated and streamlined shape.

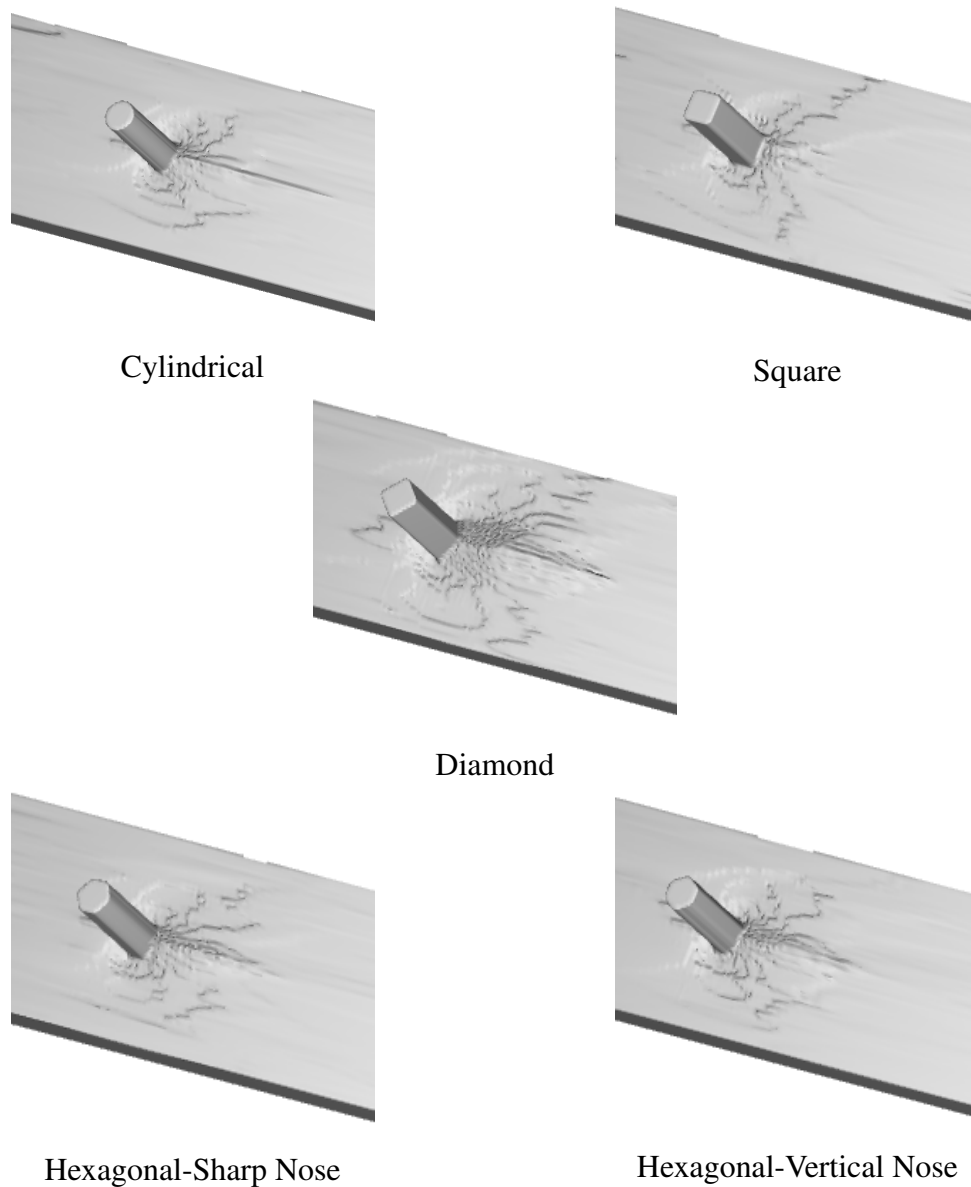


Figure 4.43: River bed in 3D after scouring for cylindrical, square, diamond, hexagonal pier

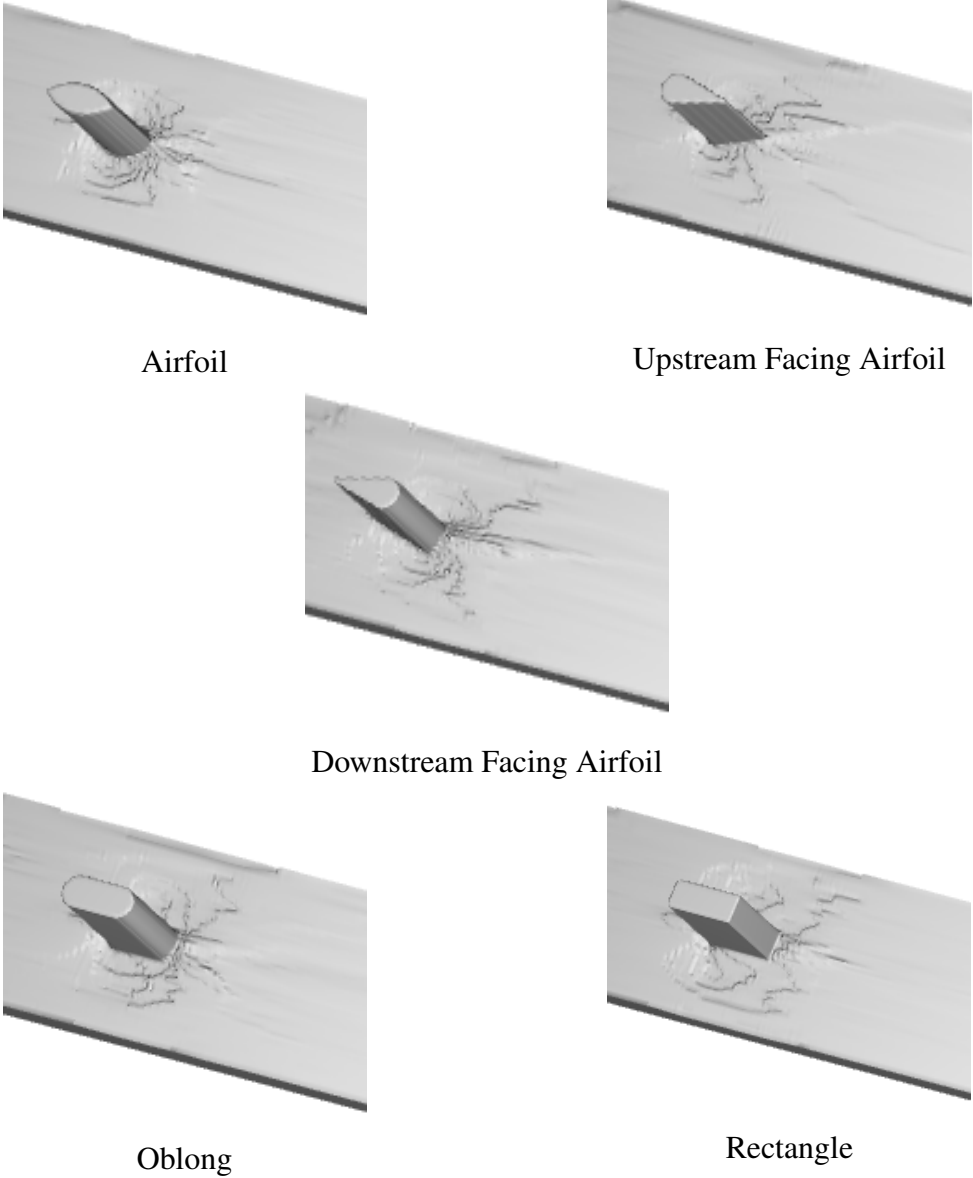


Figure 4.44: River bed in 3D after scouring for airfoil, oblong, rectangle pier

4.2 Velocity and Pressure Distribution

Observing the distribution of velocity and pressure along the length of the river bed will reveal the primary cause of scouring. The flume bed does not have a continuous velocity. Instead, the flow velocity varies at the upstream and downstream zones and near the structural piers. At the inlet, the flow velocity is high, and for the cylindrical pier, it is 0.305m s^{-1} . The flow velocity at the front of the pier and fluid interface is almost zero, and this point is known as the stagnation point in Figure 4.45. A decrease in velocity leads to an increase in pressure. At the stagnation point, the pressure gradient has its highest value. The water velocity also changes along the Z-direction, from which pressure gradient can be obtained. Pressure is highest at the bottom and gradually decreases as it moves to the top surface. For the cylindrical pier in Figure 4.45, the pressure gradient at the front section of the pier is 850Pa . The pressure gradient along the Z-direction influences the scouring mechanism and transfers sediment particles from the front of the pier to the downstream. Scouring is higher at the front section of the pier because of the high-pressure gradient. At the rear section of the pier, the water velocity is low, the pressure gradient is 770Pa , and the flow is unsteady. This zone in Figure 4.45 is called a wake region, where eddies and wake vortices have been formed. This will form a scouring area behind the pier, and in this region, the scour hole depth is insignificant because of low water velocity. Sediments will come along the wake flow and deposits at the rear section of the pier. After the wake region, the flow begins to accelerate again. However, no further scouring is observed because no abutment or pillar is blocking the flow, creating an obstacle and resulting in local scouring. The velocity and pressure distribution process are the same for the rest of the piers instead of the numerical values.

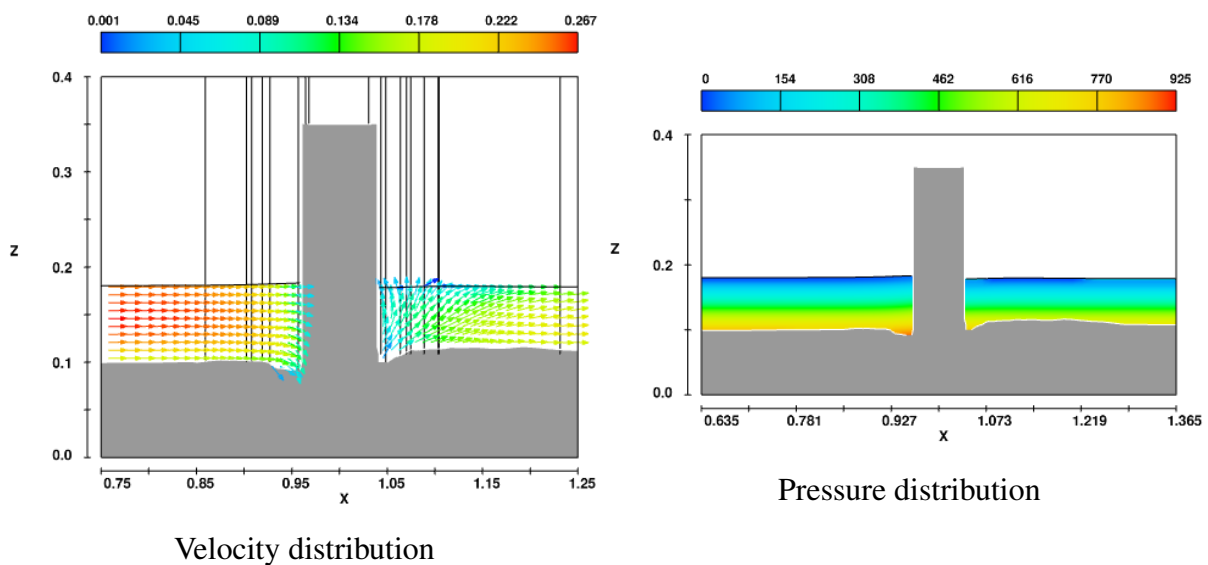


Figure 4.45: Velocity and pressure distribution for cylindrical pier in ZX plane

For square pier in Figure 4.46, pressure gradients at the front and rear section of the pier are $920Pa$ and $650Pa$, respectively. According to the velocity distribution graph, the wake region of the square pier is located a bit further from the pier compared to the cylindrical pier. The reason for this is that the cylindrical pier has a more streamlined shape than the square pier. The edges of the square pier are not streamlined, and these edges resist creating a streamlined flow.

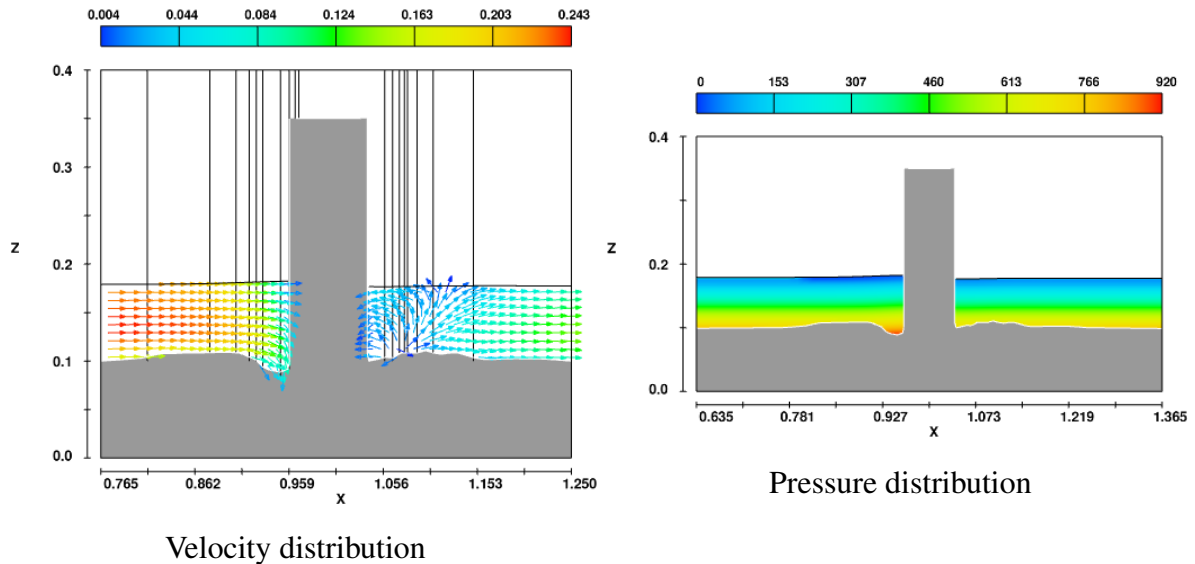


Figure 4.46: Velocity and pressure distribution for square pier in ZX plane

For diamond pier in Figure 4.47, pressure gradients at the front and rear section of the pier are $993Pa$ and $828Pa$, respectively. According to the velocity distribution graph, the wake region of the diamond pier is located close to the pier same as the cylindrical pier. This is because the diamond pier has sharp noses at the front, rear, and sides of the pier, which is a more streamlined shape than the square pier. The diamond pier occupies a large area of wake region than the cylindrical pier's wake region because of its geometry.

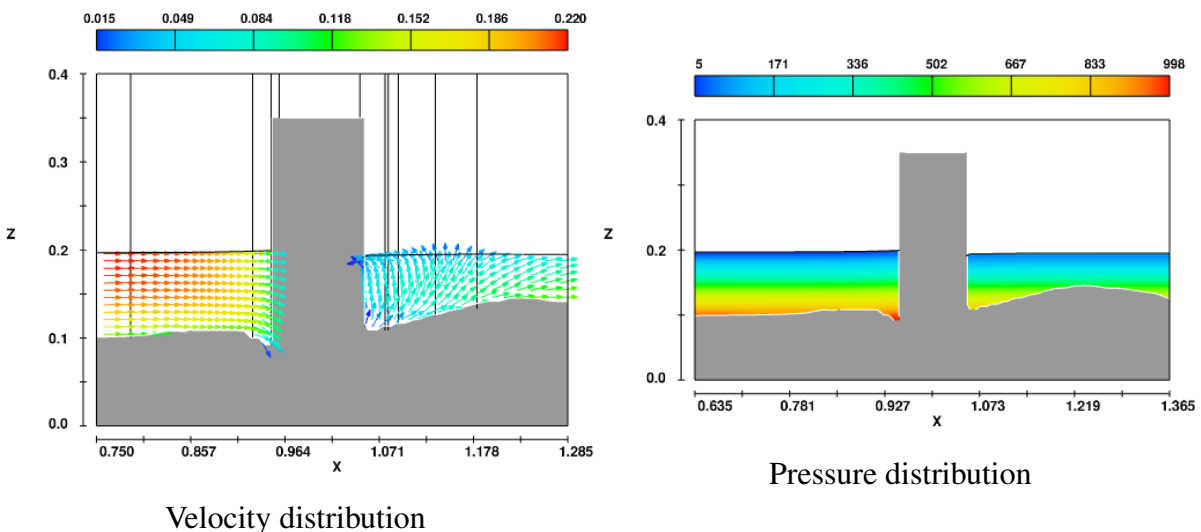


Figure 4.47: Velocity and pressure distribution for diamond pier in ZX plane

For hexagonal-sharp nose pier in Figure 4.48, pressure gradients at the front and rear section of the pier are $845Pa$ and $704Pa$, respectively. According to the velocity distribution graph, the wake region of the hexagonal-sharp nose pier is located almost close to the pier. This is because the hexagonal-sharp nose pier has sharp noses at the front and rear, which is more streamlined than the square pier. The outward direction of the velocity vector represents the formation of eddies in the wake region.

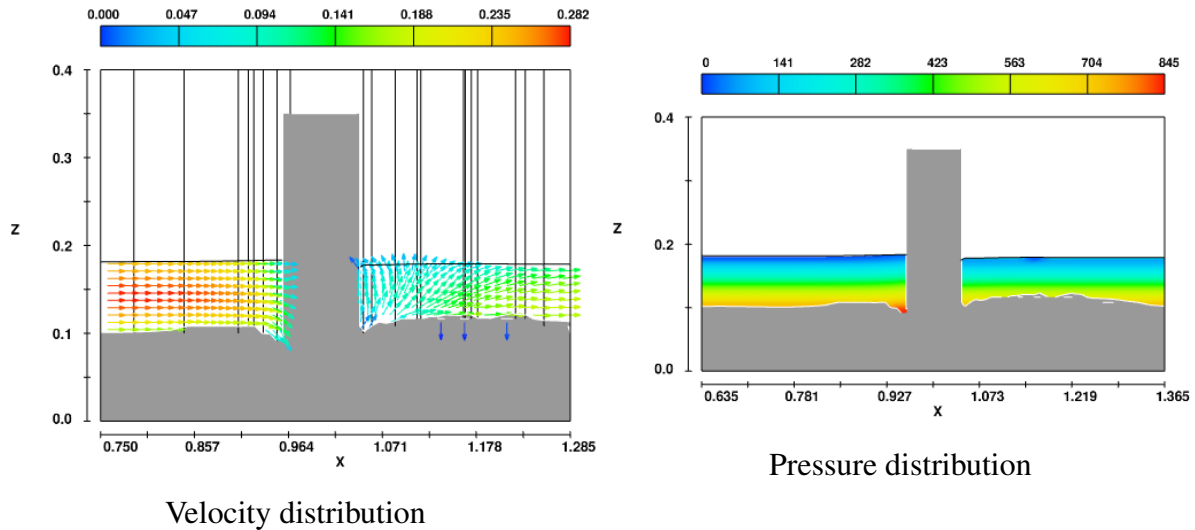


Figure 4.48: Velocity and pressure distribution for hexagonal-sharp nose pier in ZX plane

For hexagonal-vertical nose pier in Figure 4.49, pressure gradients at the front and rear section of the pier are $964Pa$ and $804Pa$, respectively. From the velocity distribution graph, the wake region of the hexagonal-vertical nose pier is located almost close to the pier. This is because the hexagonal-vertical nose pier has sharp noses at the sides of the pier, which is more streamlined than the square pier. The hexagonal-vertical nose pier occupies a large area of wake region than the cylindrical pier's wake region because of its geometry.

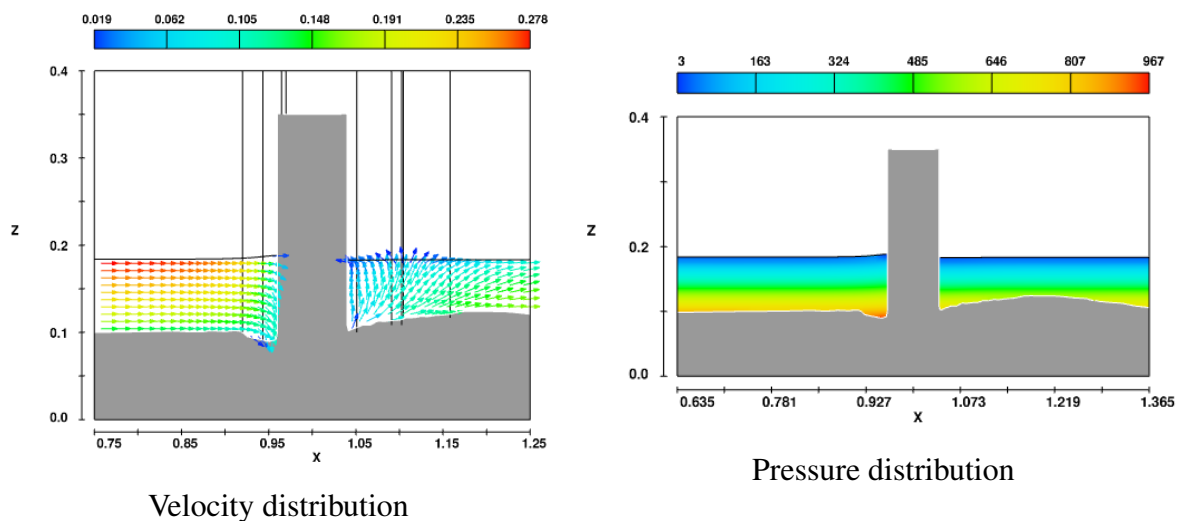


Figure 4.49: Velocity and pressure distribution for hexagonal-vertical nose pier in ZX plane

For airfoil pier in Figure 4.50, pressure gradients at the front and rear section of the pier are $886Pa$ and $1064Pa$, respectively. From the velocity distribution graph, there are few outward velocity vectors at the rear of the pier, unlike the previous shapes. The airfoil pier has a more streamlined shape, which prohibits the formation of many eddies and wake vortices. Therefore, there is a relatively small wake region at the rear of the airfoil pier. The flow is almost laminar for the airfoil pier.

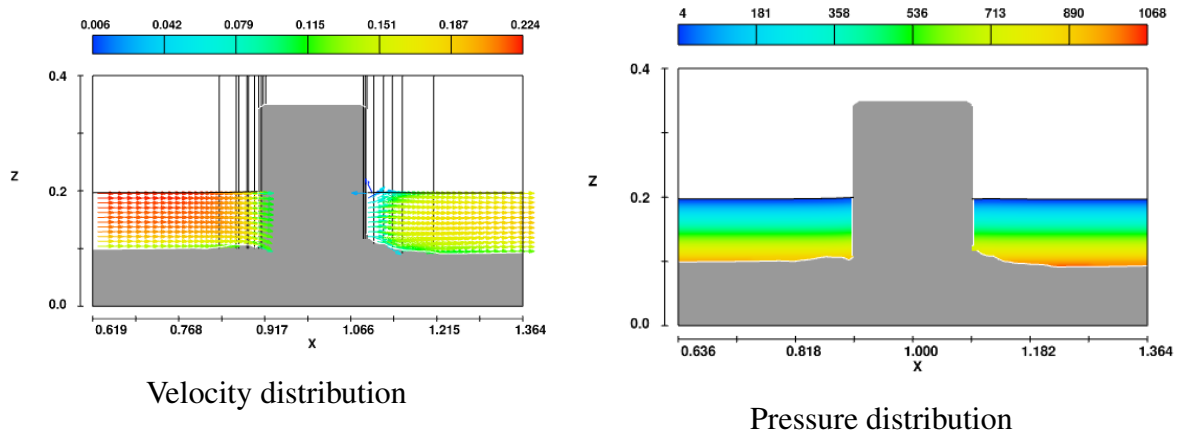


Figure 4.50: Velocity and pressure distribution for airfoil pier in ZX plane

For upstream facing airfoil pier in Figure 4.51, pressure gradients at the front and rear section of the pier are $852Pa$ and $710Pa$, respectively. From the velocity distribution graph, there are no outward velocity vectors at the rear of the pier, unlike the other piers. The streamlined shape with a sharp end of the upstream facing airfoil pier prohibits the formation of eddies and wake vortices. Therefore, there is no such wake region at the rear of the pier. The flow is entirely laminar for the upstream facing airfoil pier.

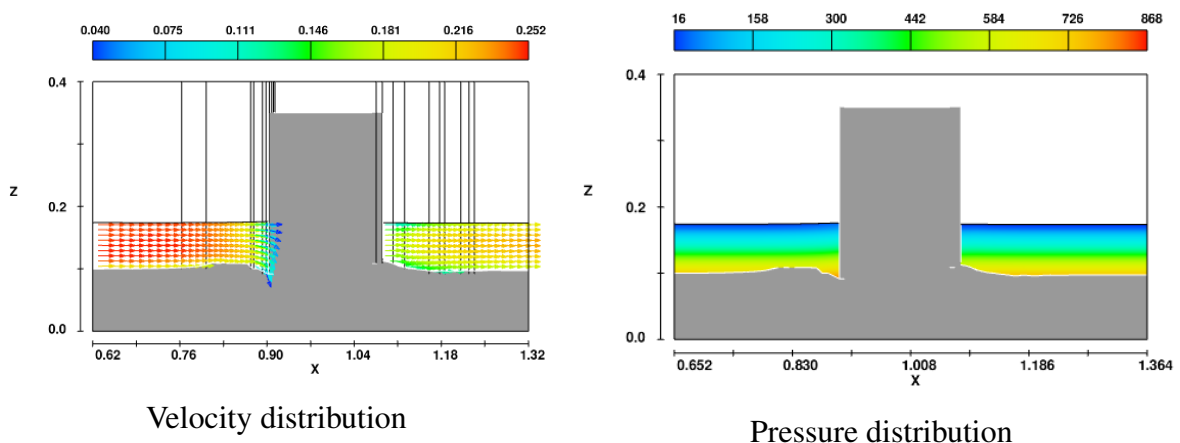


Figure 4.51: Velocity and pressure distribution for upstream facing airfoil pier in ZX plane

For downstream facing airfoil pier in Figure 4.52, pressure gradients at the front and rear section of the pier are $753Pa$ and $903Pa$, respectively. From the velocity distribution graph, there are many outward velocity vectors at the rear of the pier, unlike the upstream facing airfoil pier. The streamlined shape with a round end of the downstream facing airfoil pier promotes the formation of eddies and wake vortices. Therefore, the wake region formed at the rear of the pier and is located close to the pier.

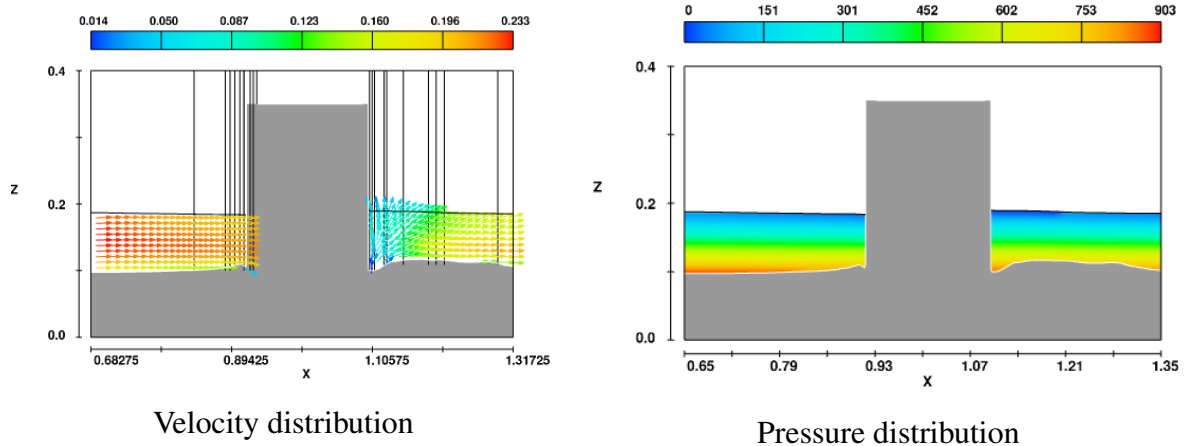


Figure 4.52: Velocity and pressure distribution for downstream facing airfoil pier in ZX plane

For oblong pier in Figure 4.53, pressure gradients at the front and rear section of the pier are $991Pa$ and $661Pa$, respectively. From the velocity distribution graph, there are few outward velocity vectors at the rear of the pier occupying a smaller region. Hence the wake region formed at the rear of the pier and is located close to the pier. After the wake region, the flow becomes laminar again.

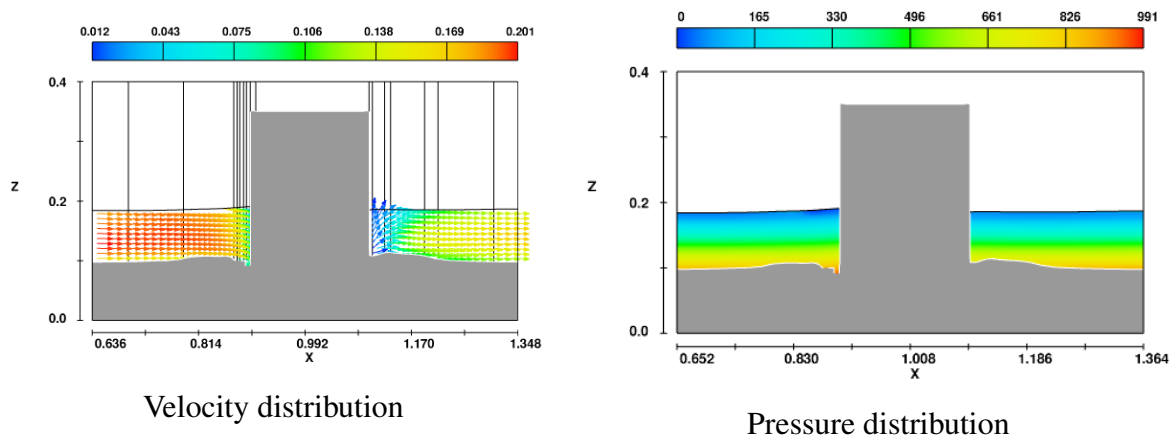


Figure 4.53: Velocity and pressure distribution for oblong pier in ZX plane

For rectangle pier in Figure 4.54, pressure gradients at the front and rear section of the pier are $1011Pa$ and $845Pa$, respectively. From the velocity distribution graph, the wake region of the rectangular pier is located a bit further from the pier, which is the same as the square pier. This is because the edges of the rectangle pier are not streamlined, and these edges resist creating a streamlined flow.

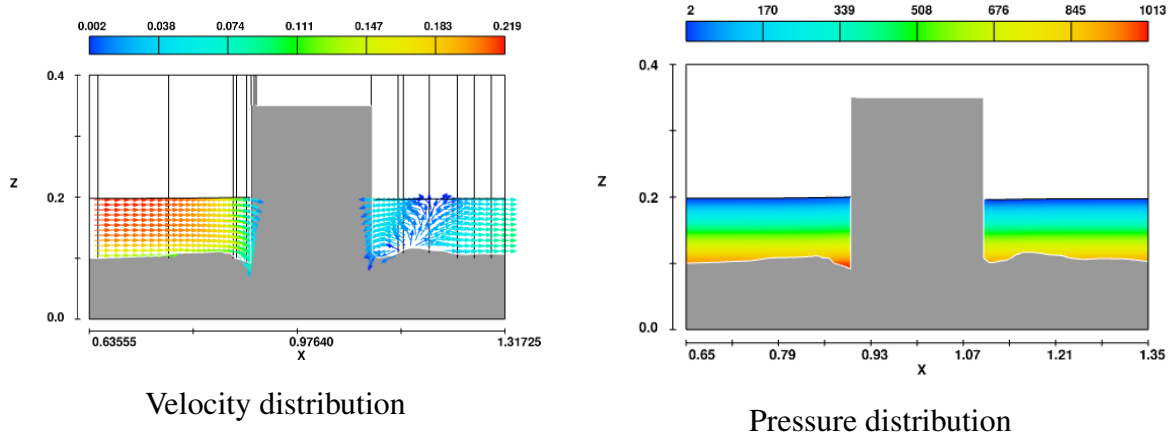


Figure 4.54: Velocity and pressure distribution for rectangle pier in ZX plane

4.3 Time Dependent Analysis Of Scour Depth And Sediment Deposition

The impact of local scour around the structural piers increases over time, and it is crucial to run the simulation for a very long period. In this study, the simulation runs for 1000s or 16.5 minutes to reach the equilibrium conditions. At the beginning of the simulation, the effect of scouring is more negligible. When the simulation runs for a long period, it severely impacts the scouring process. This is because the velocity around the piers changes progressively, and the horseshoe vortex becomes the dominant factor. Both the scour depth and sand deposition depend on time. Herein, scour depth and sediment deposition over time have been discussed.

4.3.1 Scour Depth Over Time

From Figure 4.55, for cylindrical, square, diamond, hexagonal-sharp nose, hexagonal-vertical nose piers, it takes 300s, 350s, 300s, 450s, 300s, respectively, to reach the equilibrium conditions. Among these piers, it takes more time for the diamond pier to reach equilibrium because it has a more streamlined shape, allowing larger scour depth and sand deposition. For airfoil, upstream facing airfoil, downstream facing airfoil, oblong, rectangle, it takes 400s, 500s, 700s, 500s, 300s, respectively, to reach the equilibrium conditions. The downstream facing pier takes longer to reach the equilibrium conditions due to its geometry. The second set of piers takes

more time to get the equilibrium conditions because their lengths are more extended than the first set and have a more streamlined shape.

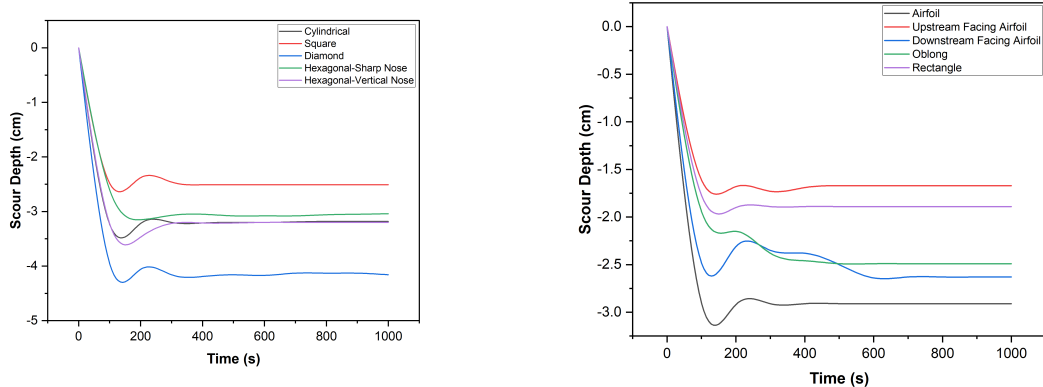


Figure 4.55: Scour depth vs Time

4.3.2 Sediment Deposition Over Time

From Figure 4.56, the diamond pier has the highest sand depositions because of its sharp edge geometry. The rate of sand depositions for this pier increases over time and does not reach the equilibrium conditions within 1000s. For the cylindrical, square, hexagonal-sharp nose, hexagonal-vertical nose piers, it takes 200s, 200s, 700s, and 900s for the sediment depositions to reach equilibrium. The downstream facing airfoil has more irregular sediment depositions up to 800s because of its shape. For airfoil, upstream facing airfoil, oblong, rectangle piers, it takes 400s, 300s, 600s, 400s for the sediment depositions to reach equilibrium.

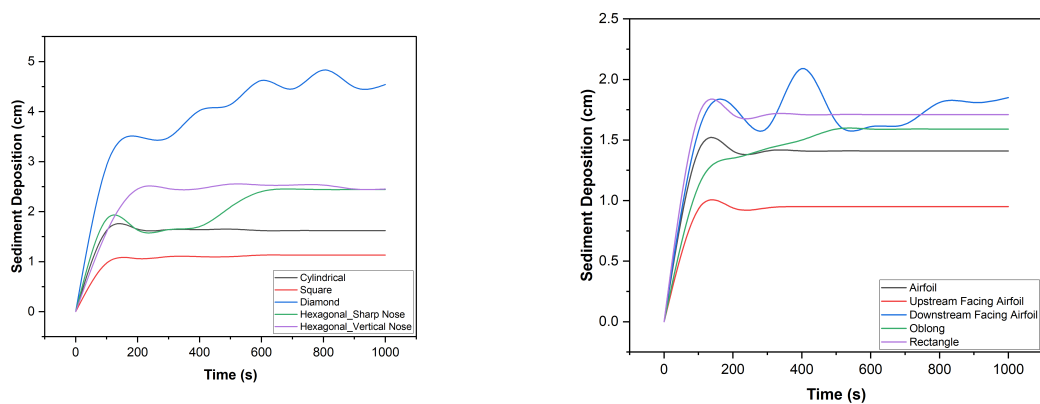


Figure 4.56: Sediment deposition vs Time

4.4 Reduction Of Local Scour

It is vital to diminish the scouring effect around the bridge piers and increase the lifespan of the hydraulic structures. Two methods have been employed in this study to minimize the impact of local scour and the scour depth around the piers.

- Using tapered shape bridge piers
- Using collar plate around the piers

4.4.1 Tapered Cylindrical Bridge Piers

Tapered shape drastically decreases the scour depth around the tapered cylindrical bridge pier. From Table 3.4, the taper angle for cylindrical pier and tapered cylindrical pier are 0° and 2.45° , respectively. The dimensions of the tapered cylindrical are given in Table 3.4. Figure 4.57 displays the 3D model of the piers.

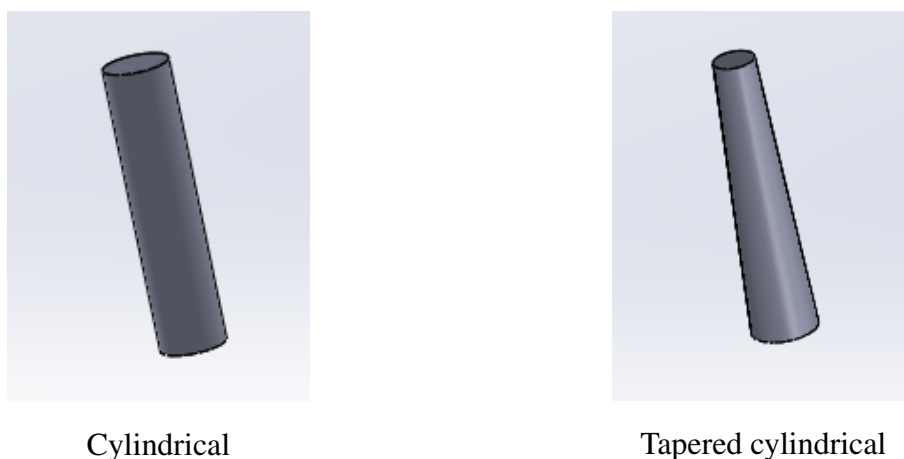


Figure 4.57: 3D sketch of non-tapered vs tapered cylindrical pier

From Figure 4.58, the maximum scour depth and sand deposition for the tapered cylindrical pier are 2.1cm and 2.11cm , respectively. For the non-tapered cylindrical pier, the scour depth and sediment deposition is 3.18cm and 1.62cm from Table 4.1. The scour depth and sediment deposition of the tapered cylindrical pier are 33.96% less and 30% higher than the non-tapered cylindrical pier, respectively. The percentage change in scour depth is shown in Table 4.4.

For tapered cylindrical pier in Figure 4.59, pressure gradients at the front and rear section of the pier are 829Pa and 691Pa , respectively. According to the velocity distribution graph, the wake region of the tapered cylindrical pier is located close to the pier, same as the non-tapered cylindrical pier in Figure 4.45. The tapered cylindrical pier occupies a large area of wake region than the non-tapered cylindrical pier's wake region because of its tapered geometry. The flow

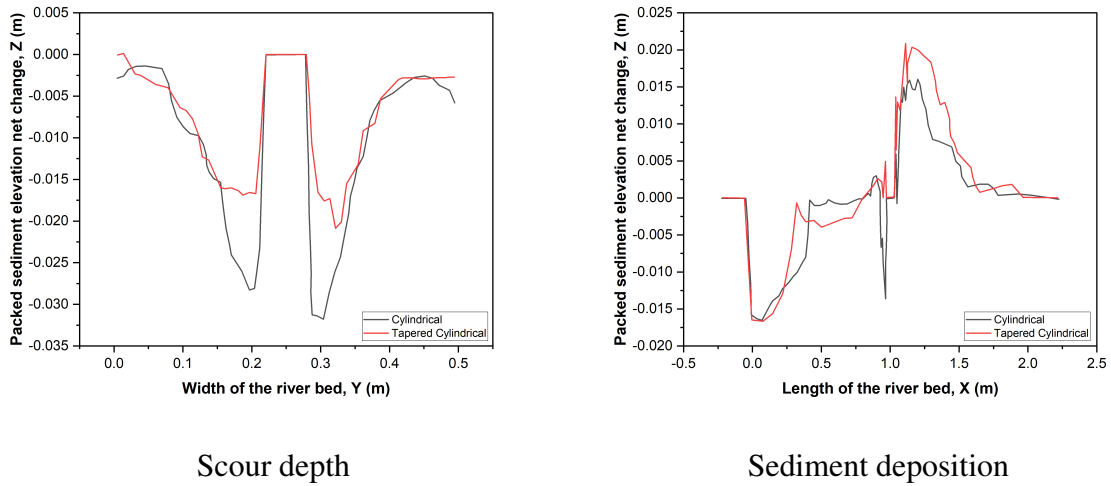


Figure 4.58: Packed sediment elevation net change for non-tapered vs tapered cylindrical pier

Table 4.4: Percentage change in scour depth for tapered cylindrical pier

Pier Geometry	Scour Depth (cm)	Percentage Change
Cylindrical	3.18	+51.43%
Tapered cylindrical	2.10	-33.96%

velocity at the wake region of the tapered and non-tapered cylindrical pier are $0.024ms^{-1}$ to $0.066ms^{-1}$ and $0.001ms^{-1}$ to $0.045ms^{-1}$, respectively.

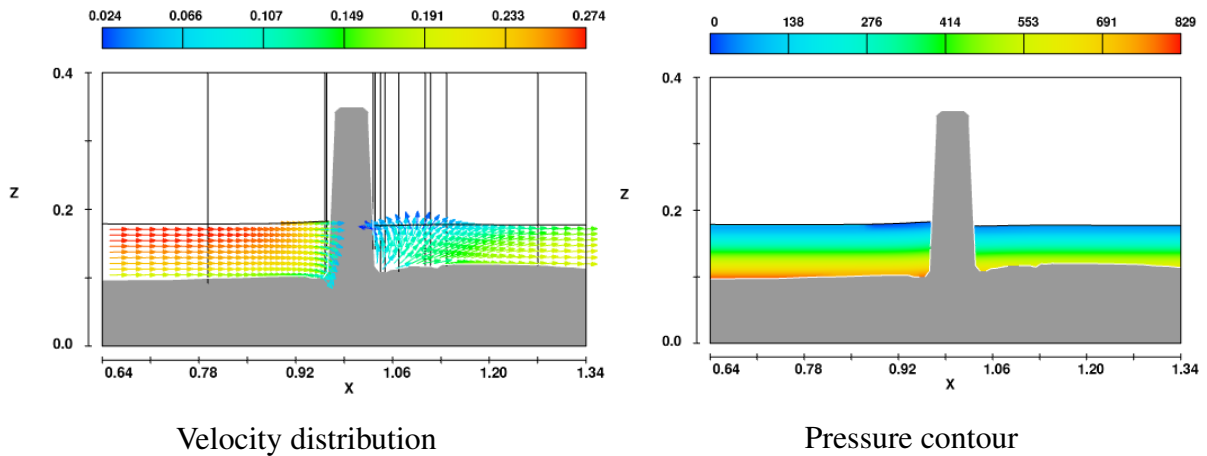


Figure 4.59: Velocity distribution and pressure contour of the tapered cylindrical pier

4.4.2 Tapered Hexagonal Bridge Piers

The scour depth of the tapered hexagonal pier is comparatively less than the non-tapered hexagonal pier. From Table 3.4, the taper angle for hexagonal pier and tapered hexagonal pier are 0° and 2.45° , respectively. The dimensions of the tapered hexagonal are given in Table 3.4. Figure 4.60 displays the 3D model of the piers.

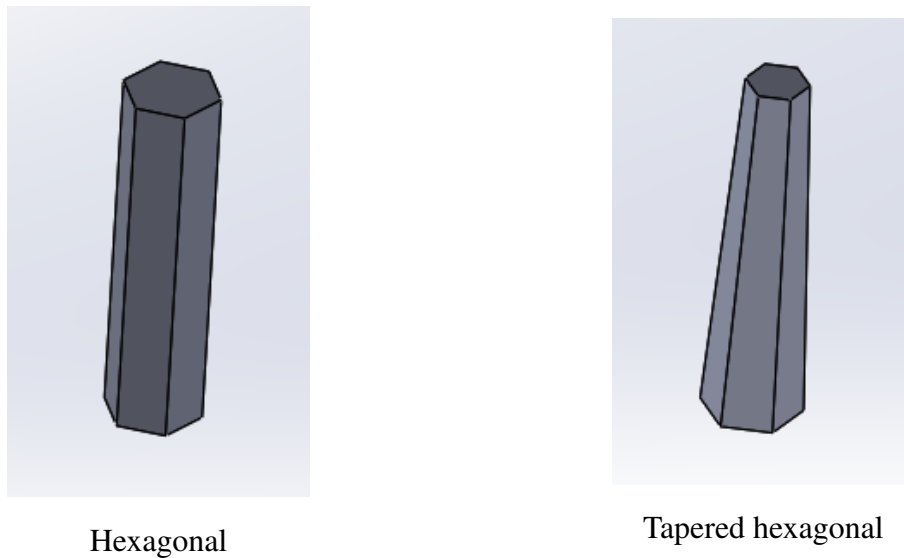


Figure 4.60: 3D sketch of non-tapered vs tapered hexagonal-sharp nose pier

From Figure 4.61, the maximum scour depth and sand deposition for the tapered hexagonal-sharp nose pier are 2.6cm and 3.29cm , respectively. For the non-tapered hexagonal-sharp nose pier, the scour depth and sediment deposition is 3.04cm and 2.44cm from Table 4.1. The scour depth and sediment deposition of the tapered hexagonal-sharp nose pier are 14.47% less and 34.8% higher than the non-tapered hexagonal-sharp nose pier pier, respectively. The percentage change in scour depth is shown in Table 4.5.

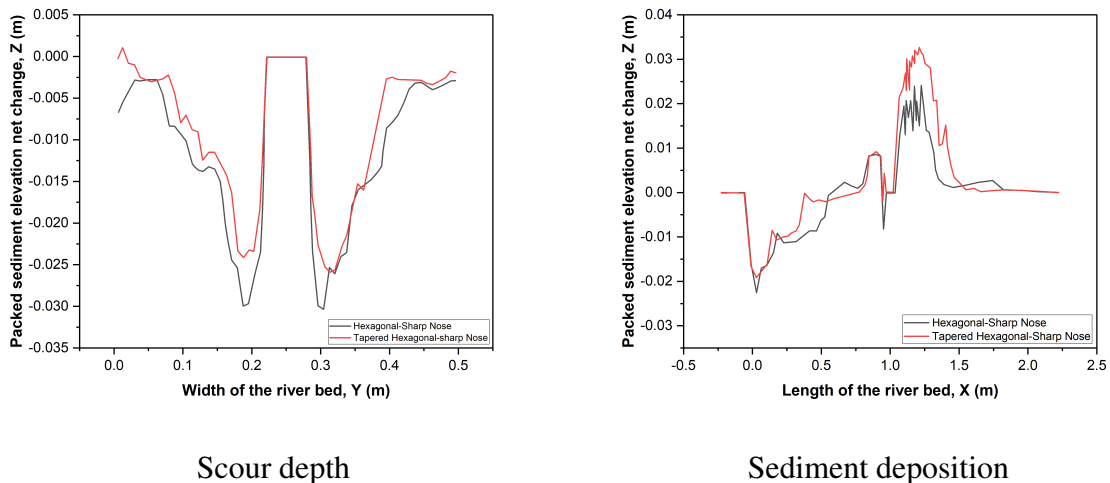


Figure 4.61: Packed sediment elevation net change for non-tapered vs tapered hexagonal-sharp nose pier

For tapered hexagonal-sharp nose pier in Figure 4.62, pressure gradients at the front and rear section of the pier are 871Pa and 588Pa , respectively. According to the velocity distribution graph, the wake region of the tapered hexagonal-sharp nose pier is located close to the pier, the same as the non-tapered hexagonal-sharp nose pier in Figure 4.48. The range of flow velocity

Table 4.5: Percentage change in scour depth for tapered hexagonal-sharp nose pier

Pier Geometry	Scour Depth (cm)	Percentage Change
Hexagonal	3.04	+16.92%
Tapered hexagonal	2.60	-14.47%

at the wake region of the tapered and non-tapered hexagonal-sharp nose pier are 0.014m s^{-1} to 0.056m s^{-1} and 0.00m s^{-1} to 0.047m s^{-1} , respectively.

Using a tapered shape can effectively reduce scour depth. Both the tapered cylindrical and hexagonal-sharp nose piers reduce local scour. In Bangladesh, the Padma Multipurpose Bridge spans the Padma River, offering road-rail access to the city. The total length is 6,150 m (20,180 ft), and 42 piers have been used. From Figure 4.63, instead of using a continuous tapered hexagonal-shaped pier made of concrete, six raking steel tubular piles have been attached at an angle to the hexagonal pier cap. The entire pier has a tapered shape geometry. This is because there is a higher level of stability for raking piles in terms of resisting lateral loads from earthquake motions [50]. Adding a large number of piles can make the pile cap heavier and contribute to scouring. So the number of piles is limited to six to seven to reduce local scour.

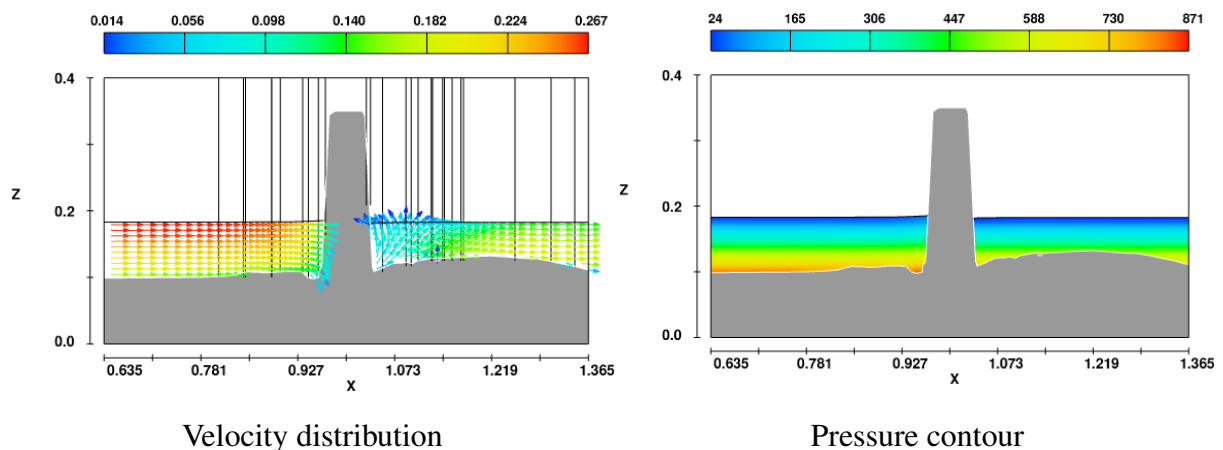


Figure 4.62: Velocity distribution and pressure contour of the tapered hexagonal-sharp nose pier



Figure 4.63: The Padma Multipurpose Bridge, Bangladesh

4.4.3 Anti-Scour Collar Plates

In Figure 4.64, attaching a collar plate to the pier creates an impassable barrier against horseshoe vortices. It prevents the vortices from directly impacting the river bed by reducing the force of down-flow and horseshoe vortices. The collar plate will reduce local scour if it is mounted at or below the average bed level [51]. Positioning the collar plate below the bed level will increase its effectiveness. Scouring can be reduced through multiple collar plate placement with one collar plate above the bed level and one under it [52]. The position of the collar plates around the cylindrical bridge pier has been shown in Table 4.6, Figure 4.66, and Figure 4.67.

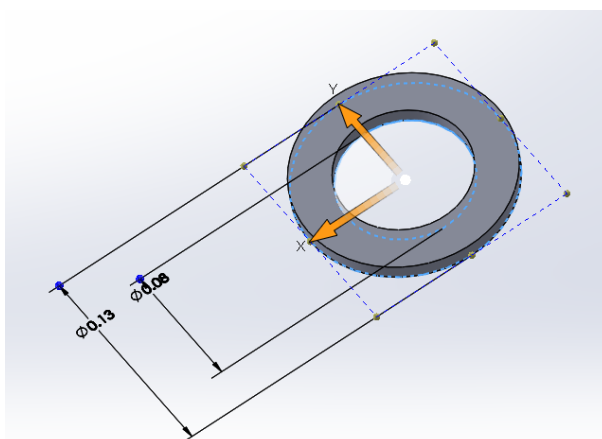


Figure 4.64: Collar plate

Scour depths for the different arrangements of the collar plates (Test 1-10) around the cylindrical pier have been compared in Figure 4.65. Attaching collar plates above bed level (Test 2-7) will increase scour depth while placing the collar plates below bed level (Test 8-9) will reduce scour depth. Test 10 shows that scour depth will decrease the most if one collar plate attaches under the bed level and one above the bed level.

Table 4.6: Scour depth with multiple collar plates attaching to the cylindrical pier in cm

Test	No of Collar Plate	Distance From Bed Surface	Scour Depth	Sand Deposition
Test 1	1	0	3.93	1.51
Test 2	1	2	3.46	2.78
Test 3	2	2, 4	3.48	3.25
Test 4	3	2, 4, 6	3.53	2.49
Test 5	1	6	2.98	1.72
Test 6	2	6, 8	3.02	2.19
Test 7	3	4, 6, 8	3.30	2.48
Test 8	1	-2	2.42	1.62
Test 9	1	-2.5	2.50	1.66
Test 10	2	-2, 6	2.32	2.50

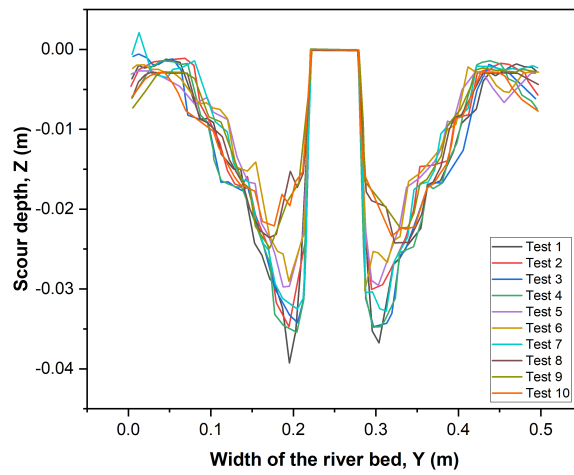


Figure 4.65: Effect of collar plates on scour depths

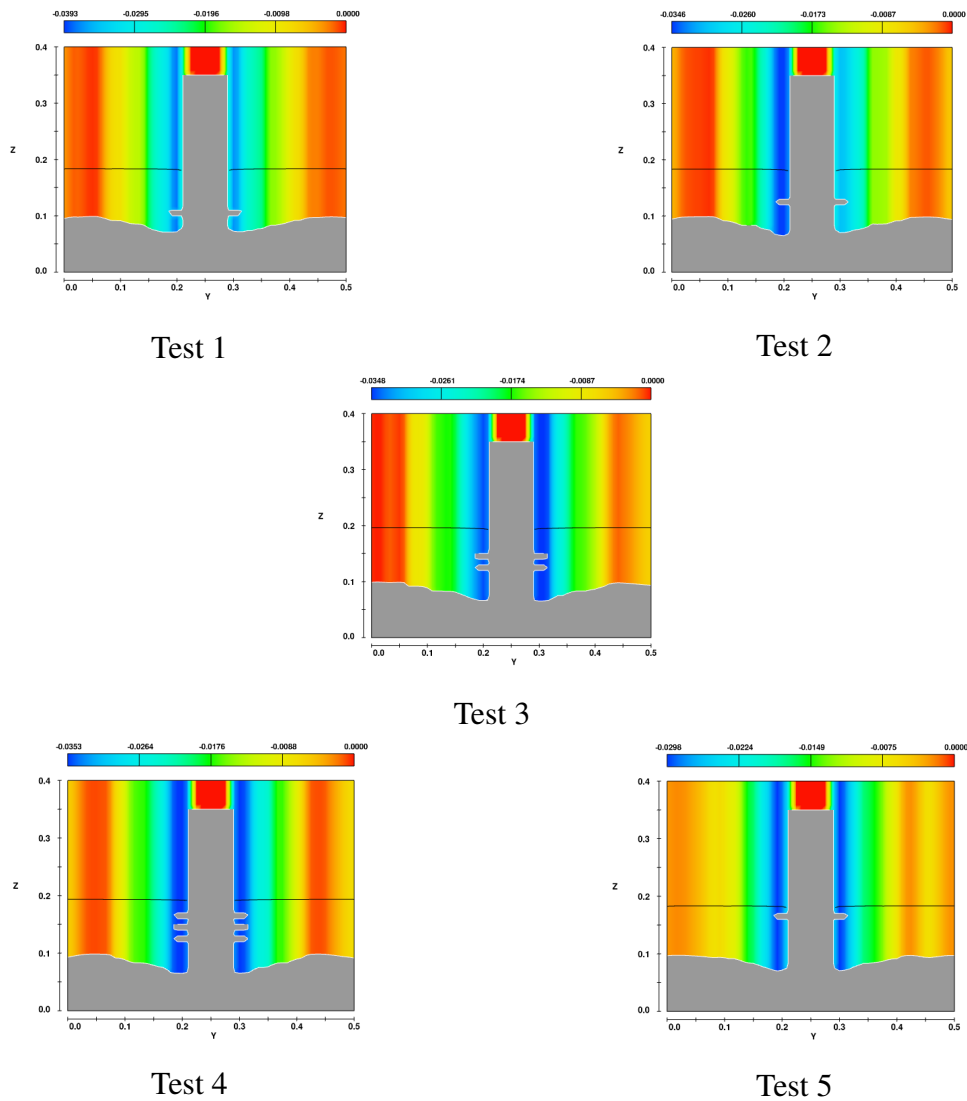
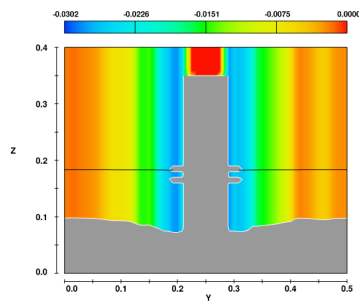
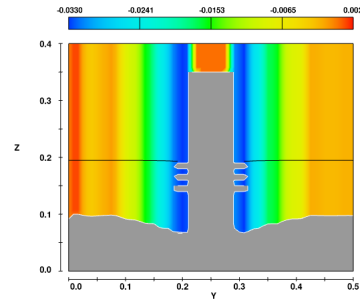


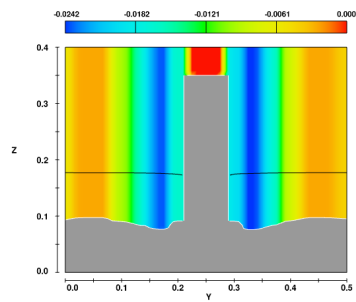
Figure 4.66: 2D contour plot of scour depth in the presence of collar plates



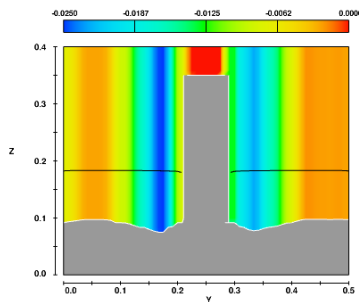
Test 6



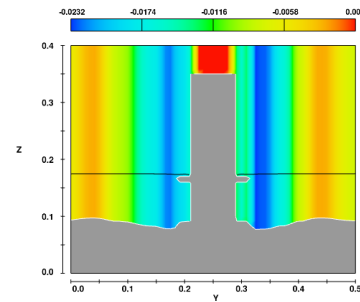
Test 7



Test 8



Test 9



Test 10

Figure 4.67: 2D contour plot of scour depth in the presence of collar plates

4.5 Effective Pier Geometry For Bridge Construction

From Figure 4.68 and Table 4.7, the scour depth of the tapered cylindrical pier is 33.96% and 9.48% less than the cylindrical pier and cylindrical pier with one collar plate under the bed level and one above the bed level, respectively. The bridge with cylindrical piers that are not tapered may collapse sooner than the bridge with cylindrical piers that are tapered. The stability of hydraulic structures can be improved by the tapered cylindrical-shaped pier, which can lessen the scouring impact. With a longer lifespan, this pier will be effective for bridge construction.

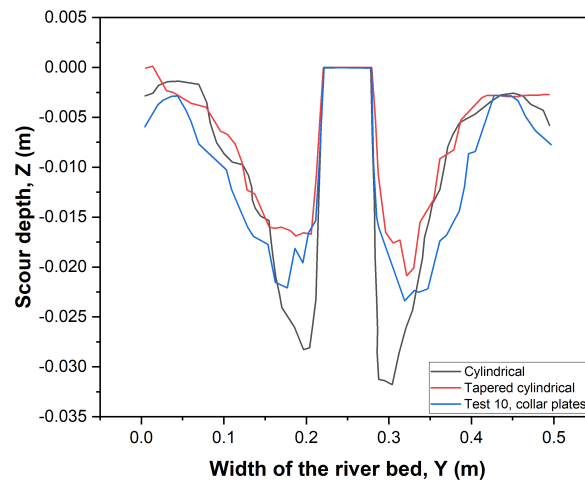


Figure 4.68: Comparing the scour depth for cylindrical, tapered cylindrical, and cylindrical piers with collar plates

Table 4.7: Scour depth for non-tapered cylindrical, tapered cylindrical, and cylindrical pier with collar plates

Pier Geometry	Scour Depth (<i>cm</i>)
Cylindrical	3.18
Tapered cylindrical	2.10
Test 10, collar plates	2.32

Chapter 5

Conclusions and Recommendations

5.1 Conclusions

In this study, the local scour around the different geometry of the structural bridge piers has been discussed to find the most efficient shape with the lowest scour depth. The investigations' findings are summarized as follows:

- There are two sets of simulations results. The first set includes the cylindrical, square, diamond, hexagonal-sharp nose, and hexagonal-vertical nose pier. The second set comprises airfoil, upstream facing airfoil, downstream facing airfoil, oblong, and rectangle pier. From the bed topography, scour depth, and time-dependent analysis, it is very clear that the square, the upstream facing airfoil, and the rectangle shape piers have the minimum scour depth.
- The square shape pier has a blunt edge at the flow direction, which is likely to create a larger scour hole at the front of the pier compared to the cylindrical and hexagonal sharp nose pier. Hence, the cylindrical, the hexagonal sharp nose, the upstream facing airfoil, and the rectangle shape piers are considered as the most suitable structures to prevent bridge collapse.
- To reduce the effect of scouring, tapered shapes of cylindrical and hexagonal-sharp nose piers have been introduced. Piers with a tapered design significantly reduce scour depth.
- Local scour is also lessened by collar plates that are wrapped around the cylindrical pier. A collar plate at bed level will result in more scouring. If collar plates are positioned above the bed level, local scour will increase; if collar plates are positioned below the bed level, local scour will decrease. The findings show that the most effective way to prevent

local scour is to combine one collar plate above the bed level with one collar plate below the bed level.

- It is evident that the tapered cylindrical pier has the lowest scour depth after comparing the result with the cylindrical pier having collar plates.
- There are a few limitations to this study. The tapered shape has not been implied on all the shapes mentioned in this study. Two suitable shapes, cylindrical and hexagonal-sharp nose pier, have been chosen to compare with their corresponding tapered shape.

5.2 Recommendations

This study aims to reduce the scour depth. It is necessary to reduce the impact of flow on the surface of the structural piers to accomplish this. Additional structures like collar plates have been attached to the cylindrical pier to minimize the scour depths. Herein, two more additional shapes can be considered, the horizontal splitter and the vertical plate in Figure 5.1. To evaluate the effectiveness of these structures, they should be attached to the cylindrical pier.

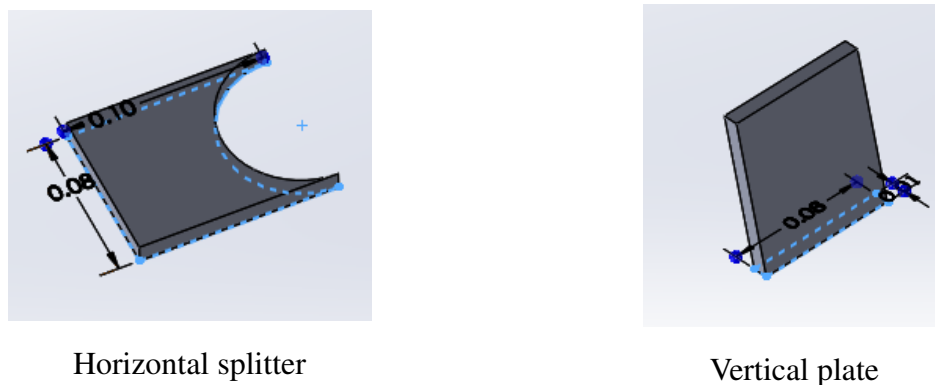
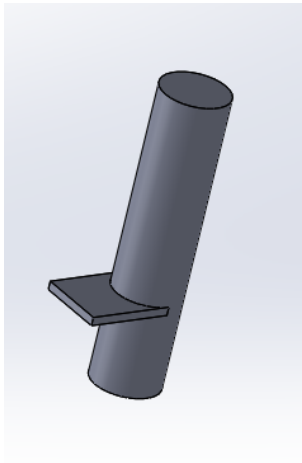


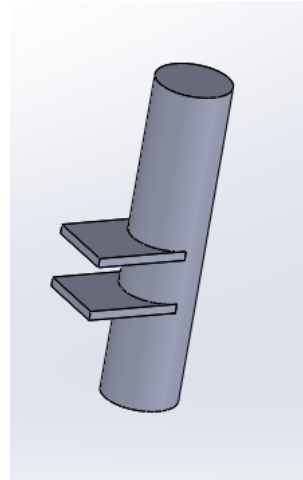
Figure 5.1: 3D model of splitter and plate

From Figure 5.2, multiple splitters have been attached to the wall of the cylindrical pier. A front and a back plate have also been attached to the cylindrical pier in Figure 5.3.

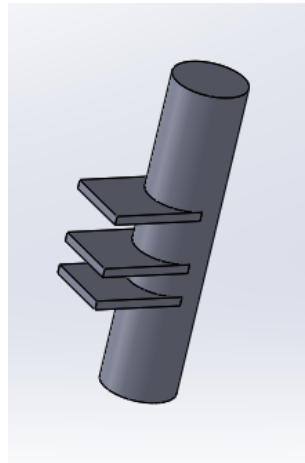
Therefore, it is recommended to conduct more numerical analysis in the future, taking into account the different diameters of the circular pier as well as the various dimensions and positions of the splitter and plate attached to the pier to estimate the lowest scour depth. Moreover, research can be conducted on the varying ratio of pier diameter to height and collar plate outer diameter to its thickness. The accurate architecture of the structural piers is a demanding topic in river engineering.



Single splitter

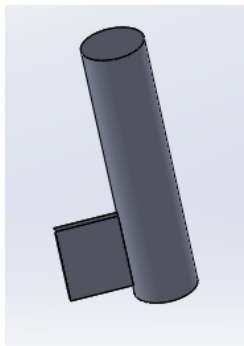


Double splitter

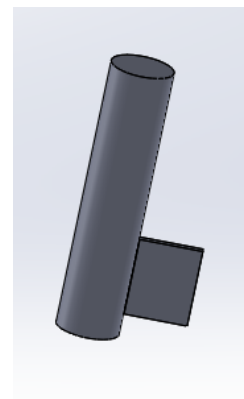


Tripple splitter

Figure 5.2: Multiple splitters attached to the cylindrical pier



Front plate



Back plate

Figure 5.3: Front and back plate attached to the cylindrical pier

References

- [1] C. González, D. H. Richter, D. Bolster, S. Bateman, J. Calantoni, and C. Escauriaza, “Characterization of bedload intermittency near the threshold of motion using a lagrangian sediment transport model,” *Environmental Fluid Mechanics*, vol. 17, no. 1, pp. 111–137, 2017.
- [2] A. M. Tawfik, “Best non scour channel section design using artificial neural networks,” *Ain Shams Engineering Journal*, vol. 12, no. 2, pp. 1283–1291, 2021.
- [3] Y. Sonia Devi and A. Barbhuiya, “Bridge pier scour in cohesive soil: a review,” *Sādhanā*, vol. 42, no. 10, pp. 1803–1819, 2017.
- [4] S.-U. Choi and B. Choi, “Prediction of time-dependent local scour around bridge piers,” *Water and Environment Journal*, vol. 30, no. 1-2, pp. 14–21, 2016.
- [5] A. R. Shahriar, A. C. Ortiz, B. M. Montoya, and M. A. Gabr, “Bridge pier scour: An overview of factors affecting the phenomenon and comparative evaluation of selected models,” *Transportation Geotechnics*, vol. 28, p. 100549, 2021.
- [6] Q. Xiang, K. Wei, Y. Li, M. Zhang, and S. Qin, “Experimental and numerical investigation of local scour for suspended square caisson under steady flow,” *KSCE Journal of Civil Engineering*, vol. 24, no. 9, pp. 2682–2693, 2020.
- [7] A. E.-H. Rady *et al.*, “Prediction of local scour around bridge piers: artificial-intelligence-based modeling versus conventional regression methods,” *Applied Water Science*, vol. 10, no. 2, pp. 1–11, 2020.
- [8] B. W. Melville and Y.-M. Chiew, “Time scale for local scour at bridge piers,” *Journal of Hydraulic Engineering*, vol. 125, no. 1, pp. 59–65, 1999.
- [9] E. Akhlaghi, M. S. Babarsad, E. Derikvand, and M. Abedini, “Assessment the effects of different parameters to rate scour around single piers and pile groups: a review,” *Archives of Computational Methods in Engineering*, vol. 27, no. 1, pp. 183–197, 2020.
- [10] K. Wardhana and F. C. Hadipriono, “Analysis of recent bridge failures in the united states,” *Journal of performance of constructed facilities*, vol. 17, no. 3, pp. 144–150, 2003.

- [11] R. Malik and B. Setia, "Interference between pier models and its effects on scour depth," *SN Applied Sciences*, vol. 2, no. 1, pp. 1–12, 2020.
- [12] M. Rasaei, S. Nazari, and S. Eslamian, "Experimental investigation of local scouring around the bridge piers located at a 90 convergent river bend," *Sādhanā*, vol. 45, no. 1, pp. 1–15, 2020.
- [13] Q. Zhang, X.-L. Zhou, and J.-H. Wang, "Numerical investigation of local scour around three adjacent piles with different arrangements under current," *Ocean Engineering*, vol. 142, pp. 625–638, 2017.
- [14] Y. Jia, M. Altinakar, and M. S. Guney, "Three-dimensional numerical simulations of local scouring around bridge piers," *Journal of Hydraulic Research*, vol. 56, no. 3, pp. 351–366, 2018.
- [15] P. Lagasse, E. Richardson, J. Schall, and G. Price, "Instrumentation for measuring scour at bridge piers and abutments," *TRB, National Research Council, Washington, DC*, 1997.
- [16] K. H. LeBeau and S. J. Wadia-Fascetti, "Fault tree analysis of schoharie creek bridge collapse," *Journal of Performance of Constructed Facilities*, vol. 21, no. 4, pp. 320–326, 2007.
- [17] J.-H. Hong, Y.-M. Chiew, J.-Y. Lu, J.-S. Lai, and Y.-B. Lin, "Houfeng bridge failure in taiwan," *Journal of Hydraulic Engineering*, vol. 138, no. 2, pp. 186–198, 2012.
- [18] E. Halliday, "Flood-damaged bishopsford road bridge will be demolished and rebuilt for £2.7 million," accessed Feb. 3, 2022. <https://www.swlondoner.co.uk/news/05032020-bridge-damaged-by-floods-will-be-demolished-and-rebuilt-for-2-7-million>.
- [19] C. Wang, X. Yu, and F. Liang, "A review of bridge scour: mechanism, estimation, monitoring and countermeasures," *Natural Hazards*, vol. 87, no. 3, pp. 1881–1906, 2017.
- [20] M. Kayser and M. A. Gabr, "Assessment of scour on bridge foundations by means of in situ erosion evaluation probe," *Transportation Research Record*, vol. 2335, no. 1, pp. 72–78, 2013.
- [21] D. M. Sheppard and J. S. Jones, "Scour at complex pier geometries," in *Stream Stability and Scour at Highway Bridges: Compendium of Stream Stability and Scour Papers Presented at Conferences Sponsored by the Water Resources Engineering (Hydraulics) Division of the American Society of Civil Engineers*, pp. 365–370, ASCE, 1998.
- [22] B. S. Abed and H. Q. Majeed, "The behavior of scouring around multiple bridge piers having different shapes," in *IOP Conference Series: Materials Science and Engineering*, vol. 745, p. 012158, IOP Publishing, 2020.

- [23] Y. Yang, B. W. Melville, G. H. Macky, and A. Y. Shamseldin, "Experimental study on local scour at complex bridge pier under combined waves and current," *Coastal Engineering*, vol. 160, p. 103730, 2020.
- [24] J. Wang, K. Wang, B.-h. Fang, and J. Sui, "A revisit of the local scour around bridge piers under an ice-covered flow condition—an experimental study," *Journal of Hydrodynamics*, vol. 33, no. 5, pp. 928–937, 2021.
- [25] S. I. Ahmed and S. I. Khassaf, "Study the local scour around different shapes of non-uniform piers," *Basrah J Eng Sci*, vol. 20, no. 1, pp. 12–14, 2020.
- [26] N. Raeisi and M. Ghomeshi, "Effect of bridge pier diameter on maximum depth of scour impacts on the environment," *SN Applied Sciences*, vol. 2, no. 11, pp. 1–12, 2020.
- [27] T. A. GELMIRAN, K. I. Othman, and M. GUNAL, "Investigation of local scour around group bridge pier with different shapes," *Al-Rafidain Engineering Journal (AREJ)*, vol. 24, no. 2, pp. 10–22, 2019.
- [28] D. Dehghan, M. Vaghefi, and M. Ghodsian, "Experimental study of the effect of the length-to-width ratio and skewness angles of the pier installed at the bend on scour pattern," *Journal of the Brazilian Society of Mechanical Sciences and Engineering*, vol. 43, no. 3, pp. 1–17, 2021.
- [29] A. Ismael, M. Gunal, and H. Hussein, "Effect of bridge pier position on scour reduction according to flow direction," *Arabian Journal for Science and Engineering*, vol. 40, no. 6, pp. 1579–1590, 2015.
- [30] A. Bordbar, S. Sharifi, and H. Hemida, "Investigation of the flow behaviour and local scour around single square-shaped cylinders at different positions in live-bed," *Ocean Engineering*, vol. 238, p. 109772, 2021.
- [31] R. Hasan and R. Khan, *Numerical Investigation of Local Scour Around Different Shaped Bridge Piers Using Flow-3d Software*. PhD thesis, Department of Mechanical and Production Engineering, Islamic University of Technology, 2019.
- [32] R. Mohammadpour, A. A. Ghani, M. Vakili, and T. Sabzevari, "Prediction of temporal scour hazard at bridge abutment," *Natural Hazards*, vol. 80, no. 3, pp. 1891–1911, 2016.
- [33] B. Sanahmadi, M. Heydari, and S. Shabanlou, "A reliable non-tuned machine learning approach for local scouring simulation around twin bridge piers," *Iranian Journal of Science and Technology, Transactions of Civil Engineering*, pp. 1–14, 2022.
- [34] M. Najafzadeh and G. Oliveto, "More reliable predictions of clear-water scour depth at pile groups by robust artificial intelligence techniques while preserving physical consistency," *Soft Computing*, vol. 25, no. 7, pp. 5723–5746, 2021.

- [35] S.-U. Choi and S. Choi, "Prediction of local scour around bridge piers in the cohesive bed using support vector machines," *KSCE Journal of Civil Engineering*, vol. 26, no. 5, pp. 2174–2182, 2022.
- [36] Q. Chen, Z. Yang, and H. Wu, "Evolution of turbulent horseshoe vortex system in front of a vertical circular cylinder in open channel," *Water*, vol. 11, no. 10, p. 2079, 2019.
- [37] J. Unger and W. H. Hager, "Down-flow and horseshoe vortex characteristics of sediment embedded bridge piers," *Experiments in Fluids*, vol. 42, no. 1, pp. 1–19, 2007.
- [38] M. Pregnolato, L. Prendergast, P. Vardanega, P. Giordano, and M. Limongelli, "Risk-based bridge scour management: A survey," in *Bridge maintenance, safety, management, life-cycle sustainability and innovations*, pp. 693–701, CRC Press, 2021.
- [39] S. H. Hong and I. Abid, "Physical model study of bridge contraction scour," *KSCE Journal of Civil Engineering*, vol. 20, no. 6, pp. 2578–2585, 2016.
- [40] P. R. Orszag, "America's bridges need greater investment to survive," accessed March 12, 2022. <https://www.bloomberg.com/opinion/articles/2021-05-04/america-s-bridges-need-greater-investment-to-survive>.
- [41] M. Ghasemi and S. Soltani-Gerdefaramarzi, "The scour bridge simulation around a cylindrical pier using flow-3d," *Journal of Hydrosociences and Environment*, vol. 1, no. 2, pp. 46–54, 2017.
- [42] J.-H. Tang and A. D. Puspasari, "Numerical simulation of local scour around three cylindrical piles in a tandem arrangement," *Water*, vol. 13, no. 24, p. 3623, 2021.
- [43] S. Abdelaziz, M.-D. Bui, and P. Rutschmann, "Numerical simulation of scour development due to submerged horizontal jet," *River Flow 2010*, pp. 1597–1604, 2010.
- [44] H. H. Van Der Veen and S. M. Hulscher, "Predicting the occurrence of sand banks in the north sea," *Ocean dynamics*, vol. 59, no. 5, pp. 689–696, 2009.
- [45] T. Morales de Luna, M. Castro Díaz, and C. Parés Madroñal, "A duality method for sediment transport based on a modified meyer-peter & müller model," *Journal of Scientific Computing*, vol. 48, no. 1, pp. 258–273, 2011.
- [46] V. Yakhot, S. Orszag, S. Thangam, T. Gatski, and C. Speziale, "Development of turbulence models for shear flows by a double expansion technique," *Physics of Fluids A: Fluid Dynamics*, vol. 4, no. 7, pp. 1510–1520, 1992.
- [47] H. C. Lee and A. K. A. Wahab, "Performance of different turbulence models in predicting flow kinematics around an open offshore intake," *SN Applied Sciences*, vol. 1, no. 10, pp. 1–14, 2019.

- [48] T. M. Salaheldin, J. Imran, and M. H. Chaudhry, “Numerical modeling of three-dimensional flow field around circular piers,” *Journal of Hydraulic Engineering*, vol. 130, no. 2, pp. 91–100, 2004.
- [49] A. Khosronejad, S. Kang, and F. Sotiropoulos, “Experimental and computational investigation of local scour around bridge piers,” *Advances in Water Resources*, vol. 37, pp. 73–85, 2012.
- [50] S. Sham and M. Tapley, “The design of padma multipurpose bridge—challenges and solutions in design of the river spans,” in *Proc. IABSE-JSCE Conference, Dhaka*, pp. 10–12, 2010.
- [51] V. Garg, B. Setia, V. Singh, and A. Kumar, “Scour protection around bridge pier and two-piers-in-tandem arrangement,” *ISH Journal of Hydraulic Engineering*, pp. 1–13, 2021.
- [52] V. Garg, B. Setia, and D. Verma, “Reduction of scour around a bridge pier by multiple collar plates,” *ISH Journal of Hydraulic Engineering*, vol. 11, no. 3, pp. 66–80, 2005.